FATIGUE BEHAVIOR AND MECHANISMS IN POWDER METALLURGY TI-6AL-4V TITANIUM ALLOY

by

Fei Cao

A dissertation submitted to the faculty of
The University of Utah
in partial fulfillment of the requirements for the degree of

Doctor of Philosophy

Department of Metallurgical Engineering

The University of Utah

December 2016

The University of Utah Graduate School

STATEMENT OF DISSERTATION APPROVAL

The dissertation of **Fei Cao**

has been approved by the following supervisory committee members:

Ravi Chandran	, Chair	**May 17, 2016** Date Approved
Zhigang Zak Fang	, Member	**May 17, 2016** Date Approved
Sivaraman Guruswamy	, Member	**May 17, 2016** Date Approved
Dinesh K. Shetty	, Member	**May 17, 2016** Date Approved
Ashley Spear	, Member	**May 31, 2016** Date Approved

and by **Manoranjan Misra** , Chair/Dean of

the Department/College/School of **Metallurgical Engineering**

and by David B. Kieda, Dean of The Graduate School.

ABSTRACT

Hydrogen sintering and phase transformation (HSPT) is a novel low-cost process for powder metallurgy (PM) titanium alloys. The microstructure obtained from the HPST process has very fine α grains, as well as other common features of a PM product, such as residual pores and large α grains. This research is aimed at evaluating the microstructure and mechanical behavior of Ti-6Al-4V alloy made from TiH_2 powders with different size distributions and a variety of processing parameters. Pneumatic isostatic forging (PIF) was carried out under β-tarsus to eliminate residual porosity without coarsening the grains. Tensile, fatigue, and crack growth properties of HSPT processed alloys, as well as wrought Ti-6Al-4V alloys, were studied in this research to investigate the microstructure-property relationships, with an emphasis on the effect of microstructural inhomogeneity on fatigue behavior.

Tensile properties of the HSPT Ti-6Al-4V alloys were found equivalent to or exceeded those of mill-annealed alloy. The low cycle fatigue (LCF) life was also found equivalent to that of wrought Ti-6Al-4V after PIF. However, the high cycle fatigue (HCF) performance was still inferior to that of wrought material due to the large α phase grain/grain boundary α phase plate, which was found to initiate cracks from inside of the specimen in HCF range. It is also shown that with the optimization of the distribution of powder sizes and the processing parameters, the properties of HSPT processed Ti-6Al-4V alloys are much superior to those of Ti-6Al-4V alloys made by other conventional

blended elemental (BE) methods, and equivalent to best properties found in alloys produced by pre-alloyed method in hot iso-static pressed (HIPed) and heat treated condition.

The S-N behaviors of different alloys were studied. Crack initiation types, sizes, and locations were found to alter the fatigue failure mechanism and the shape of S-N curves. The quantitative correlations between crack initiation size, location, and the S-N curve shape were also revealed in this study. Fatigue crack growth tests were carried out using miniature single edge-notched tension (SENT) specimens to evaluate the crack growth behavior. Crack growth stages were classified based on the characteristics of fractographs of both fatigue failed samples and crack growth samples. Microstructurally small crack growth rate was calculated from rough area size and fatigue life consumed in this region. The predicted S-N curves at HCF region based on crack growth rate at different stages for Ti-6Al-4V alloys with different crack initiator sizes match very well with the current HCF data.

TABLE OF CONTENTS

ABSTRACT iii

LIST OF TABLES viii

ACKNOWLEDGEMENTS ix

Chapters

1. INTRODUCTION 1

    1.1 Background 1
    1.2 Fatigue of Powder Metallurgy Titanium 2
    1.3 Objective of the Present Research 4

2. LITERATURE REVIEW 5

    2.1 Fatigue Performance of Powder Metallurgy Ti-6Al-4V Alloy 5
    2.2 PM Titanium Using TiH_2 18
        2.2.1 Vacuum Sintering of TiH_2 18
        2.2.2 Beneficial of Using TiH_2 as Raw Material 18
        2.2.3 Hydrogen Sintering and Phase Transformation Process 20
    2.3 Fatigue Behavior of Engineering Alloys 21
        2.3.1 Low Cycle and High Cycle Fatigue 21
        2.3.2 Fatigue Behavior 22
    2.4 HCF Crack Initiation and Small Crack Propagation in Ti-6Al-4V Alloy 25
        2.4.1 Crack Initiation 25
        2.4.2 Near Threshold Crack Growth 27
    2.5 References 33

3. MATERIALS AND EXPERIMENTAL PROCEDURE 36

    3.1 Materials Fabrication 36
    3.2 Tensile and Fatigue Testing 37
    3.3 Fatigue Crack Growth Testing 38

4. ROLE OF CRACK INITIATION AND DUALITY OF FATIGUE RESPONSE 41

4.1 Introduction....42
4.2 Material and Experimental Procedure....43
4.3 Results and Discussion....44
4.3.1 Microstructure and Fatigue Failure Initiations of PM Ti-6Al-4V....44
4.3.2 S-N Curves of PM Ti-6Al-4V by HSPT....45
4.3.3 Duality of S-N Fatigue Behavior....46
4.4 Conclusions....47
4.5 References....48

5. FATIGUE PROPERTY OF TI-6AL-4V BY HYDROGEN SINTERING AND PHASE TRANSFORMATION....49

5.1 Introduction....50
5.2 Experimental Procedures....51
5.3 Results and Discussion....52
5.3.1 Materials and Microstructures....52
5.3.2 Tensile Properties....55
5.3.3 Fatigue Performance....55
5.3.4 Mechanisms of Fatigue Failure....56
5.3.5 Comparison against Other PM Ti-6Al-4V Alloys....59
5.4 Conclusions....59
5.5 References....60

6. FATIGUE CRACK GROWTH BEHAVIOR....61

6.1 Introduction....61
6.2 K Solution for the Present Miniature Specimen....62
6.3 Crack Growth Behavior of HSPT Ti-6Al-4V Alloys....65
6.4 References....77

7. FAILURE ANALYSIS AND LIFE PREDICTION....78

7.1 LCF Failure and Mechanism of S-N Curve Transition....78
7.1.1 -400 HSPT Ti-6Al-4VAlloy....78
7.1.2 HSPT + PIF and Mill-annealed Ti-6Al-4V Alloys....81
7.2 HCF Failure and Near Threshold Crack Growth....81
7.2.1 HCF Crack Initiation from Internal Pore....82
7.2.2 HCF Crack Initiation from Near Surface Facet....83
7.2.3 HCF Crack Initiation from Internal Facet....85
7.2.4 Summary of HCF Failure Mode....87
7.3 Quantitative Fractograph Analysis and HCF Life Prediction....88
7.3.1 Introduction....88
7.3.2 Quantitative Fractograph Analysis....90
7.3.3 Near Threshold Crack Growth Rate....92
7.3.4 HCF Life Prediction....94

7.4 References.....113

8. CONCLUSIONS.....115

LIST OF TABLES

2.1 Parameters used to fit the fatigue data with the fatigue constitutive equation…....…9

2.2 Properties of PM Ti-6Al-4V in the as-sintered condition…….....……10

2.3 Properties of PM Ti-6Al-4V alloy in the sintered plus HIPed condition……..11

2.4 Properties of PM Ti-6Al-4V alloys in heat treated condition…..……..13

2.5 Properties of PM Ti-6Al-4V alloy thermomechanically processed condition…..….15

5.1 Composition of HSPT-processed Ti-6Al-4V alloys in weight percent…….…....51

5.2 Tensile properties of HSPT-processed Ti-6Al-4V alloys……..……54

6.1 Sizes of plastic zones a the end of tests…….....……64

7.1 Average values of crack initiation size and ΔK_{ini}……..…....…76

7.2 Results of quantitative fractography analysis data…….……..102

ACKNOWLEDGEMENTS

First I would like to thank my advisor Dr. K.S. Ravi Chandran for his patience and guidance during my research and study at University of Utah. I have greatly benefited from his helpful comments and insight throughout the completion of this work. My special thanks go to Dr. Zhigang Z. Fang for letting me use their equipment, and being on my supervisory committee. I would also like to thank the other committee members: Dr. Sivaraman Guruswamy, Dr. Ashley Spear, and Dr. Dinesh K. Shetty, for their time, interest, and helpful comments. I would like to acknowledge Dr. Pei Sun, Dr. James Paramore, Dr. Mark Koopman, Matt Dunstan, and my lab mates Pankaj Kumar, Yuxuan Zhang, and Bhaskar Vadlamani for their constant help in my work. And lastly, I would like to thank my family for all their love, support, and encouragement.

CHAPTER 1

INTRODUCTION

1.1 Background

Civilian use of titanium, such as in biomedical tools and automobile industries, has been severely restricted due to its high cost. One of the ways to solve this problem is by using the near-net shape process, such as powder metallurgy (PM). Powder processing has been regarded as a promising approach for reducing cost of Ti fabrication because of the near-net-shape capability. However, after several decades of research and development, the use of powder metallurgy titanium is still very limited due to inferior properties in comparison with wrought titanium. However, the demand for low-cost titanium continues to drive the research and development of new technologies. In the past few decades, a variety of powder-related processes of titanium, as well as postprocessing treatments, have been developed. However, the inherent low-cost characteristics of powder metallurgy is often diminished by the need to improve mechanical properties and lowering interstitial impurities through high pressure consolidation, thermo-mechanical processing, or pre-alloying through melting.

Apart from complex shape, many applications require good mechanical properties of the component, especially related to fatigue resistance. Therefore, cost reduction

without sacrificing performance is the major task to materialize PM titanium. Only a truly low-cost PM process for producing titanium alloys with good mechanical properties can possibly be used in cost-sensitive civilian applications. Therefore, the research on PM Ti should be limited to low-cost techniques to produce titanium components with desired microstructure and properties. The low-cost techniques include blended elemental method, low-cost press and sinter technique, and as least as possible postsintering consolidation process, thermo-mechanical processing. Most importantly, the raw material should also be low-cost, easy to compact, and with high purity.

1.2 Fatigue of Powder Metallurgy Titanium

PM materials share one characteristic property with all conventionally produced materials; they also contain defects and weak spots. Effect of defects on fatigue, such as nonmetallic inclusions, on the fatigue property of steels, has been extensively studied. However, because wrought titanium alloys are pore free and very clean, the microstructural discontinuity-related fatigue mechanism has not yet been investigated extensively for titanium alloys. PM processed titanium parts are not as clean as wrought titanium alloys, in order to extend the limits of application of PM titanium alloys as far as possible. It becomes necessary to understand the effect of the defects on fatigue property of PM titanium components.

Internal fatigue origins are most commonly associated with high cycle fatigue (HCF) loading. Before entering service, titanium alloys are often subjected to cold working to increase resistance to fatigue. This is achieved by surface treatment to produce compressive residual stresses at the surface. Fatigue cracks were eventually initiated

subsurface and propagate internally before connecting to the component surface and the surrounding atmosphere. The fatigue cracking mechanism and associated fatigue crack growth rates of internal features are poorly understand, and provide a major challenge regarding estimation of component life. The pre-existing defects in the bulk of PM materials weaken the material, leading to internal failures with much shorter time. Thus the effect of microstructural discontinuities, such as residual pore and large phase grain that are commonly seen in blended elemental PM titanium alloys, on fatigue performance should be addressed.

As is known, the fatigue life of PM titanium is usually shorter than that of wrought material due to imperfections in the microstructure; internal crack initiation can be seen at fatigue life around 1 million cycles, which is a critical regime, where both crack initiation and crack propagation are important. In PM titanium alloys, with the presence of a variety of microstructural features, the crack initiation mechanism would be more complicated. Thus, the mechanism of micro-crack initiation and microstructural short crack growth under the traditional mechanical threshold is meaningful to predict fatigue life and understand how the fatigue life is affected by the microstructural discontinuities. The crack initiators are generally larger than normal grain size, and the effect of size of crack origins on fatigue behavior in titanium is poorly understood. It is currently impossible to do in-situ crack initiation and microstructural short crack growth observations to study the mechanism and HCF life portion at different stages due to the restriction of resolution. Thus, the characteristics of the fractographs are the direct source that can be used to distinguish the crack growth stages and reveal failure mechanisms.

1.3 Objectives of the Present Research

The objectives of this research work are:

1. To establish processing-microstructure-property relationships in PM Ti-6Al-4V alloy made from TiH_2 by using the hydrogen sintering and phase transformation (HSPT) process.

2. To investigate the effect of microstructure on fatigue crack initiation, and the role of fatigue crack initiation in the fatigue behavior of PM Ti-6Al-4V alloy.

3. To evaluate the crack growth behavior using miniature specimens and study the crack growth mechanisms at different stages.

4. To reveal HCF failure mechanism and predict HCF life based on crack initiation size and crack growth rate at different stages.

CHAPTER 2

LITERATURE REVIEW

2.1 Fatigue Performance of PM Ti-6Al-4V Alloy

Published as:

Fei Cao and K.S. Ravi Chandran

Fatigue Performance of Powder Metallurgy (PM) Ti-6Al-4V Alloy: A Critical Analysis of Current Fatigue Data and Metallurgical Approaches for Improving Fatigue Strength

JOM, 2016, Volume 68, Issue 3, pp 735-746.

JOM, Vol. 68, No. 3, 2016
DOI: 10.1007/s11837-016-1821-5

Fatigue Performance of Powder Metallurgy (PM) Ti-6Al-4V Alloy: A Critical Analysis of Current Fatigue Data and Metallurgical Approaches for Improving Fatigue Strength

FEI CAO[1] and K.S. RAVI CHANDRAN[1,2]

1.—Department of Metallurgical Engineering, The University of Utah, 135 South 1460 East Rm. 412, Salt Lake City, UT 84112, USA. 2.—e-mail: ravi.chandran@utah.edu

A comprehensive assessment of fatigue performance of powder metallurgy (PM) Ti-6Al-4V alloy, manufactured using various powder-based processing approaches to-date, is performed in this work. The focus is on PM processes that use either blended element (BE) or pre-alloyed (PA) powder as feedstock. Porosity and the microstructure condition have been found to be the two most dominant material variables that control the fatigue strength. The evaluation reveals that the fatigue performance of PM Ti-6Al-4V, in the as-sintered state, is far lower than that in the wrought condition. This is largely caused by residual porosity, even if it is present in small amounts, or, by the coarse lamellar colony microstructure. The fatigue strength is significantly improved by the closure of pores, and it approaches the levels of wrought Ti-6Al-4V alloys, after hot-isostatic-pressing (HIPing). Further thermo-mechanical and heat treatments lead to additional increases in fatigue strength–in one case, a high fatigue strength level, exceeding that of the mill-annealed condition, was achieved. The work identifies the powder, process and microstructure improvements that are necessary for achieving high fatigue strength in powder metallurgical Ti-6Al-4V alloys in order for them to effectively compete with wrought forms. The present findings, gathered from the traditional titanium powder metallurgy, are also directly applicable to additively manufactured titanium, because of the similarities in pores, defects, and microstructures between the two manufacturing processes.

INTRODUCTION

Achieving high fatigue resistance in components manufactured by powder metallurgy (PM) is a challenging task, regardless of metal class. This is because of the influence of porosity in initiating fatigue cracks overriding the effects of microstructure, sintering parameters or the source powder characteristics. Additionally, the variations in powder and process parameters are intrinsically reflected in the nature of porosity itself, making pores and the associated parameters (shape, volume fraction and size and spatial distribution) as being the dominant variables affecting fatigue behavior of sintered, as well as additively manufactured metals. In a PM component, one should expect the porosity to vary from specimen to specimen, regardless of the manufacturing method. There is no way to tell if the porosity volume fraction is zero, even after optimizing the sintering process or if all the pores closed in the post-sintering treatments.

Fatigue strength is the most sensitive mechanical property of a PM or additively manufactured component because a crack can initiate even from a single, isolated pore in the test volume. For this reason, it has often been found that fatigue fracture of a specimen occurred from a large pore that was not discovered in metallographic sections. Any assessment of fatigue performance of PM components begins with volume fraction of porosity. Haynes[1] showed that in Cu and Fe-based sintered materials, the fatigue endurance limit and the scatter in fatigue life data are greatly affected by the volume fraction of porosity. Any change in powder feedstock characteristics or sintering conditions or post-sintering heat treatments can changes

(Published online January 28, 2016)

the pore volume fraction and the size of the largest pore, and sometimes, this change is also accompanied by the changes in microstructure, making it difficult to resolve the independent effects of porosity of microstructure on fatigue performance. This situation is largely similar to the fatigue behavior of cast metals[2,3] where, in addition to the porosity arising from shrinkage, microstructural factors that are linked to the solidification behavior such as large dendritic arm spacing, constitutional segregation play additional roles in affecting the fatigue performance of cast metals. In the case of PM titanium alloys, fatigue behavior is known to be strongly affected by porosity as well as the physical location of pores, either in the specimen surface or interior.[4,5] In addition, one can expect any compositional non-uniformity or microstructural coarsening due to sintering, may affect the fatigue performance. These aspects are to be clearly understood and controlled in any PM titanium alloy, for it is to compete with wrought material, reliably and economically. In this work, a complete survey of the available fatigue data on PM Ti-6Al-4V alloy is made. A critical analysis of fatigue data has been made by structuring that data in logical groups. The key PM process and microstructure variables affecting the fatigue performance are identified and the effective metallurgical approaches necessary for bringing up fatigue strength of PM alloys on par with their wrought versions are highlighted.

POWDER METALLURGICAL PROCESSING APPROACHES FOR TI-6AL-4V COMPONENTS

At the outset, fatigue behavior of PM titanium alloys is greatly influenced by the nature of the powder feedstock and the PM processing steps involved. Various processing techniques for producing the powder feedstock for the manufacturing of titanium compacts have been investigated in the past decades. Figure 1 illustrates the processing flow chart that shows the starting points, the intermediate steps and the final product outcome in various approaches of powder metallurgical manufacturing of titanium. The most commonly used powders are blended elemental (BE) powders, pre-alloyed rotating electrode process (PREP) powders and powders obtained through the hydride-and-dehydride (HDH) process that starts with titanium sponge. The latter powders are often called HDH sponge fines. Either the directly milled elemental powders or the milled HDH sponge fine powders are usually used as feedstock for the most common method of PM titanium processing—the blended elemental method. Titanium hydride powder can also be used as feedstock for manufacturing titanium by either vacuum sintering[6] or hydrogen sintering[7] of TiH_2 powder compacts followed by phase transformation and dehydrogenation. The use of expensive pre-alloyed powders such as PREP powders may be preferred over BE powders due to possibility of consolidation (by HIP) in a short time and without the need for alloy homogenization in sintering.

In general, the PM titanium processing involves a primary sintering step such as vacuum sintering of cold compacted titanium powders except in the case of direct hot pressing or HIP of powders. The primary consolidation step (cold press + sinter) may be followed by heat treatment and/or thermomechanical processes to eliminate the pores and/or refine the microstructure. When the post consolidation step is more detailed, including thermomechanical processing and/or heat treatment, greater improvements in the PM materials' microstructure and tensile and fatigue properties can be expected. This is due to a more through closure and welding of pores and accompanied by substantial microstructure refinement. Thus it is not surprising that the best high-cycle-fatigue (HCF) properties of PM Ti-6Al-4V were achieved[8] using PREP powder followed by HIPing, thermomechanical processing and annealing. It will be shown that the fatigue data compiled in this review supports the general discussion presented above.

MICROSTRUCTURAL FACTORS AFFECTING FATIGUE STRENGTH

The fatigue properties of PM titanium alloys are generally lower compared to wrought alloys, especially with respect to HCF strength, unless careful powder processing and microstructure control after sintering is achieved to eliminate microstructural discontinuities such as porosity, coarse microstructure, grain boundary α and inclusions. The answer to the question of which of these microstructural factors becomes the dominate factor that controls the fatigue performance, depends on the powder parameters, the processing approach, and the post consolidation processes such as thermomechanical processing, and heat treatment.[9] Of all these factors, perhaps the most important parameter is the porosity in PM titanium alloys. As pores are detrimental to the fatigue performance of titanium alloys, generally, there is resistance in the industry to use titanium alloy with pores for fatigue-sensitive applications. This is possibly because even though the porosity is controllable to very low levels, fatigue strength has been shown[10] to be significantly degraded even when the amount of porosity is less than one percent. For fatigue fracture to occur, all that needed is one crack to initiate from a random pore in the microstructure. This is the principal reason for the HIPing of PM materials, akin to HIPing of cast titanium alloys to prevent the degradation of fatigue performance due to solidification porosity. HIPing is a costly procedure, but it has been an effective process for PM titanium materials and castings to eliminate pores and thus improve the mechanical performance of alloy.[11]

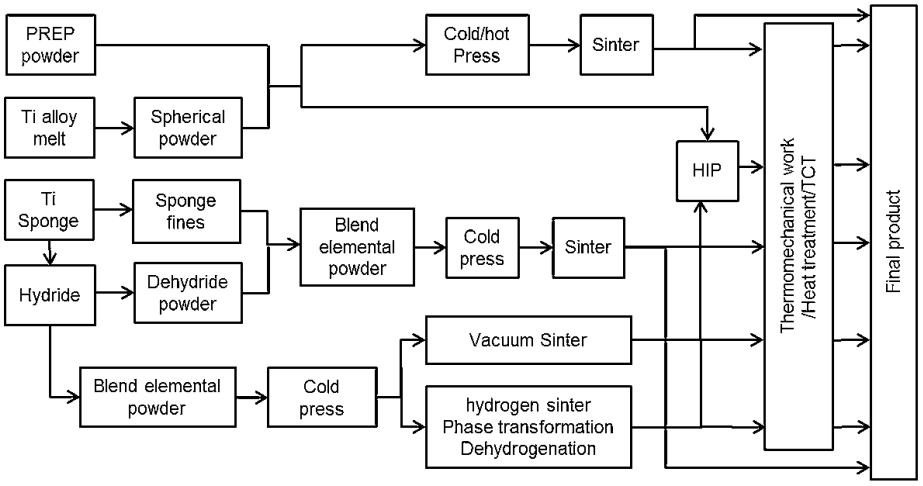

Fig. 1. Flow chart of powder metallurgical manufacturing of titanium alloys.

HIPed PM titanium compacts have densities equivalent to the wrought materials and a finer grain size, when compared to the PM samples made by cold pressing and sintering steps alone.

A CONSTITUTIVE EQUATION TO CHARACTERIZE THE S–N FATIGUE BEHAVIOR OF TITANIUM ALLOYS

In the comparisons of S–N fatigue behavior of various PM processed titanium alloys the fatigue the data exhibit significant scatter and the data trends often overlap, which lead to difficulties in identifying the trends. To facilitate easy characterization of the data trends we use here an S–N constitutive equation to fit the fatigue data. The S–N fatigue equation was developed based on a physically based theory of fatigue, by Chandran.[12] The equation is given by

$$\left(\frac{\sigma_a - \sigma_e}{\sigma_u - \sigma_e}\right) = \exp\{-C_n (N_f)^{m_n}\} \qquad (1)$$

where σ_a and σ_e are the applied and fatigue limit stress amplitudes, σ_u is the ultimate tensile strength, C_n and m_n are constants representing the fatigue behavior of the material and N_f is cycles to failure. The right side of the equation is the probability of specimen survival. The left side is the scaling of the fatigue stress level, ranging from the fatigue limit as the lower bound and the tensile strength as the upper bound. The equation exhibits the expected behavior at the extremes, that is, in the limit of fatigue stress amplitude approaching tensile strength, the fatigue failure cycles tend to zero and when the stress amplitude approaches the fatigue limit, failure cycles tend to infinity. Equation 1 can be rearranged, to reflect the fact that the N_f is a dependent variable in fatigue tests, as

$$N_f = \left[-\frac{1}{C_n} \ln\left(\frac{\sigma_a - \sigma_e}{\sigma_u - \sigma_e}\right)\right]^{1/m_n} \qquad (2)$$

The above equation serves as the constitutive equation to describe the S–N fatigue behavior for the fully reversed fatigue (zero mean stress) condition. It is a function of only the non-dimensional parameters, C_n and m_n and the requisite boundary conditions—the fatigue strength and the ultimate tensile strength. The parameters C_n and m_n define the shape of the S–N fatigue curve. The fatigue data assessed in this study are well represented by this constitutive equation because the curves could be fitted easily by suitable choice of C_n and m_n. The parameters are listed in Table I.

FATIGUE PERFORMANCE OF SINTERED PM TI-6AL-4V ALLOYS

A compilation of fatigue data of Ti-6Al-4V alloys, made by cold pressing of powders (BE or PA powders) followed by vacuum sintering to obtain compacts with >95% density,[13,14,17] is presented in Fig. 2. The processing conditions, microstructural features and tensile properties for these samples are listed in Table II. Generally, fatigue endurance limit is defined as the cyclic stress amplitude (or maximum stress for fully reversed fatigue cycle) for specimen survival for 10^7 cycles. On the basis of this definition, it can be seen that the fatigue strength levels for the as-sintered materials, in Fig. 2, ranged from 200 MPa to 400 MPa, when the density varied from 95% to >99%. The trend lines are from

Table I. Parameters used to fit the fatigue data with the fatigue constitutive equation[8,11,13–16]

Process	Data source	Tensile strength (MPa) (σ_u)	Fatigue strength (MPa) (σ_e)	C_n	m_n
CP + VS	Anderson BE	926	400	2.0E−9	2
	Fujita BE	926	350	8.0E−3	0.67
HIP	Moxson BE	965	340	3.8E−3	0.42
	Hagiwara BE	922	400	5.2E−4	0.54
	Wirth PREP	967	480	2.0E−4	0.59
HIP + HT	Eylon BE	937	500	4.5E−7	1.4
	Hagiwara BE	1186	700	1.4E−3	0.5
	Eylon PREP	950	600	3.0E−3	0.6
Hot worked	Wirth PREP, Equiaxed	1050	590	2.0E−3	0.6
	Wirth PREP, Lenticular	1090	680	3.5E−3	0.37
Mill + annealed	Cao, Chandran, [unpublished work]	1045	720	5.0E−3	0.4

CP cold pressing, *VS* vacuum sintering, *HIP* hot-isostaic-pressing, *HT* heat treatment, *BE* blended element, *PREP* plasma rotating electrode process.

the S–N constitutive equation (Eq. 1)—the data are well represented by the trend lines. To avoid confusion only two sets of data are fitted with the constitutive equation. The data provide an illustration of the effect of density of the sintered material on fatigue performance—less dense materials have a relatively higher volume fraction of and/or a relatively larger size of the crack-initiating pores, leading to fatigue crack initiation at a relatively lower stress level. In addition, the tensile strength of the sintered material is also affected by porosity—at lower densities, the strength of the porous materials will also be lower, relative to the fully dense material. In addition to the physical effect of pores itself, which acts as a crack initiator, the low strength will further decrease the fatigue performance, because of an increased stress on the net section material. Hence, due to two main factors (the decrease in porosity and the absence of strength-lowering effect of porosity) the fatigue strength will be expected to increase with the increasing of as-sintered density of PM titanium parts. The data in Fig. 2 is consistent with this expectation. In addition to these factors, the presence of extreme-sized (the pore with the largest size) pore in the test volume, even in a nearly-fully-dense material will also affect the fatigue performance. The location and the size of the extreme-sized pores can impact, in addition to the fatigue life, the extent of scatter in fatigue life itself. These aspects are, however, experimentally difficult to isolate.

The basic processing or sintering approach involved in the manufacture of PM Ti-6Al-4V alloys, shown in Fig. 2, is cold consolidation and vacuum sintering at a temperature above the β-transus temperature, for several hours. The β-transus temperature is about 1010°C for the Ti-6Al-4V alloy. This sintering approach does not necessarily yield full density or even close to the full density, unless sintering temperatures are high and the sintering

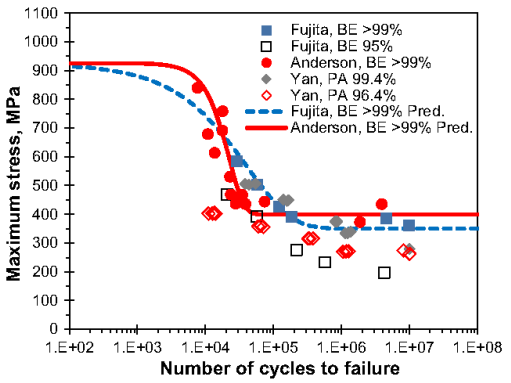

Fig. 2. S–N fatigue data of PM Ti-6Al-4V alloys made by cold pressing and vacuum sintering in the β-phase field. All the samples have the lamellar $\alpha + \beta$ colony miocrostructure.

times are long. Further, because the sintering temperature is above the β transus, substantial growth of β grains occurs with the end result being coarse $\alpha + \beta$ colony structure in the sintered microstructure. Thus, in addition to residual porosity, coarse lamellar colonies are commonly found in titanium PM parts made by the above-β-transus-sintering approaches.[11,16] This means that even if the porosity could be eliminated, the coarse lamellar colonies would be expected to initiate fatigue cracks, with relative ease, leading to a generally poor fatigue performance of vacuum sintered PM Ti-6Al-4V. This appears to be reflected in the range and ranking of the fatigue data in Fig. 2. The fatigue strengths vary between about 200 and 400 MPa, which is only about 30% of the ultimate tensile strength (UTS), giving a fatigue-strength-to-tensile-strength ratio of about 0.3. The "normal" value of fatigue strength of recrystallization-

Table II. Summary of processing conditions, microstrurcture and tensile properties of PM Ti-6Al-4V in the as-sintered condition[13,14,17]

Source	Powder type and size	Processing	Microstructure	Yield strength (MPa)	Tensile strength (MPa)	%Elongation	%Reduction area	%Theoretical density
Fujita	HDH, < 149 μm	CP + VS 1260°C, 4 h	Lamellar colonies with GB-α, ~50 × 10 μm	809	926	19	31	99.6
Anderson	SF, < 149 μm	CP + VS	Equiaxed α, ~30 μm	866	933	12.5	20	>99
		620 MPa, 1260°C, 4 h						
Yan	PA, milled 45–250 μm	CP + VS	Lamellar colonies with GB-α,	848	925	6.2	–	99.4
		690 MPa, 1371°C, 1.5 h	Prior β grain size, ~150 μm					

HDH hydride-dehydride, *SF* sponge fine, *PA* pre-alloyed. See Table I for other abbreviations.

annealed wrought Ti-6Al-4V alloy is about 600 MPa or higher with microstructure refinement. The fatigue-strength-to-tensile-strength ratios for the wrought titanium alloys are generally >0.5. Thus, the fatigue strength of the as-sintered PM Ti-6Al-4V alloys, regardless of powder feedstock type is quite inferior to wrought alloys.

One of the reasons for the poor fatigue performance and/or the large variability in the fatigue data of PM titanium alloys is to do with the size and the distribution of pores in the volume and how they vary with the volume of the test section. In samples with a copious amount of porosity, fatigue cracks generally initiated from pores at the surface of specimen. However, the fatigue cracking, as initiated from subsurface pores or pore clusters can occur, as long as the specimen volume contained a pore large enough to nucleate a fatigue crack.[5] In this scenario, sintering pores both on the surface and in the bulk of the specimen can independently act as fatigue crack initiators with a very short crack initiation life and the cracks can propagate to failure, resulting in a relatively shorter fatigue life. A relatively larger size of the pore leads to larger initiated crack, and a relatively larger value of the stress intensity factor of that crack accelerates the fatigue crack growth. In microstructures with $\alpha + \beta$ lamellar colonies, there can be competition between pores and the colony microstructure for fatigue crack initiation. When the pore size is smaller than the large lamellar colonies in vacuum sintered titanium alloys, the lamellar colonies act as initiators of fatigue cracks. When a PM Ti-6Al-4V alloy with sintering pores was tested at low stress levels, crack initiating facets that are larger in size than the competing pores were found at the fatigue initiating site.[18] Such facets usually correspond to large lamellar colonies or in some cases either α/β interface or grain boundary α platelets. Thus, the fatigue crack initiation mechanism in PM Ti-6Al-4V compacts is determined by the competition between pores (surface or internal) and large lamellar colony type microstructural units. It can thus be stated that unless the size of the crack initiator is reduced to very small levels (typically <25 μm) by some microstructure modification, any further improvement in the fatigue strength of as-sintered Ti-6Al-4V beyond the currently observed endurance limit range of 300–400 MPa is unlikely.

FATIGUE PERFORMANCE OF SINTERED PLUS HIPED OR DIRECTLY HIPED PM TI-6AL-4V ALLOYS

Because residual pores or coarse $\alpha + \beta$ lamellar colonies in the microstructure have been found to be deterimental to fatigue strength, processing innovations geared toward enhancing the fatigue strength of PM titanium alloys generally focused on ways to close and weld the pores resulting from the lack of complete sintering. One effective step in

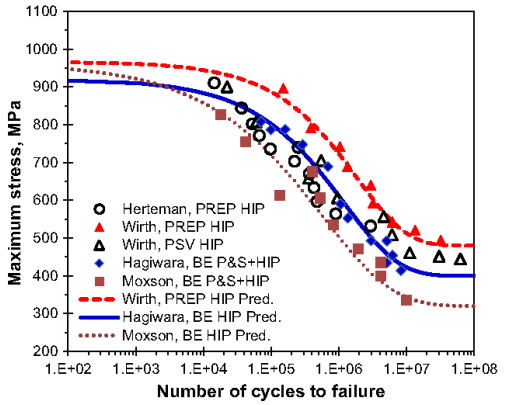

Fig. 3. S–N fatigue data of PM Ti-6Al-4V alloys made by cold pressing plus sintering and then followed by HIPing/or HIPing directly.

this regard is to HIP the vacuum sintered material with two general objectives: (i) to close all the sintering pores and (ii) to impart some mechanical work to help break the lamellar colonies and refine the microstructure. While the former result is readily expected because of the hydrostatic nature deformation imposed in HIPing, it is not yet clear if the second effect would occur in HIPing. This is because it can be argued that HIPing deformation is purely hydrostatic not deviatoric, at the scale of its application, thus any distortional component of deformation, which helps to recrystallize microstructure, is largely absent in HIPing. However, in regions local to pores and at phase or grain boundaries, this may not be the case. Further research is necessary to identify ways to refine microstructure after vacuum sintering of Ti-6Al-4V alloy.

Figure 3 illustrates the compilation of fatigue performance of PM Ti-6Al-4V materials that were HIPed after the primary consolidation step (cold pressing + sintering), either using BE or PA powders. The detailed processing conditions and paramters are listed in Table III. Herteman et al.,[19] Wirth et al.[8] and other researchers not listed here have used direct HIPing of PREP and PSV (electron beam vacuum melted) powders to make several titanium alloys. Hagiwara et al.[16,20] and Moxson et al.[21] also performed HIPing of BE compacts after vacuum sintering in the β-phase field ($\sim$ 1300°C). In both of these studies, the Ti-6Al-4V alloy samples almost attained the theoretical density. The trend lines in Fig. 3, as fitted by the constitutive equation, again help to identify the shifts in fatigue performance with changes in PM processing. In Fig. 3, it can be seen that the fatigue performances of HIPed PREP/PSV and BE titanium alloys are comparable to each other in the high-stress/low-cycle-fatigue (LCF) regime, which is the cycle range with failure cycles less than 10^5. In the low-stress and high-cycle-fatigue

Table III. Summary of processing conditions, microstrurcture and tensile properties of PM Ti-6Al-4V alloy in the sintered plus HIPed condition[8,9,16,19–21]

Samples	Powder	Processing	Micro-structure	Yield strength (MPa)	Tensile strength (MPa)	%Elongation	%Reduction area
Herteman	PREP*, < 425 μm	HIP, 925°C, 1050 MPa, 5 h	Lamellar colonies, ~80 × 10 μm	860	937	17	42
Wirth	PREP 63–350 μm	HIP, 925°C, 198 MPa, 3 h	Lamellar Colonies, ~ 30 × 5 μm	900	967	14.5	41.4
Wirth	PSV	HIP, 925°C, 198 MPa, 3 h	–	871	934	11.9	26.4
Hagiwara	BE, HDH < 149 μm	CP + VS, 1300°C, 4 h	Lamellar colonies, ~ 100 × 10 μm	833	922	14	36
		HIP, 930°C, 98 MPa, 3 h					
Moxson	BE, HDH < 177 μm	CIP, 410 MPa	Lamellar colonies, ~ 100 × 10 μm	865	965	12.9	31.6
		VS, 1260°C, 4 h					
		HIP, 955°C, 207 MPa					

*PSV is Pulvérisation, Sous Vide–electron beam vacuum melted, *CIP* cold-isostatic-pressing. See Tables I and II footnotes for other abbreviations.

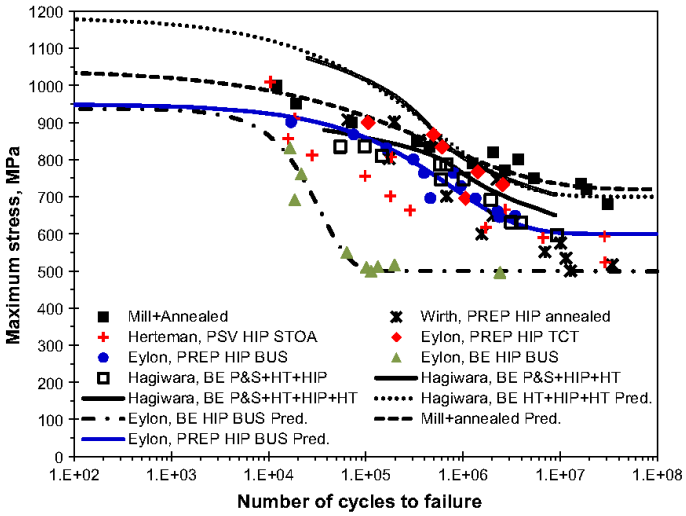

Fig. 4. S–N fatigue data of PM Ti-6Al-4V alloys made by cold pressing and sintering followed by HIPing and including prior/post-HIP heat treatments.

(HCF) regime, (failure cycles $> 10^6$ cycles) the fatigue performance of HIPed BE compacts is a little bit inferior to that made from PREP/PSV powders. The HCF performance is more sensitive to porosity and microstructure size, than the LCF performance. From the microsturctures provided,[21] it was determined that the microstructures of BE samples had relatively lager grains. Additionally, the grain size was more variable than that found in the alloy made from PREP/PSV powders.[8] The larger grains had likely resulted from the compositional and deformation inhomgeneties arising from inadequate powder processing and limited diffusion of alloying elements, which is possible in BE approaches. In general, the fatigue endurance limit values of PM titanium alloys, finished by the HIPing step but without any additional thermomechanial treatments, are found to lie between 350 MPa and 500 MPa (Fig. 3). Although the variation in the fatigue data suggests that the fatigue peformance after HIPing also depends on the prior history, that is the powder type and processing parameters, the overall performance is much higher than that is achieved by the cold pressing followed by vacuum sintering procedure. This is clearly attributable to the elimination of porosity in HIPing and, to some extent, a reduction in grain size due to lower processing temperature than that of vacuum sintering.

FATIGUE OF SINTERED, HIPED, AND HEAT TREATED PM TI-6AL-4V ALLOYS

The most convenient metallurgical path for microstructure refinement, after any mechanical processing, is the recrystallization of the microstructure by heat treatment. Heat treatment is the preferred industrial approach to produce a more uniform and a desirable size and morphology of microstructure in the PM materials. This has been shown to be successful in many PM materials that have been subject to some form of pressing either before or after primary consolidation. Another motivation is that any HIPing process many not necessarily modify the base microstructure suitably because the main objective of the HIP process is to close the pores. Thus, a heat treatment subsequent to the HIPing step can be viewed as also the step of microstructure restoration or modification into a desired form.

Figure 4 illustrates the fatigue performance of PM Ti-6Al-4V alloy samples that have used either BE or PREP powders as feedstock, consolidated by HIP, and followed by varied heat treatments. The heat treatment procedures are listed in Table IV. In general, the heat treatment of titanium involves two primary approaches. First is the heat treatment above the β transus temperature to homogenize phase and eliminate any history of deformed or undeformed α phase structure. Another motivation can be to set up a stage for producing a widmanstatten microstructure or finely divided $\alpha + \beta$ microstructure upon rapid cooling from the β-phase field. Eylon et al.[11] used this method, followed by aging, to obtain what was called the "broken-up-structure" (BUS). Because of the difficulties involved in achieving the required fast cooling rate through the entire thickness of large samples, this approach is of limited practical use. A more effective heat treatment approach for titanium alloys is to solution treat in the $\alpha + \beta$ phase field to produce a certain

Table IV. Summary of processing conditions, microstrurcture and tensile properties of PM Ti-6Al-4V alloys in the sintered plus HIPed plus heat treated condition[8,11,16,19,20]

Source	Powder type and size	Processing	Heat treatment	Microstructure	Yield strength (MPa)	Tensile strength (MPa)	%Elongation	%Reduction area
Herteman	PSV, 100–630 μm	HIP, 950°C, 1000 MPa, 5 h	975°C, 1 h WQ, 700°C, 2 h, AC	Martensite no GB-α	1020	1095	9	21
Wirth	PREP, 63–354 μm	HIP, 925°C, 198 MPa, 3 h	1010°C, 0.05 h, WQ, 900°C, 2 h, AC	Fine lamella	932	1036	13	29.1
Hagiwara	HDH, < 149 μm	CP, VS,1300°C, 4 h HT, 1050°C,WQ HIP, 930°C, 98 MPa, 3 h	–	Fine lamella	862	951	15	42
Hagiwara	HDH, < 149 μm	CP, VS,1300°C, 4 h HIP, 930°C, 98 MPa, 3 h	1050°C, 0.25 h, WQ 815°C, 24 h, AC	Fine lamella	921	1000	9	25
Hagiwara	HDH, < 149 μm	CP, VS,1300°C, 4 h HT, 1050°C,WQ HIP, 930°C, 98 MPa, 3 h	955°C, 1 h, WQ 540°C, 6 h, AC	Acicular α	1107	1186	10	27
Eylon	PREP	HIP, 925°C, 105 MPa, 5 h	1025°C, WQ, 815°C, 24 h	Coarser α platelets, broken up	910	1000	15	23
Eylon	PREP	HIP, 925°C, 105 MPa, 5 h	1025°C, 0.3 h, WQ, Hydro. 600°C, De-hydro. 760°C	Finer α platelets, broken up	965	1048	8	17
Eylon	BE	CP, 420 MPa VS, 1260°C, HIP, 930°C, 105 MPa, 5 h	1025°C, WQ 815°C, 24 h	Coarser α platelets, broken up, Density > 99.5	834	937	11	26

WQ water quech, *AC* air cooling. See previous Tables for other abbreviations.

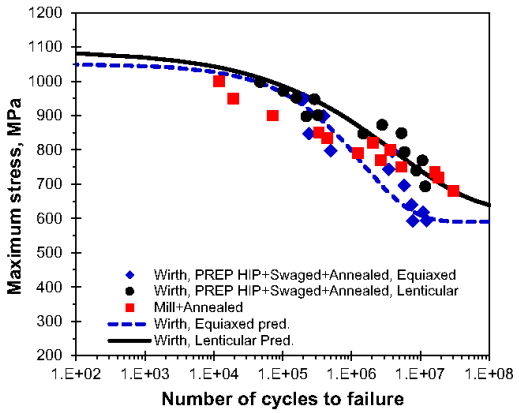

Fig. 5. S–N fatigue data of PM Ti-6Al-4V alloys made by first cold pressing and sintering followed by HIPing + thermo-mechanical processing + heat treatment, as indicated.

amount of primary-α phase, and then cool at different rates to produce a transformed $\alpha + \beta$ phase structure in the rest of the sample. This often leads to a duplex microstructure providing a good balance of strength, ductility and fatigue resistance. Most of the heat treatments refered to in Fig. 4 are of this (duplex) type, with the differences in their microstructural features resulting from the variations in temperature, time and cooling rate in the different investigations. Another effective and well known heat treatment is the thermochemical treatment [11] (TCT, also known as hydrovac process[22]), in which temporary alloying of titanium with hydrogen is made through a solution treatment (hydrogenation treatment), in the presence of hydrogen at atmospheric pressure, in the β-phase field. The subsequent eutectoid transformation of the hydrogen-alloyed titanium and the subsequent dehydrogenation at a lower temperature, results in a highly refined $\alpha + \beta$ microsructure.[11]

Figure 4 illustrates the fact that the fatigue performance of heat treated PM Ti-6Al-4V alloys after HIPing is much superior to the PM alloys that were just sintered (compare with the data in Fig. 2) or HIPed after sintering (compare with the data in Fig. 3). Again, the trend lines from the constitutive equation helps to discern the patterns in the fatigue data. With the exception of one data (Eylon, BE HIP BUS), the large improvement in fatigue performance, relative to the fatigue data in Figs. 2 and 3, is seen in both the LCF and the HCF regimes of the data. The fatigue limit strengths at 10^7 cycles range from 500 MPa to 600 MPa, which is close to the best fatigue performance of a wrought Ti-6Al-4V alloy (about 600 MPa). The range of fatigue endurance limit values, for the various samples compared in Fig. 4, is attributable to the microstructural differences arising from the different processing histories. According to Hagiwara et al.[20] and Chait et al.,[23] HCF strength is directly related to the size of the α phase, or more specifically to width of α-platelets in the transformed $\alpha + \beta$ microstructure. Consistent with this, the stacking of fatigue performance in Fig. 4 appears to generally correlate with the size of the α phase.

A more detailed analysis of the fatigue data in Fig. 4 is in the following. Eylon et al..[11] performed HIP and BUS heat treatment to BE titanium powder metallurgy compacts. The fatigue limit is much lower than that obtained in the samples made from the PREP and PSV powders. The microstructure contained residual micro-pores (density $>99.5\%$). This poor fatigue performance (Fig. 4), relative to other fatigue data, can be attributed to the presence of microscopic pores. It may also be attributed to the presence of relatively thicker α-plates. Coarse powders would cause poor densification and even slow the inter-diffusion and homogenization of alloying elements in the BE approach, which can lead to the presence of large α grains and residual porosity. In the samples made by Eylon (BE HIP BUS), these two types of microstructural factors could have resulted in for the poor fatigue performance. However, Hagiwara et al.[16,20] also used BE powders and a vacuum sintering approach followed by heat treatment and then HIPing of the compacts. The fatigue performance of the resulting microstructure was significantly higher compared to that without the heat treatment. The improvement is evident by comparing with the data (BE P&S + HIP) shown in Fig. 2. This improved fatigue performance is as good as the that found in products made by HIPing of PREP compacts followed by TCT, or BUS heat treatment. It is thus apparent that the blended elemental method can produce materials with high fatigue strengths if the parameters of sintering and heat treatment procedures are well optimized to eleminate porosity and refine the microstructure.

In the analysis of the data presented in Fig. 4, an important aspect of fatigue behavior should be noted. The microstrcture of the HIPed + heat treated PM Ti-6Al-4V compacts have a much finer $\alpha + \beta$ microstructure than that of the as-HIPed samples. However, some grain boundary plate and occassional large grains [20] were still present in the samples after HIPing and heat treatment. Despite this, it is quite remarkable that the HIPed + heat treated titanium alloys have excellent fatigue performance comparable to that of the wrought Ti-64 titanium alloy (Fig. 4), in the LCF regime. However, in the HCF regime, it appears that there is still some room for further improvement of fatigue performance–the S–N curve is not as flat as that is seen for the wrought mill-annealed Ti-6Al-4V alloy. The shape of the S–N fatigue curve (referring to the changes in curvature of the fatigue curves) for mill-annealed Ti-6Al-4V is possibly due to the grain size and shape in mill-annealed condition. The S–N

curve is nearly flat, as opposed to the strong exponential shapes in other microstrucutre conditions. It is possible that there are other factors that could explain this discrepancy—the mill-annealed wrought alloy samples used in fatigue testing were made from extruded rods that have a strong initial texture or preferred orientation. This initial texture is unlikely to have been completely eliminated in the heat treatment process of mill-annealing. Hence, the possible additional contribution from texture for the superior fatigue strengths of wrought alloys should be considered in evaluating the relative fatigue performance of PM titanium alloys.

It is important to note that any further improvements in fatigue performance in the HCF regime, to bring PM titanium alloys on par with the wrought Ti-6Al-4V alloys, might require more complex metal processing steps. This is evident from an assessment of selected fatigue data, shown in Fig. 5 and listed in Table 4. The trend lines generated from the S–N constitutive equation are also shown to identify easily the relative fatigue performance of the materials compared.

Generally, for the wrought Ti-6Al-4V alloy, the beginning of a large drop in fatigue strength with respect to the fatigue life, is around ten million cycles[24,25] for the bimodal and the equiaxed microstructures, while such a "drop" begins at around 1 million cycles for PM Ti-6Al-4V alloys, as shown in Fig. 4. The beginning of the decrease of fatigue strength at a relatively shorter fatigue life is caused by the microstructure discontinuities.[9] The large grains inside the material volume usually act as crack initiators at HCF regime. It is very difficult to eliminate all microstructural inhomogeneities inside the material volume without large deformation and recrystallization that created by, for example, thermomechanical processing. The microstructural discontinuties can be phase boundaries or α lamellar colonies. These discontinuties, generally present in sizes that are larger than normal grain size act as crack initiators. The fatigue life degradation is largely impacted by a relatively easy crack initiation and faster small crack growth rates, with a negligible contribution from the part where a large crack propagates to failure in the later stages of fatigue. This is because the improved fatigue performance in a microstructurally refined titanium alloy mostly comes from the resistance to fatigue crack initiation and the relatively larger extent of small crack growth in fatigue (Table V).

FATIGUE OF SINTERED, HIPED, THERMO-MECHANICAL PROCESSED AND HEAT TREATED PM TI-6AL-4V ALLOYS

Several interesting thermomechanical processing approaches were tried in early attempts at PM titanium alloy processing. Thermomechanical processes[8,26] such as isothermal forging, rolling and

Table V. Summary of processing conditions, microstrucrture and tensile properties of PM Ti-6Al-4V alloy in the sintered, HIPed, thermomechanically processed plus heat treated condition[9]

Sample	Powder type and size	Processing	Thermo-mechanical processing	Post-treatment	Micro-structure	Yield strength (MPa)	Tensile strength (MPa)	% Elongation	%Reduction area
Wirth	PREP, 63–354 μm	930°C, 193 MPa, 2.5 h	Extrusion, 1020°C Swage, 900°C	830°C, 2 h, AC	Fine Equiaxed α	931	1048	16.7	38.2
Wirth	PREP, 63–354 μm	930°C, 193 MPa, 2.5 h	Extrusion, 1020°C Swage, 900°C	1010°C, 0.05 h,WQ 900°C, 2 h, AC	Lenticular α	990	1088	12.7	28.3

See previous Tables for abbreviations.

swaging, were used in hopes of causing microstructure refinement that could possibly increase the fatigue strength. Wirth et al.[8] swaged the compacts after HIPing, and then employed two different heat treatment procedures to get PM Ti-6Al-4V alloys with equiaxed-α and lenticular-α microstructures. This processing resulted in a microstructure that has provided the highest fatigue strength (750 MPa fatigue limit corresponding to 10^7 cycles, Fig. 5) in PM Ti-6Al-4V alloy so far. Fatigue crack initiation in this microstructure was from the microstructure (α phase) and not pores or inclusions. The relatively high fatigue performance of the swaged PM compacts were attributed to the uniform precipitation of α phase inside the β grains and as well in regions near to the prior-β grain boundaries.[8,9] The sizes of the α phase were decreased by swaging of the PM compacts. The extremely fine $\alpha + \beta$ microstructure is generally more resistant to fatigue crack initiation and thus leads to improved fatigue strength both in the low-cycle and high-cycle regimes. Thus, it may be suggested that the effective method to produce a fine $\alpha + \beta$ microstructure morphology is to apply large amounts of cold working before HIPing to induce uniform microstructure recrystallization and this can be expected to reduce crack initiation site size in fatigue. It can thus be expected that proper thermomechanical processing can make the PM Ti-6Al-4V material exhibit a superior HCF performance, equaling or sometimes exceeding that of mill-annealed wrought Ti-6Al-4V alloy.

RELEVANCE TO ADDITIVELY MANUFACTURED TITANIUM

Recently, interest in additively manufactured titanium components, with a view to rapidly produce near-net shape components at low cost and reduced tooling, has been gaining momentum in many fields of titanium application. Similar to the situation in powder metallurgical processing, process parameters in additive manufacturing, including powder characteristics, deposition conditions and sintering parameters affect the mechanical quality of the article.[27,28] For example, lack of fusion pores having sizes ranging from a few to a few hundred micrometers have been found to have a drastic effect on fatigue behavior, even though the density achieved in the manufactured article is $>99.5\%$.[28–31] Similar to powder metallurgically processed titanium alloys, this necessitates the use of HIP processing and heat treatments[28–32] to improve the fatigue properties by eliminating porosity and modifying microstructure. Thus the process- and microstructure-based arguments related to improving the fatigue behavior of PM titanium alloys as discussed above also apply to additive-manufactured titanium alloys.

SUMMARY

From a critical assessment of existing literature on the fatigue of PM titanium alloys, the following conclusions can be made. The major causes of inferior fatigue performance in the PM processed Ti-6Al-4V alloys, relative to wrought Ti-6Al-4V alloy, are porosity, and coarse microstructural features, including lamellar colonies, coarse α grains or the grain boundary α phase. There is an overwhelming support in the fatigue data to the thesis that poor HCF performance can be attributed to the preferential crack initiation either at pores, coarse lamellar grains, or grain boundary α regions. It is also possible that the α/β interface cracking occurs in some fatigue tests, but there is a little evidence to support this. Regardless, a finer and more homogeneous microstructure, free from any processing and microstructural defect would result in superior fatigue properties that are comparable to or exceeding the fatigue properties of wrought Ti-6Al-4V alloy. Any PM titanium processing approach or additive manufacturing process broadly, should necessarily target to keep the sizes of the crack initiators (microstructure units or defects) sufficiently small or comparable to that in wrought materials, if the goal is to produce PM titanium alloy parts that can compete effectively with the wrought titanium alloys. These conclusions also apply to additive-manufactured titanium alloys, because of the similarities between the process defects occurring in powder metallurgical and other additive manufacturing practices.

ACKNOWLEDGEMENT

The authors gratefully acknowledge the financial support from the US Department of Energy, Innovative Manufacturing Initiative (DEEE0005761), through the Advanced Manufacturing Office and the Office of Energy Efficiency and Renewable Energy.

REFERENCES

1. R. Haynes, *Powder Metall.* 13, 465 (1970).
2. B. Zhang, D.R. Poirier, and W. Chen, *Metall. Mater. Trans. A* 30, 2659 (1999).
3. Q.G. Wang, D. Apelian, and D.A. Lados, *J. Light Metals* 1, 73 (2001).
4. C. Lin, C. Ju, and J.H. Lin, *Biomaterials* 26, 2899 (2005).
5. F. Cao, P. Kumar, M. Koopman, C. Lin, Z.Z. Fang, and K.S. Ravi Chandran, *Mater. Sci. Eng. A* 630, 139 (2015).
6. O.M. Ivasishin, D.G. Savvakin, F. Froes, V.C. Mokson, and Bondareva, *Powder Metall. Met. Ceram.* 41, 382 (2002).
7. Z.Z. Fang, P. Sun, and H. Wang, *Adv. Eng. Mater.* 14, 383 (2012).
8. G. Wirth, K.J. Grundhoff, and W. Smarsly, *SAMPE Q.* 17, 34 (1986).
9. Y.T. Lee, K.J. Grundhoff, and G. Wirth, *Zeitschrift für Metallkunde* 78, 49 (1987).
10. H. Wang and Z. Zak, Fang, and P. Sun. *Int. J Powder Metall.* 46, 45 (2010).
11. D. Eylon, R.G. Vogt, and F.H. Froes, *Modern Dev. Powder Metall.* 16, 563 (1985).

12. K.S. Ravi Chandran, Department of Metallurgical Engineering, The University of Utah, Salt Lake City, UT, Unpublished research, 2015.
13. T. Fujita, A. Ogawa, C. Ouchi, and H. Tahima, *Mater. Sci. Eng. A* 213, 148 (1996).
14. P.J. Anderson, V.M. Svoyatytsky, F.H. Froes, Y. Mahajan, and D. Eylon, *Modern Dev. Powder Metall.* 13, 537 (1981).
15. F.H. Froes, D. Eylon, and Y. Mahajan, *Modern Dev. Powder Metall.* 13, 523 (1981).
16. M. Hagiwara, Y. Kaieda, and Y. Kawabe, *Paper presented at the 114th ISIJ Meeting*, Tetsu-to-Hagane, 71, S1518 (1987) (in Japanese).
17. Y. Yan, G.L. Nash, and P. Nash, *Int. J. Fatigue* 55, 81 (2013).
18. F. Cao, K.S. Ravi Chandran, P. Kumar, P. Sun, M. Koopman, Z.Zak Fang, Department of Metallurgical Engineering, the University of Utah, Salt Lake City, UT, unpublished research, 2015.
19. J.P. Herteman, D. Eylon, and F.H. Froes, *Proceeding of the Fifth International Conference on Titanium* (Munich, Germany, 10–14 September 1984).
20. M. Hagiwara, Y. Kaieda, Y. Kawabe, and S. Miura, *ISIJ Int.* 31, 922 (1991).
21. V.S. Moxson, P. Sjoblom, and M.J. Trzcinski, *Adv. Powder Metall.* 6, 125 (1992).
22. W.R. Kerr, *Metall. Mater. Trans. A* 16, 1077 (1985).
23. R. Chait and T.S. Desisto, *Metall. Mater. Trans. A* 8, 1017 (1977).
24. K.S. Chan, *Int. J. Fatigue* 32, 1428 (2010).
25. X. Liu, C. Sun, and Y. Hong, *Mater. Sci. Eng. A* 622, 228 (2015).
26. I. Weiss, D. Eylon, M.W. Toaz, and F.H. Froes, *Metall. Trans. A* 17, 549 (1986).
27. S.T. Williams, H. Zhao, F. Leonard, F. Derguti, I. Todd, and P.B. Prangnell, *Mater. Charact.* 102, 47 (2015).
28. G. Kasperovich and J. Hausmann, *J. Mater. Proc. Tech.* 220, 202 (2015).
29. Q. Liu, J. Elambasseril, S. Sun, M. Leary, M. Brandt, and P.K. Sharp, *Adv. Mater. Res.* 891–892, 1519 (2014).
30. S. Leuders, M. Thöne, A. Riemer, T. Niendorf, T. Tröster, H.A. Richard, and H.J. Maier, *Int. J. Fatigue* 48, 300 (2013).
31. A. Mohammadhosseini, D. Fraser, S.H. Masood, and M. Jahedi, *Mater. Res. Innov.* 17, 106 (2013).
32. B. Baufeld, E. Brandl, and O. Biest, *J. Mater. Proc. Tech.* 211, 1146 (2011).

2.2 PM Titanium Using TiH_2

2.2.1 Vacuum Sintering of TiH_2

In recent years, an alternative BE PM Ti technique employs vacuum sintering of TiH_2 powders. [1,2,3] During sintering, TiH_2 will dehydrogenate at moderate temperatures prior to being sintered at high temperatures in vacuum.[1,2] Ivasishin et al.[2] showed that the sintered density can be 98.5-99.5% of the theoretical density in the as-sintered state, in contrast to 90-95% of the theoretical density when titanium powder was used. However, common to all above β-transus sintered Ti-6Al-4V alloys, the microstructures are usually large colony structures, as shown in Figure 2.6 (a), and the colony structure leads to poor tensile and fatigue strength. As reviewed in the previous section, the as-sintered large colony structure can be refined by extra postsintering processes, such as heat treatment, thermal mechanical work to achieve high tensile and fatigue strengths. All the extra processes would increase the cost of PM titanium parts, thus losing the advantage of low cost for PM Ti.

2.2.2 Benefits of Using TiH_2 as Raw Material

TiH_2 is brittle and low strength in nature (250 MPa), thus the TiH_2 particles can be easily crushed. Ivasishin et al. [4] found that the compaction of TiH_2 under pressure leads to the brittle fracture of the hydride particles, but does not increase the concentration of defects in their crystals, thus the rate of pore healing does not increase with increasing compaction pressure. Thus the use of TiH_2 powders makes it possible to attain a high theoretical density with relatively low compacting pressure. Furthermore, high active atomic hydrogen is capable of reducing metal oxide. Ivasishin et al. [4,5] illustrated that the

oxygen content in sintered alloy was somewhat lower than that in initial hydride powder. Hydrogen is released from the hydride compact, part of which reduces the surface oxide forming water vapor. The rate of sintering was thought to be markedly higher after dehydrogenation due to cleaner surfaces and activation of diffusion by crystal lattice defects formed during TiH_2 to Ti (beta) phase transformation.[4] To date, research has shown several merits of employing TiH_2 as PM Ti raw material: 1) low cost, 2) easy to compact due to low strength, 3) surface cleaning during sintering.

Hydrogen is generally an undesirable component in titanium and structural metals, due to the well-known hydrogen embrittlement. However, hydrogen can be potentially beneficial when used in Ti processing. Hydrogen can stabilize the β phase and decrease β-transus temperature. In addition, hydrogen has a rapid diffusion rate in titanium and the reaction between titanium and hydrogen is reversible. Therefore, hydrogen can be used as a temporary alloying element to improve the workability and deformability during hot working of Ti.[6] The well-known thermo-hydrogen processing (THP) utilizes hydrogen as a temporary alloying element to refine the microstructure. The THP usually first involves hydrogenation by controlled diffusion from a hydrogen environment, and then cooling down to room temperature to obtain hydride phase. During the last step, the hydrogen is removed by annealing at a moderate temperature (typically between 600 ˚C to 800 ˚C) in vacuum. It has been extensively shown that, when used correctly, hydrogen as a temporary alloying element can become powerful in improving processing and microstructure/mechanical properties of titanium alloys.

2.2.3 HSPT Process

Recently, a new PM process, HSPT, that involves sintering of TiH_2 powder in the β-phase field and obtaining the Ti-6Al-4V alloy by subsequent phase transformation and dehydrogenation, has been introduced.[7,8,9,10] The advantage of the HSPT process is that high density and very fine microstructure, as shown in Figure 2.6(b), can be achieved in the as-sintered state at moderate sintering temperatures. The raw TiH_2 powder is also less expensive than pre-alloyed (PA) titanium powders produced by the plasma-rotating-electrode process (PREP) or the liquid alloy atomization process.

The temperature-time profile of HSPT is shown in Figure 2.7. As shown in the figure, HSPT consists of three steps for Ti-6Al-4V: (1) sintering at 1200 ˚C in hydrogen, (2) phase transformation at a moderate temperature 650 ˚C in hydrogen, and (3) dehydrogenate at 750 ˚C in vacuum.[9,10] The phase transformations and microstructural evolution during HSPT are schematically shown in Figure 2.8. During HSPT, when the samples were cooled from 1200 ˚C to 650 ˚C, there was no precipitation of α, even when the temperature was below β transus. During isothermal holding at 650 ˚C, ultra-fine α precipitated, which then transformed to α2 after the sample was held for some time. The precipitation of α within the β grains and the presence of α2 are the key to attain the ultra-fine microstructure. Finally, during the dehydrogenation step, new β phase forms from the reaction of α + δ to β. Since the dehydrogenation process is conducted in the α + β phase region, the mixed phase grain boundaries would be expected to retard grain growth. Thus the final dehydrogenated microstructure primarily inherits the morphology of the microstructure before dehydrogenation.[8,9,10]

The (Ti-6Al-4V)-H phase diagram has been developed by different authors and studied extensively in the past few decades. They commonly showed β phase exists above about 1073 K (800 ˚C) in the Ti-6Al-4V-H system, at hydrogen concentrations >10 at.%.[9,1113] According to Kerr and Qazi et al.,[11,13] when hydrogen content is sufficient, below this temperature, the β phase was hypothesized to have decomposed into α and hydride phase, and this transformation is the origin of the fine microstructure. Sun et al.[10] illustrated that the precipitation of α/α_2 phase within β grains during isothermal holding (at temperatures below β-transus under hydrogen atmosphere), and the eutectoid transformation of remaining β into α and hydride phase at a lower temperature, are critical for the formation of the final fine α + β microstructure.[9,10] On this basis, in the HSPT process, the sintering of TiH_2 powder compacts occurs in the β-phase field in hydrogen atmosphere, the subsequent phase transformation and dehydrogenation of powder metallurgically sintered Ti-6Al-4V-H alloy below 1073 K (800 ˚C) produce a very fine α + β widmanstätten microstructure.[9,11,14] The mechanisms of microstructure refining were discussed in great detail by Sun et al.[9,10]

2.3 Fatigue Behavior of Engineering Alloys

2.3.1 Low and High Cycle Fatigue

Dynamic properties of titanium alloys, in which crack initiation plays a major role, can be degraded as a result of contamination levels. In the low cycle region, the grains are plastically deformed homogeneously and thus the external plastic strain amplitude is identical with plastic strain amplitude of all the grains. LCF strength is more dependent on the tensile strength of the material. The failure in LCF usually starts from the

specimen surface. Under LCF loading conditions, though plastic deformation involves large areas of a structure and causes immediate multiple-site crack initiation, the crack initiation by the formation of persistent slip bands consists of about 50 % of the total life.[15] Titanium alloys are well known to be sensitive to surface roughness and defects, such as inclusions and porosity. Thus with the presence of inclusion or porosity, LCF life would be degraded significantly. It has been shown that micro-sized porosity would not play a role in crack initiation if it is smaller than some size; the size can be as large as 50 μm.[16]

Contrary to LCF, HCF properties of titanium alloys are strongly affected by microstructure. HCF damage occurs locally, because the applied load is macroscopically elastic. Under this circumstance, only a small fraction of grains within a typical test volume have favorable conditions for cyclic plastic deformation.[15] The longest-life fracture is initiated on a completely subsurface facet, so the term near-surface is used because the slip direction did not intersect the surface of the sample, so the initiation was not caused by the classical slip band intrusion/extrusion mechanism.

2.3.2 Fatigue Behavior

In fatigue of single phase (FCC) ductile materials without inclusions, such as copper, this type of material has conventional high cycle fatigue limit, and a UHCF limit. Fatigue life in the UHCF regime is governed by surface roughening, which can lead to persistent slip band formation and subsequent crack initiation in the slip bands. Titanium alloys are relatively “clean” materials; in this sense, subsurface crack initiation is not expected. However, subsurface crack initiation which is not associated with pre-existing defects has

been reported for various titanium alloys at and below room temperature under cyclic axial loading conditions.[17] The typical S-N curve including LCF, HCF and UHCF regimes for a defect free Ti-6Al-4V alloy is shown in Figure 2.9.[17] The S-N curve of a Ti-6Al-4V alloy shows a plateau range between one million and ten million cycles as illustrated. There is a rather sharp drop in the fatigue strength between 10 million and 100 million cycles; thereafter, the curve flattens out and reaches a fatigue limit of 10^{10} cycles. The drop in fatigue strength is associated with a change in the mechanism of fatigue damage.

Steele et al.[15] compared the cyclic and monotonic stress-strain curves of copper and titanium. The stress for a lifetime of 10^7 cycles corresponds to the level at which the cyclic stress-strain curve departs from the elastic line. In contrast, the stress for a lifetime of 10 million cycles in Ti-6Al-4V is at a level well below this average strain level and in fact, all lives greater than 1000 cycles correspond to stresses below this level. Therefore, in the case of copper, the matrix itself is in the plastic region whereas in the case of Ti-6Al-4V, the matrix of the material is in the pseudo-elastic range. Internal failures are observed in HCF/UHCF range. According to Steele et al.,[15] localized crack nucleation happens quite early in life. This would mean therefore that the major portion of fatigue lifetime is spent in propagating a micro-crack to critical size.

Materials with defects, such as nonmetallic inclusions, have been described comprehensively on a microstructural basis in terms of multi-stage fatigue life diagrams by Mughrabi et al.[18] This type of materials has HCF limit, and subsurface fatigue crack initiation at inclusions is dominant in the UHCF range, provided that the inclusion density is below a critical value. A number of studies have been done to characterize the

fatigue behavior of this type of material.[19,20] This type of material often present two failure modes: surface crack induced failure in shorter life regime, and interior crack induced failure in the longer fatigue life regime. The material discontinuities, including nonmetallic inclusions, second phase particles and some inhomogeneous microstructures, play an important role in causing interior crack nucleation.

The fatigue life behavior of materials with inclusions can be described using a multi-stage Wöhler-type S-N plot, as shown schematically in Figure 2.10.[18] In reality, the transitions between the different ranges will not be sharp but gradual with some scatter and overlap. In LCF range I, failures are usually initiated at the surface. The conventional HCF regime can extend into the UHCF regime, where it is terminated with the onset of UHCF range III, in which fatigue failures occur at the stresses below the conventional HCF limit, originating in most cases from internal defects. However, some specific aspects have remained open, such as fatigue crack initiation and early slow crack growth as life-controlling factors, life-controlling factors in ranges I-III and in the transition from surface to internal failure.

PM materials unavoidably contain inclusion, porosity, and extremely large grains due to local compositional segregation. Microscopically localized deformation is always related to the microstructural heterogeneity such as nonmetallic inclusions, pores, second phase particles and grain boundaries, which are sites for local stress concentration. A comparatively larger pre-existing defect in the specimen interior may introduce higher stress concentration than the surface flaws. Especially at lower cyclic stress, the difference is considered to become more distinct, since the extrusion-intrusion mechanism becomes less active, the formation of PSBs needs a plastic strain amplitude

over 10^{-5}, and the size of the pre-existing defect is unchangeable. On the contrary, when the pre-existing defect is very small, the specimen might be immune from the defect-nucleation-crack at any cyclic stress level. Thus, it is considered that the site or Stage I crack which is selected for fatal crack is always competitive and depends on its size, shape, location in specimen and stress concentration at the tip.

It can be expected that microstructural discontinuities play a significant role of fatigue crack initiation in these high cycle or very high cycle regimes[21]. Grain size at the high end of size distribution, grain orientation was associated with the crack initiation process.[21] The fatigue behavior of engineering alloys at different stress amplitudes become strongly dependent on the microstructure heterogeneity level and the probability of the occurrence of critical heterogeneities.

2.4 HCF Crack Initiation and Small Crack Propagation in Ti-6Al-4V Alloy

2.4.1 Crack Initiation

There was good agreement in the strain heterogeneity localization in HCF failures of titanium alloys. Both experiment and crystal plasticity predictions demonstrate that the heterogeneity is established early in cyclic loading and the localization correlates closely with the crack nucleation site.[22] There is also evidence that slip band crack separation due to accumulated fatigue damage may be the operating mechanism of crack initiation. Slip along basal and prismatic planes in the primary α nodule has been proved by investigating the cyclic plasticity activity on a large number of grains. Cracks formed from the prismatic and basal slip planes.[23] Schmid factor also appears as a relevant parameter to describe crack formation in prismatic planes. On the contrary, fatigue

damage in the basal plane results from a combination of a relatively high resolved shear stress in the basal plane and a high tensile stress perpendicular to the basal plane. Other grains, which are referred to as poorly oriented, will be plastically hard compared to neighboring grains and will undergo a lower level of deformation in order to maintain compatibility; neighboring grains which have a high Schmid factor for slip on either prism or basal planes will need to undergo higher levels of deformation, accommodating the plastic strain gradient and consequent geometrically necessary dislocation (GND) multiplication compared to the macroscopic strain. Samples tested in both fatigue and dwell fatigue show elevated levels of GND storage, which is distributed inhomogeneously between grains.[24] As illustrated by Steele et al.,[15] as well as other researchers,[23,24] the HCF crack initiation in titanium is caused by deformation incompatibility induced strain accumulation.

The slip bands are generated during fatigue and the accumulation of damage within the bands, and eventually reduce the transverse strength of the materials in these bands; therefore, cracks easily propagate along the bands. This fracture proceeds rapidly until the slip-induced damage is insufficient to reduce the local toughness below the locally applied stress intensity. For small cracks, this occurs at one of the boundaries, where the crack is arrested. The crack must then await slip-imposed damage to occur in an adjacent microstructural element for the process to repeat itself.[25]

Fatigue cracks initiated predominantly either at GBs or at slip bands in the vicinity of GBs, indicating that the GB constraint plays the most important role in the crack initiation for the titanium alloy. Crack preferentially occurs if the trace of GB lies at an

angle of 30-90˚ with respect to the loading direction. This condition guarantees a large driving force for the separation of GBs.[26]

2.4.2 Near Threshold Crack Growth

The importance of the fatigue crack initiation stage was stressed repeatedly. However, the remaining difficulty lies in drawing the borderline between the initiation and propagation stages. The current crack growth, including microstructural small crack, physically small crack, and long crack, was revealed from the traditional LEFM, which is when the applied stress intensity factor (SIF) range was expressed in terms of the remote stress range and a crack length.

The propagation behavior of these so-called microstructural short fatigue cracks is strongly affected by microstructural properties, such as the grain size and the presence of phase boundaries. Because of the strong interactions of short cracks with microstructural features (grain boundaries) and their substantially different crack growth mechanisms (Stage I) compared to long cracks, the crack propagation rate of short cracks cannot be described by LEFM.[27,28] The plastic slip ahead of the growing micro-crack is blocked by grain and phase boundaries. Once critical shear stress on a slip plane in the neighboring grain is reached, the plastic deformation and crack can propagate into the next grain. Thus, the crack decelerates when approaching a boundary and accelerates after passing this barrier, resulting in an oscillating crack growth rate.[28] Apart from crystallographic aspects, the mutual interaction of short cracks has also a marked influence on the short crack growth behavior. The large cracks grow usually from short cracks by a crack coalescence mechanism.[29]

HCF and very HCF failure of Ti-6Al-4V alloy are usually associated with subsurface crack initiation.[30, 31,32] Subsurface crack initiation in Ti-6Al-4V was discovered in the 70s in high cycle and very high cycle fatigue regime. Jha[33,34] et al. also found the duality of S-N curves in α + β titanium alloys that do not contain inclusion; the origin of duality in these materials seems to be entirely originated from microstructure. Facet and fine granular near crack origins are two features usually found in subsurface fatigue failures in titanium alloys. Though their formation mechanism is not very clear so far, the formation mechanism of facet in subsurface failures already draws a lot of attention and is extensively investigated in terms of formation microstructure and mechanism.[32, 35-39] Fine granular regions in subsurface failure of titanium alloys were discovered recently.[35,39,40] Oguma et al.[40] found that the crack propagation rate of titanium alloy under vacuum is much lower than that in air, especially at a low stress intensity factor regime, and vacuum environment is essential for the formation of granular. A. J. McEvily et al.[38] illustrated that the formation of granules in titanium alloy is because the absence of oxygen allows a wear process to take place in stage 2a which reduces the local crack closure level and thereby enables very slow crack propagation. Shanyavskiy et al.[32, 41] illustrated that regions near the inclusion are highly overstressed by hydrostatic compression or tension, and the rounded granular forms due to an elemental diffusion process under twisting plastic flow near the crack origin, usually an inclusion. Chai et al.[42] revealed that the formation of fine grains at near threshold zone is a cyclic plastic deformation-induced dislocation of subcells with low angle grain boundaries.

It has been shown that in the HCF region, an internally short crack grows at an applied SIF range significantly less than the long crack fatigue threshold and has its own

characteristics. There is a considerable interaction between the microstructurally small crack and microstructure; the HCF resistance is therefore primarily due to the difficulty of overcoming a stage I crack. Though the underline mechanism is not clear to date, that the crack can grow below the LEFM threshold condition is an overall agreement.

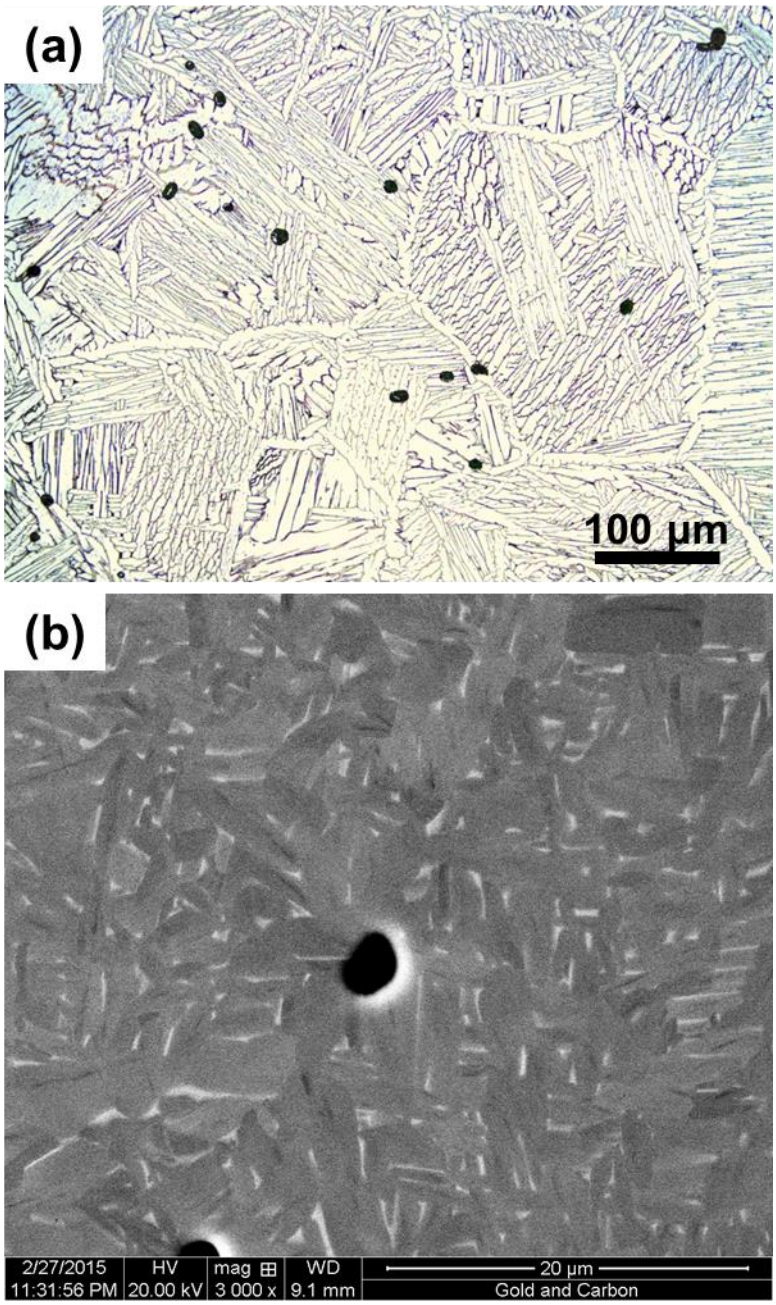

Figure 2.6 Microstructures of Ti-6Al-4V alloys produced from TiH_2 powder, (a) vacuum sintered (optical image), (b) HSPT (SEM image).

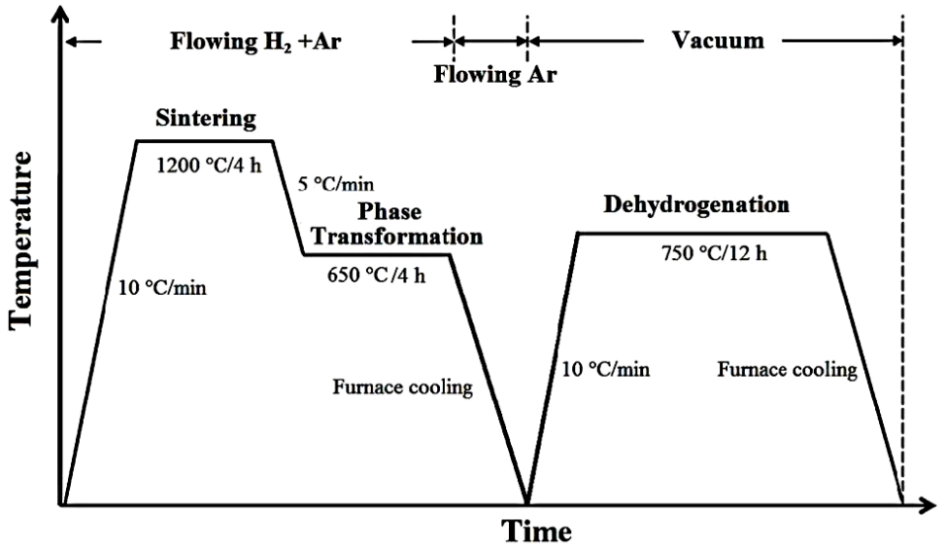

Figure 2.7 The temperature-time profiles of HSPT. Reprinted from P. Sun, Z.Z. Fang, M. Koopman, Y. Xia, J. Paramore, K.S. Ravi Chandran, Y. Ren, and J. Lu, Metall. Mater. Trans. A (46) 2015 1-15[10] with permission from Spinger.

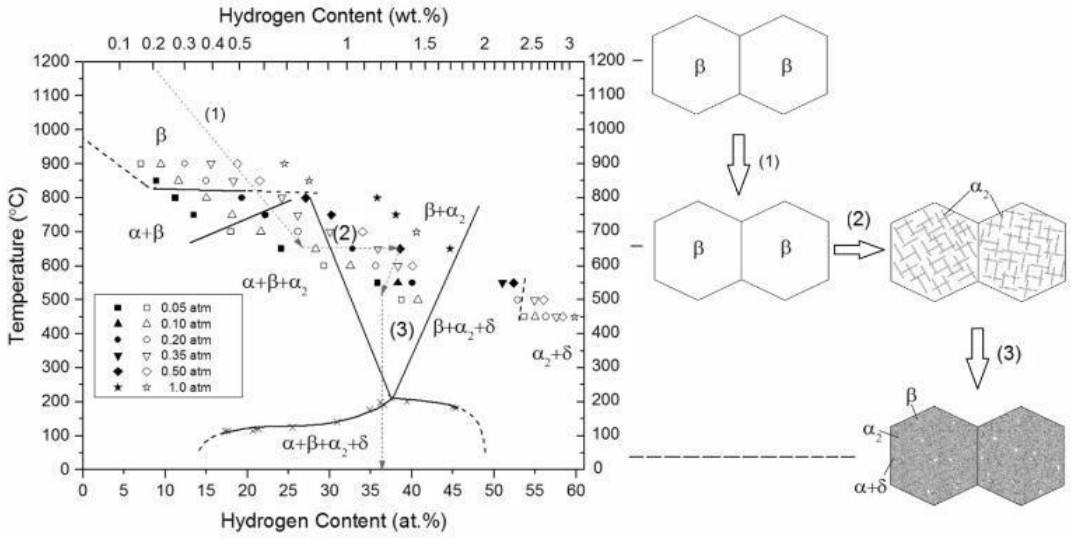

Figure 2.8 Phase transformation and microstructural evolution during (1) cooling from 1200 ˚C to 650 ˚C in hydrogen, (2) isothermal hold at 650 ˚C in hydrogen, and (3) cooling from 650 ˚C to room temperature in argon. Reprinted from P. Sun, Z.Z. Fang, M. Koopman, Y. Xia, J. Paramore, K.S. Ravi Chandran, Y. Ren, and J. Lu, Metall. Mater. Trans. A (46) 2015 1-15[10] with permission from Springer.

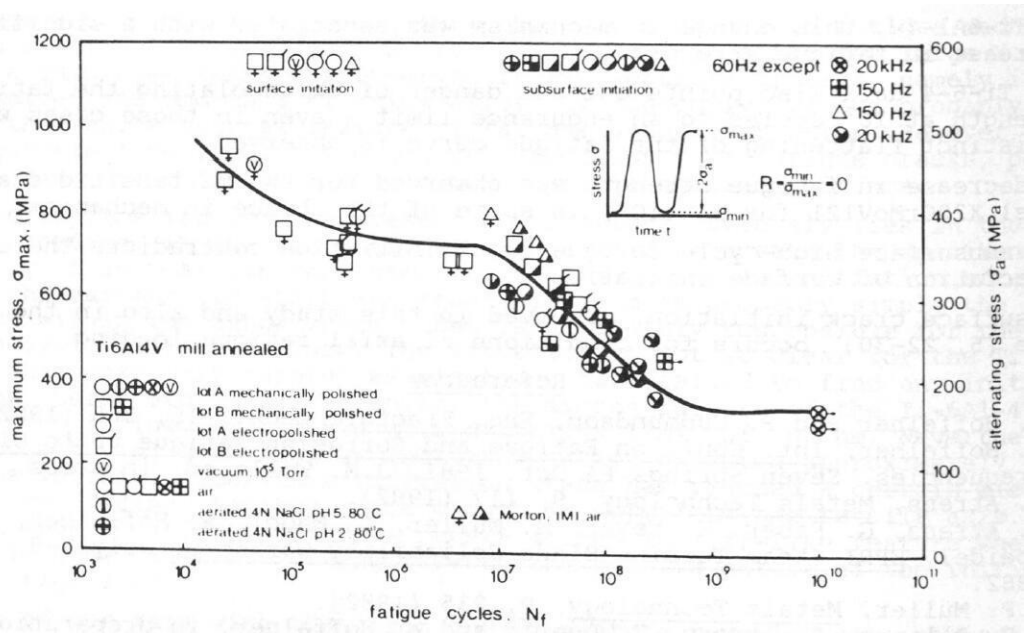

Figure 2.9 The fatigue curve for Ti-6Al-4V shows a change in crack initiation mechanism between 10^7 and 10^8 cycles. Reprinted from R.K. Steele, and A.J. McEvily, Eng. Fract. Mech. 8 (1976) 31-37[15] with permission from Elsevier.

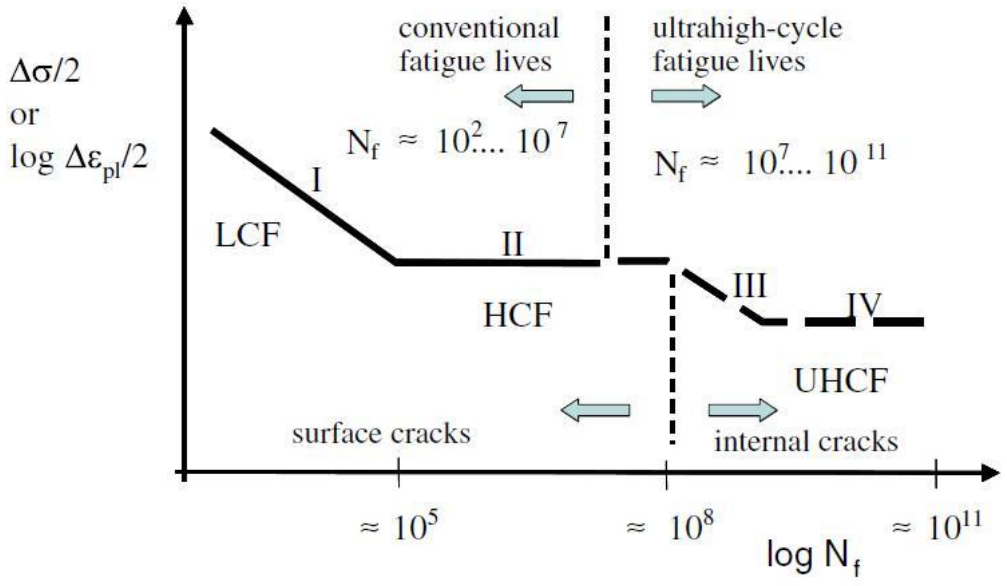

Figure 2.10 Schematic fatigue life diagram of material containing inclusions. Reprinted from H. Mughrabi, Int. J. Fatigue 28 (2006) 1501-1508[18] with permission from Elsevier.

2.5 References

1. O.M. Invasishin, V.M. Anokhin, A.N. Demidik, and D.G. Savvakin, Key Eng. Mater. 188 (2000) 55-62.

2. O.M. Ivasishin,D.G. Savvakin, V.S. Moxson, K.A. Bondareval , and F.H. Froes, Mater. Technol. 17 (2002) 20-25.

3. C.R.F. Azevedo, D. Rodrigues, and F.B. Neto, J. Alloys Comp. 353 (2003) 217-227.

4. O.M. Ivasishin, D.G. Savvakin, F. Froes, V.C. Mokson, and K.A. Bondareva, Powder Metall. Metal Cer. 41 (2002) 382-390.

5. O.M. Ivasishin, and D.G. Savvakin, Key Eng. Mater. 436 (2010) 113-121.

6. U. Zeicker, and W.S. Hans, U.S. Patent 2892742 A, 1959.

7. Z.Z. Fang, P. Sun, and H. Wang, Adv. Eng. Mater. 14 (2012) 383-387.

8. P. Sun, Z. Z. Fang, and M. Koopman, Adv. Eng. Mater. 15(10) (2013) 1007-1013.

9. P. Sun, Z. Z. Fang, M. Koopman, J. Paramore, K.S. Ravi Chandran, Y. Ren, and J. Lu: Acta Mater. (84) 2015 29-41.

10. P. Sun, Z.Z. Fang, M. Koopman, Y. Xia, J. Paramore, K.S. Ravi Chandran, Y. Ren, and J. Lu, Metall. Mater. Trans. A (46) 2015 1-15.

11. W.R. Kerr, P.R. Smith, M.E. Rosenblum, F.J. Gurney, Y.R. Mahajan, and L.R. Bidwell: Titanium ’80, Science and Technology, Proceedings of the 4th International Conference on Titanium., Metall. Soc. of AIME, Kyoto, Japan, 1980, 2477-2486.

12. W.R. Kerr, Metall. Mater. Trans. A 16 (1985) 1077-1087.

13. J. Qazi, J. Rahim, F. Froes, O. Senkov, and A. Genc, Metall. Mater. Trans. A 32 (2001) 2453-2463.

14. D.H. Kohn, and P. Ducheyne, J. Mater. Sci. 26 (1991) 534-544.

15. R.K. Steele, and A.J. McEvily, Eng. Fract. Mech. 8 (1976) 31-37.

16. D. Eylon, F.H. Froes, D.G. Haggie, P.A. Blenkinsop, and R.W. Gardiner, Metall. Trans. A 14 (1983) 2497-2505.

17. A. Atrens, W. Hoffelner, T.W. Duerig, and J.E. Allison, Scripta Metall. 17 (1983) 601-606.

18. H. Mughrabi, Int. J. Fatigue 28 (2006) 1501-1508.

19. W. Li, H. Tuan, Z. Sun, and Z. Zhang, Int. J. Fatigue 64 (2014) 42-53.

20. Z. Lei, Y. Hong, J. Xie, C. Sun, and A. Zhao, Mater. Sci. Eng. A 558 (2012) 234-241.

21. J. Miao, T. M. Pollock, and J. W. Jones, Acta Mater. 60 (2012) 2840-2854.

22. M.R. Bache, F.P.E. Dunne, and C. Madrigal, J. Strain Analysis 45 (2010) 391-399.

23. F. Bridier, P. Villechaise, and J. Mendez, Acta Mater. 56 (2008) 3951-3962.

24. P. D. Littlewood, and A. J. Wilkinson, Acta Mater. 60 (2012) 5516-5525.

25. J. A. Hall, Int. J. Fatigue 19 (1997) 23-37.

26. Y. M. Hu, W. Floer, U. Krupp, and H. J. Christ, Mater. Sci. Eng. A 278 (2000) 170-180.

27. H. J. Christ, O. Duber, C. P. Fritzen, H. Knobbe, P. Koster, U. Krupp, and B. Kunkler, Comput. Mater. Sci. 46 (2009) 561-565.

28. B. Kunkler, O. Duber, P. Koster, U. Krupp, C. P. Fritzen, and H. J. Christ, Eng. Fract. Mech. 75 (2008) 715-725.

29. Y. M. Hu, W. Floer, U. Krupp, and H. J. Christ, Mater. Sci. Eng. A 278 (2000) 170-180.

30. D.F. Neal, and P.A. Blenkinsop, Acta Metall. 24 (1976) 59-63.

31. O. Umezawa, and K. Nagai, ISIJ Int. 37 (1997) 1170-1179.

32. A. Shanyavskiy, and M. Banov. Eng. Fract. Mech. 77 (2010) 1896-1906.

33. S.K. Jha, J.M. Larsen, and A.H. Rosenberger, Acta Mater. 53 (2005) 1293-1304.

34. S.K. Jha, J.M. Larsen, and A.H. Rosenberger, and G.A. Hartman, Scripta Mater. 48 (2003) 1637-1642.

35. X. Liu, C. Sun, and Y. Hong, Mater. Sci. Eng. A 622 (2015) 228-235.

36. M. Hagiwara, and S. Emura, Mater. Sci. Eng. A 352 (2003) 85-92.

37. D. Eylon, Metall. Trans. 10 A (1979) 311-317.

38. S. Jha, C.J. Szczepanski, R. John, and J.M. Larsen, Acta Mater. 82 (2015) 378-395.

39. A.J. McEvily, T. Nakamura, H. Oguma, K. Yamashita, H. Matsunaga, and M. Endo, Script Mater. 59 (2008) 1207-1209.

40. H. Oguma, and T. Nakamura, Int. J. Fatigue 50 (2013) 89-93.

41. A. A. Shanyavskiy, Eng. Fract. Mech. 110 (2013) 350-363.

42. G. Chai, Mater. Sci. Forum 783-786 (2014) 2266-2271.

CHAPTER 3

MATERIALS AND EXPERIMENTAL PROCEDURE

3.1 Materials Fabrication

The as-received TiH_2 powders (Reading Alloys, Ametek, Robesonia, PA) had a size range of -20/+60 mesh. The powders were milled in a home-made jar under argon atmosphere for 30 minutes with a speed of 80 rpm, and then sieved to obtain -325 or -400 mesh powders. The sieved TiH_2 powders were mixed with -400 mesh 60Al/40V master alloy powder (sieved from the -325 mesh powder provided by Reading Alloys, Ametek, Robesonia, PA). The TiH_2 particles are generally angular in shape. The mean particle diameters for the -325 and -400 mesh powders were 25.3 μm and 20.6 μm, respectively.

Cylindrical Ti-6Al-4V bars were made by following the HSPT process. The details of the process were described in Chapter 2 section 2.2.3. Specifically, the process involves first cold-isostatic-pressing (CIP) of the mixed TiH_2 and 60Al/40V master alloy powder at 350 MPa. After CIP, the green compacts were sintered at 1473 K (1200 ˚C) for 4 or 8 hours in a flowing atmosphere of Ar/H_2 (50/50) mixture. The sintered samples were then phase-transformed by furnace cooling to and holding at 923 K (650 ˚C) for 4 hours. This was followed by dehydrogenation at 1023 K (750 ˚C) for 12 hours to yield a Ti-6Al-4V alloy with fine α + β microstructure. Sintered bars were pneumatic-isostatic-forged (PIFed) at Ametek Inc. at 1123 K (850 ˚C) for a short time (5-10 minutes). The

chemical composition of the sintered Ti-6Al-4V PM alloy was determined by ICP-MS analysis. The densities of the materials were determined using the Archimedes' principle. The size distribution of the pores was determined on metallographically polished sections, using ImageJ software, over 10 mm^2 areas. Microstructures were examined in an optical microscope and an SEM equipped with an EBSD detector.

3.2 Tensile and Fatigue Testing

Tensile properties were determined using samples made according to the ASTM-E8 standard and tested at a strain rate of 0.002 S^{-1} at room temperature; the sample dimensions are shown in Figure 3.1. Fatigue specimens, as shown in Figure 3.2, having a total length of 3'' were machined from sintered blanks. The test section was 0.25" in diameter and 0.5" in length. The test sections were polished using SiC paper until grade 1200, followed by finishing with 1 μm alumina suspension to obtain surfaces free from machining damage and residual stress. Tension-tension fatigue tests were conducted under load control with a cyclic frequency of 35 Hz (sine wave), at a stress ratio ($\sigma_{min}/\sigma_{max}$) of 0.1, in a 100 KN MTS 810 testing system. The fatigue tests were conducted in laboratory air at room temperature. The wrought Ti-6Al-4V alloy specimens in mill-annealed condition were also tested in the same condition for fatigue performance comparison. Replicate tests were made until the stress-versus-fatigue-life trends were clearly revealed in the data. Fatigue fracture surfaces were examined in an SEM.

3.3 Fatigue Crack Growth Testing

Fatigue crack growth was studied using miniature single edge-notched tension (SENT) specimens. Each specimen was loaded at constant stress amplitude over the entire period of fatigue crack growth. The specimen geometry is shown in Figure 3.3. The specimens were made from cylindrical Ti-6Al-4V bars of about 0.55" in diameter and 3" in length. The test section conformed to the SENT geometry and had a specimen thickness of 0.1" and a width of 0.5". The height-to-width ratio (h/W=2.5) of the test section is larger than the minimum fracture mechanics requirement. Specimens were uniformly stressed by concentric gripping at the cylindrical ends, using hydraulic grips. Starter notches (~0.01" to 0.1" in depth) were machined by EDM to initiate the pre-cracks. The root radius of the EDM notch was about 0.05" and at least a pre-crack growth of 0.1" from the notch root was allowed before crack growth was recorded. Crack lengths on both sides agreed with each other within a few percent. Fatigue crack growth tests were done at room temperature, at a stress ratio of 0.1 and at 35 Hz. The solution for ΔK values was developed by a 2D finite element model for the SENT geometry. Crack lengths were measured using a travelling microscope with a 40X objective lens. The crack growth set-up is shown in Figure 3.4. Crack growth rates were determined using two successive crack length measurements and the corresponding cycle counts.

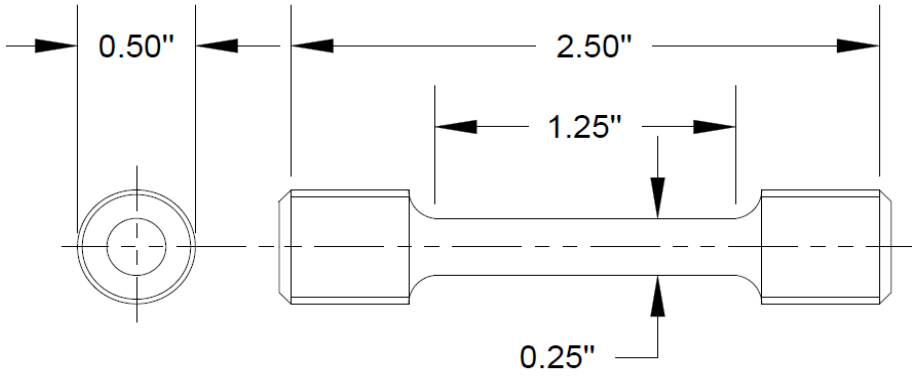

Figure 3.1 Dimensions of tensile specimen.

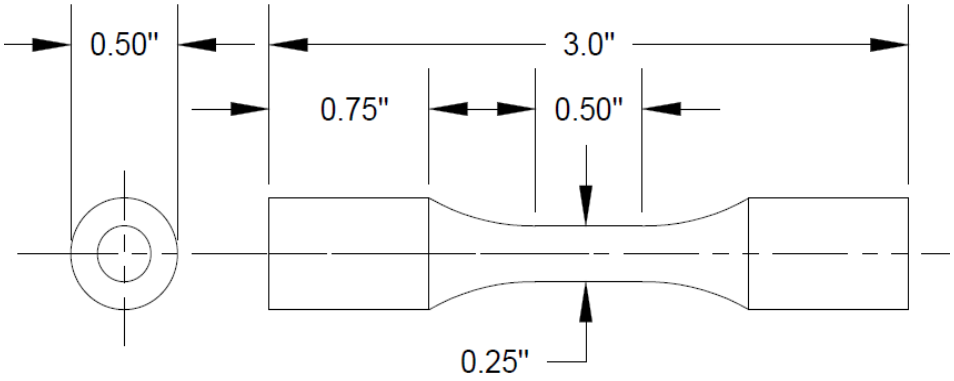

Figure 3.2 Dimension of fatigue specimen.

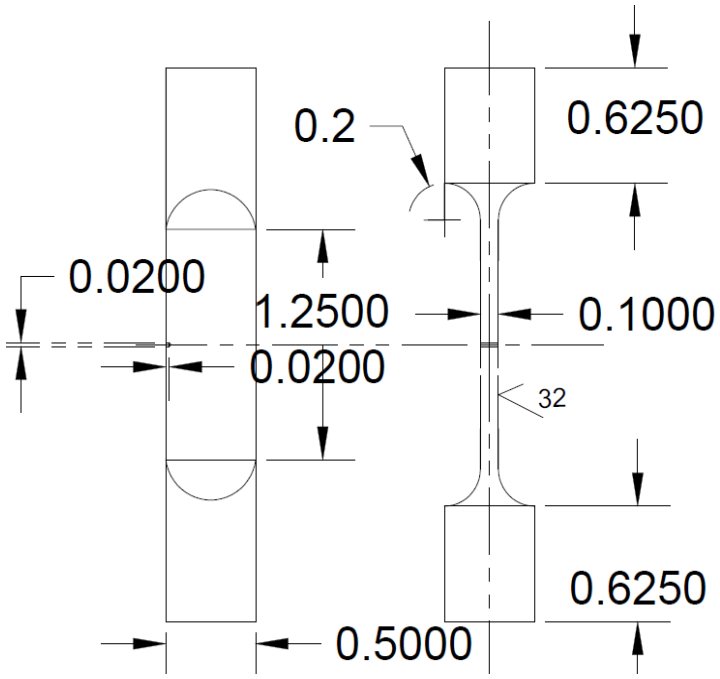

Figure 3.3 SENT specimen dimensions.

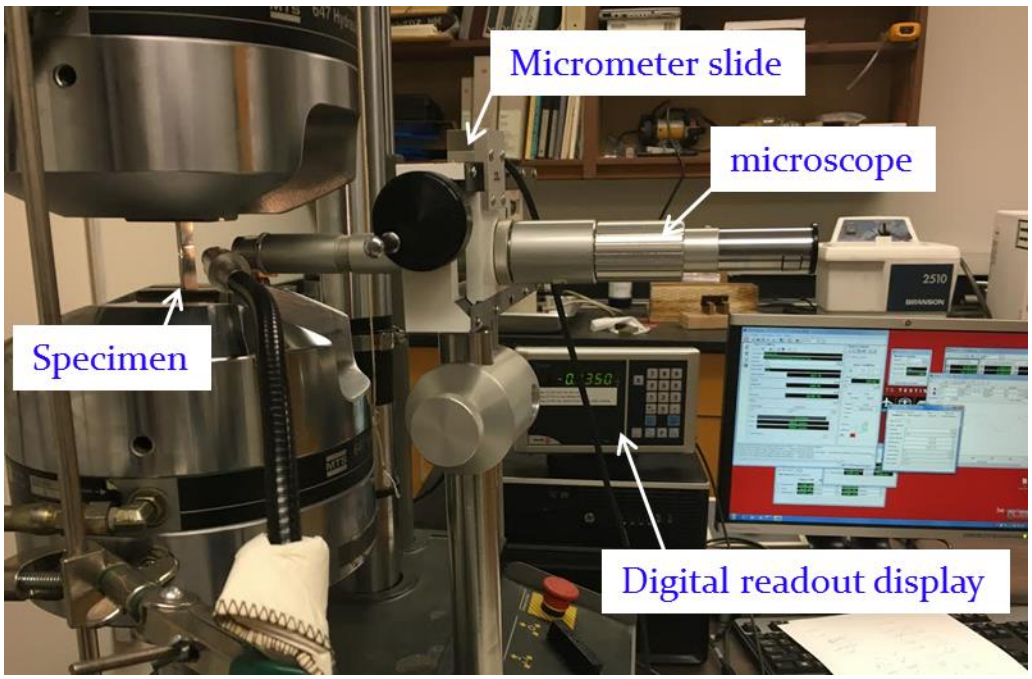

Figure 3.4 Fatigue crack growth set-up.

CHAPTER 4

ROLE OF CRACK INITIATION AND DUALITY OF FATIGUE RESPONSE

Published as :

F. Cao, P. Kumar, M. Koopman, C. Lin, Z.Z. Fang, and K.S. Ravi Chandran

Understanding Competing Fatigue Mechanisms in Powder Metallurgy Ti-6Al-4V Alloy: Role of Crack Initiation and Duality of Fatigue Response

Materials Science & Engineering A, April 2015, volume 630, pp. 139-145

Materials Science & Engineering A 630 (2015) 139–145

Contents lists available at ScienceDirect

Materials Science & Engineering A

journal homepage: www.elsevier.com/locate/msea

Understanding competing fatigue mechanisms in powder metallurgy Ti–6Al–4V alloy: Role of crack initiation and duality of fatigue response

Fei Cao, Pankaj Kumar, Mark Koopman, Chenluh Lin, Z. Zak Fang, K.S. Ravi Chandran *

Department of Metallurgical Engineering, University of Utah, Salt Lake City, UT, USA

ARTICLE INFO

Article history:
Received 25 November 2014
Received in revised form
10 February 2015
Accepted 11 February 2015
Available online 20 February 2015

Keywords:
Fatigue
Ti–6Al–4V
Powder metallurgy
Crack initiation
Porosity

ABSTRACT

Multiple mechanisms of fatigue crack initiations from pores leading to short-term and long-term fatigue life have been observed in a powder metallurgy (PM) Ti–6Al–4V alloy made by the hydrogen sintering and phase transformations (HSPT) process. The pores in the sintered alloy could be classified into two groups; type-I being caused by particle interstices that did not fully close during sintering (sinter-pores) and the type-II originating from larger voids that did not close during powder packing (cave-pores). The fatigue life trends can be classified by the type and the location of pore from which the crack initiated. Interestingly, the two types of pores, and the two different locations (surface versus interior) from which the cracks initiated lead to four distinct S–N trends in the fatigue data. When the stress amplitude level and the pore size were accounted for through initial stress intensity factors, the fatigue data reduced to dual S–N fatigue curves. The results offer new insights into how pores, especially their type and size, and location control the fatigue behavior of PM Ti–6Al–4V alloy. Large improvements in fatigue life can be obtained if the large cave-pores are eliminated or their volume density reduced to very low levels.

1. Introduction

Powder metallurgy (PM) offers many unique advantages for the mass production of near-net-shape titanium components [1,2]. The major technical barrier for the adoption of titanium PM parts, in fatigue critical applications, is that even a small amount of porosity can severely degrade fatigue life. The effect of residual pores or defects in reducing fatigue life has been extensively studied in the past [3–12]. However, the conclusions of most of these studies are somewhat expected, in that, the pores have been found to reduce the fatigue life. The concentration of cyclic stress at the surface of the pore leads to early fatigue crack initiation; therefore most of the fatigue life is controlled by propagating the crack [6,9,11]. Fatigue data of PM titanium alloys also exhibit large scatter, presumably due to random occurrence of pores of varying size in the specimen. Therefore, it is highly probable that a correlation exists between pore size and/or its physical location (surface versus interior) and the fatigue life.

The present work investigates the fatigue mechanisms in a PM Ti–6Al–4V alloy made by hydrogen sintering and phase transformations (HSPT). In this process, the material is sintered in the β phase field of the Ti–H system followed by phase transformations to reduce the grain size [13–16]. Although α-grain size was reduced in these materials, the residual pores strongly influence the fatigue behavior. The question of how the pore parameters affect the fatigue behavior was investigated in this work. In this PM Ti–6Al–4V alloy, it has been found that there are two different types of pores. The purpose of this work is to understand how the pore type, size and location affect the fatigue behavior in this HSPT Ti–6Al–4V alloy.

In fatigue of titanium alloys, there are additional complicating aspects such as the recently discovered duality in fatigue behavior [17–20] and the two-stage S–N behavior [21–23] where surface and interior crack initiations compete to cause fatigue failure. The duality is caused by the competition between surface and interior crack nucleation from primary-α particle clusters [17,18]. Generally, surface crack initiations occur at high stresses, and the associated fatigue life is relatively short because of the environmental effect (from ambient atmosphere) on fatigue crack growth. The crack initiations from interior defects generally lead to long life because of crack growth in a quasi-vacuum environment. This competition in fatigue failure between surface-initiated and interior-initiated cracks may also be present in PM titanium alloys, but there has been no such prior study. Such a study would not only be relevant to the emerging field of PM titanium, but also of particular note from a materials science perspective because the cracks initiate from pores of varying size, location and morphology. Further, interior crack initiation, not associated with any defects can also occur in titanium alloys [23]. In such a case, crack initiation shifts from the surface to the interior, creating a "step" in the S–N curve at lower stress levels [18,22,24]. The reason for the

* Corresponding author. Tel.: +1 801 581 6386.
E-mail address: Ravi.Chandran@utah.edu (K.S.R. Chandran).

http://dx.doi.org/10.1016/j.msea.2015.02.028
0921-5093/

transition in fatigue mechanism and the formation of the step has not yet been adequately explained. There can be additional microstructural factors that affect the fatigue behavior, as well. For example, grain boundary alpha phase (GB-α) that forms under certain microstructural conditions can alter the crack initiation mechanism. Thus the S–N curve or fatigue life can be complex in PM titanium alloys due to pores and microstructure variables.

The objective of this study is to investigate the competing fatigue crack initiation mechanisms from pores in PM Ti–6Al–4V fabricated by HSPT, and to establish clear correlations between the size and location of pores and fatigue life. It is shown that the two types of pores (sinter-pores and cave-pores) lead to complex fatigue failures. Each type of pore and its location (surface or interior), has its own S–N curve. It is also shown that based on the initial stress intensity factor, the fatigue life trends can be effectively rationalized into two S–N curves, confirming that dual fatigue failure response also occurs in the present material.

2. Material and experimental procedure

The PM Ti–6Al–4V alloy bars were 15 mm in diameter and 80 mm in length, and were fabricated from titanium hydride powder following the HSPT process described elsewhere [13]. Basically, the process involves first cold isostatic pressing (CIP) of TiH_2 powder (−325 mesh, average particle size is 17 μm, acquired from Reading Ametek) blended with 60 wt% Al–40 wt% V master alloy powder (−325 mesh, average particle size is 16 μm). The proportion of master alloy powders was selected according to the chemical composition of Ti–6Al–4V alloy. After CIP, the samples were sintered at 1200 °C for 4 h in a flowing atmosphere of Ar/H_2 (50/50) gas mixture. The sintered samples were then phase-transformed through eutectoid temperature and held at 650 °C for 4 h. This was followed by dehydrogenation at 750 °C for 12 h to yield solid Ti–6Al–4V alloy with a homogeneous and fine α+β microstructure. The average sintered density achieved after the processing was 99.4%. The chemical composition of the sintered Ti–6Al–4V PM alloy was determined to be (in wt%): 5.99 Al, 3.84 V, 0.42 O, 0.008 N, and 0.0005 H.

Three dimensional X-ray microtomographic imaging was performed on the cold isostatic pressed powder compact and the sintered alloy to map the distribution of residual pores. The imaging was done using an Xradia (model: micro XCT-400) high-resolution X-ray microtomographic unit. The tomographic scan was performed with a peak X-ray voltage of 80 kV with the specimen rotating along its axis. A total of 994 2-D radiographs were obtained. The 2-D radiographs were reconstructed to obtain 3-D X-ray image with a voxel of 4.59 μm × 4.59 μm × 4.59 μm. This enabled 3D visualization of pores of size 5 μm and above.

The sintered bars were machined to produce cylindrical fatigue specimens, each having a total length of 76.2 mm. The gauge sections were 6.35 mm in diameter and 12.7 mm in length. The test sections were polished using several grades of silicon carbide paper until grade 1200, followed by finishing with 1 μm alumina suspension to obtain surfaces free from machining or polishing-induced damage. Tension–tension fatigue tests were conducted under load control with a cyclic frequency of 35 Hz (sine wave) at a stress ratio ($\sigma_{min}/\sigma_{max}$) of 0.1. The fatigue tests were conducted in laboratory air and at room temperature. Fatigue fracture surfaces were examined in an SEM to determine the characteristics of fatigue crack initiation. The areas (A_p) of initiating pores present on the fracture surfaces were determined using the ImageJ software. For each pore, the equivalent circular diameter ($D_e = \sqrt{4A_p/\pi}$) was calculated.

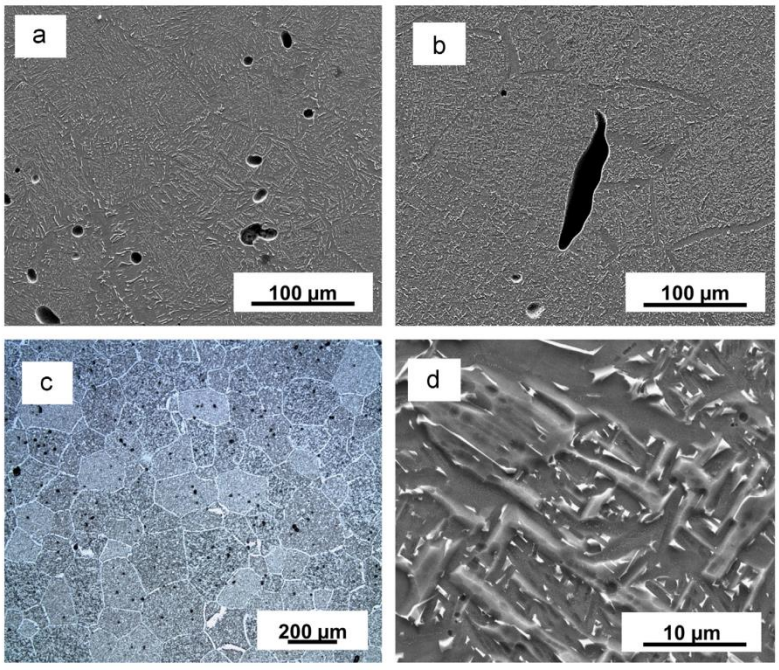

Fig. 1. Microstructures of PM Ti–6Al–4V alloy densified by HSPT (a) residual sinter-pores, (b) a large cave-pore, originating from big void that existed before sintering, (c) the overall microstructure including the prior-beta grain boundaries and (d) SEM micrograph of the fine α+β microstructure.

3. Result and discussion

3.1. Microstructures and fatigue failure initiations of PM Ti–6Al–4V

The microstructure and pore types of the PM Ti–6Al–4V alloy are shown in Fig. 1. Fig. 1(a) shows typical small pores with rounded edges (termed, "sinter-pores"), which are the most common in the microstructure. The rounded edges suggest that these pores evolved from prior interstitial spaces between the TiH_2 particles, by creep flow of matter along the edges during sintering. Fig. 1(b) shows an example of large pores (termed, "cave-pores") that are present in the microstructure in far fewer numbers relative to sinter-pores. They are thought to originate from larger voids formed by particles that had locked-in before sintering to form gaps between poorly packed particles. Fig. 2(a) shows the 3D distribution of pores in the cold pressed green compact before sintering as determined by X-ray microtomography. Fig. 2(b) is an arbitrary slice through the volume of a specimen showing the presence of large ($>100\ \mu m$) cave-pores, possibly due to local locking of titanium hydride particles during CIP. Because the titanium hydride particles are angular and their flowability is poor, formation of caves during particle packing in the green state can be expected. Fig. 2(c) shows the presence of a large cave-pore and some small sinter-pores in an arbitrary 2D slice through the 3D microtomographic construction image of the sintered specimen. The full 3D image is shown in Fig. 2(d).

When all the fatigue tests results were reviewed, it was found that fatigue failures occurred due to cracks starting from either of the two pore types. For the crack initiation pores, the equivalent diameters (approximated to circles having the same total pore area measured on the fracture surface) ranged from 20 to 340 μm. The distribution of these pore diameters are presented in the form of the largest extreme value distribution (LEVD) plots in Fig. 3. The extreme value distribution plotting is a well-established method of presentation of the defect distribution in a material, and is discussed in detail elsewhere [25]. In this method, the pore diameters are ranked in order from small to large, and the cumulative ranking is determined. The cumulative rank is given by

$$P_j = -\ln(-\ln(F_j))$$

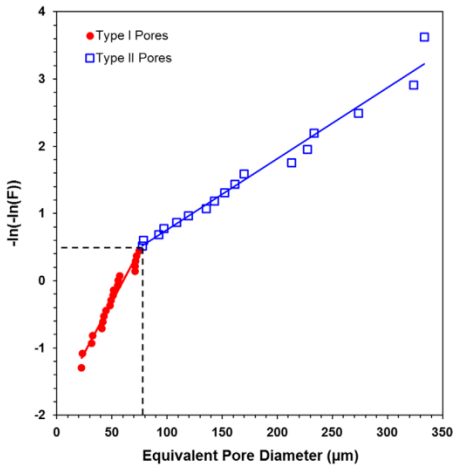

Fig. 3. Largest extreme value distribution plot of fatigue crack initiating pores in the PM Ti–6Al–4V alloy.

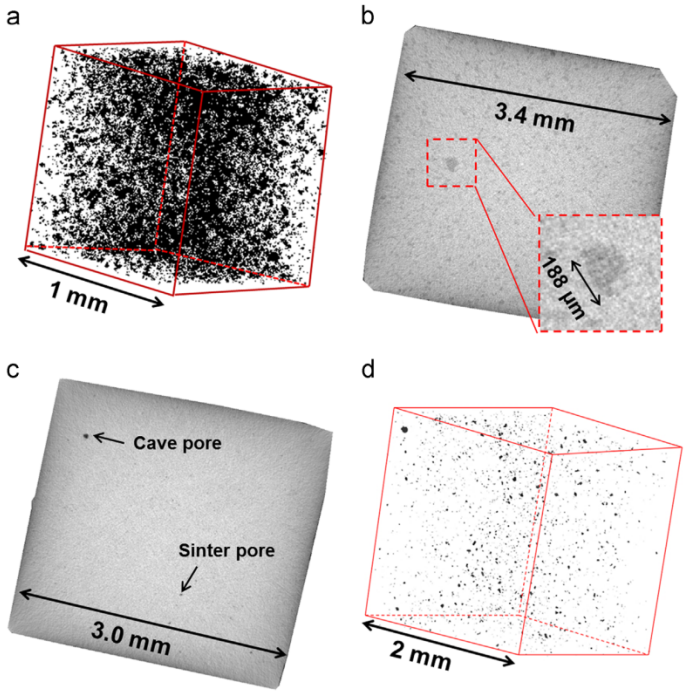

Fig. 2. X-ray microtomographic imaging showing the size and distribution of pores (a) 3D reconstructed image of a cold isostatic pressed powder compact, (b) an arbitrary 2D radiograph showing the presence of a cave, (c) a 2D slice of as-sintered Ti–6Al–4V alloy specimen, and (d) 3D reconstruction of as-sintered Ti–6Al–4V alloy specimen.

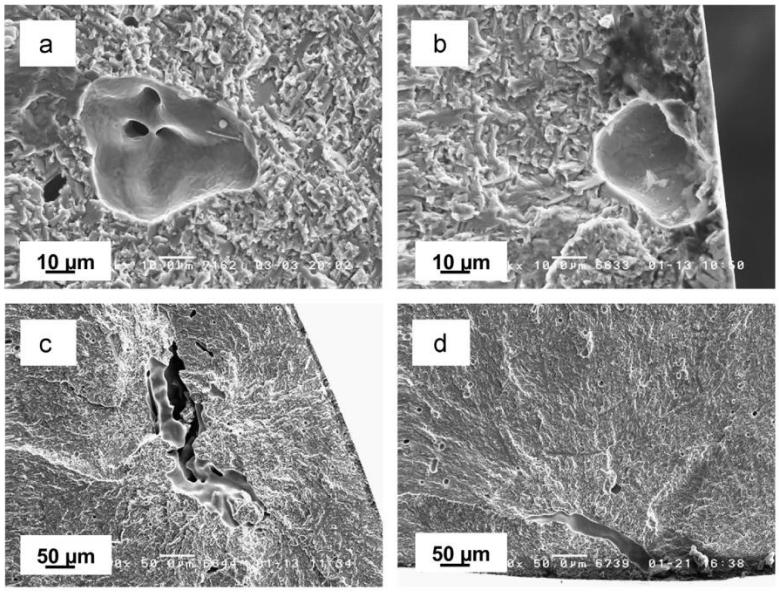

Fig. 4. Examples of fatigue crack initiations from pores (a) type-I internal pore (σ_{max}=460 MPa, N_f=1,988,166 cycles); (b) type-I surface pore (σ_{max}=700 MPa, N_f=42,076 cycles); (c) type-II internal pore, (σ_{max}=600 MPa, N_f=606,535 cycles); and (d) type-II surface pore (σ_{max}=550 MPa, N_f=36,604 cycles).

where

$$F_j = j \times 100/(n+1)$$

where j is the rank when arranged in ascending order of pore size, and n is the total number of observations. The cumulative rank is plotted against the equivalent pore diameter to illustrate the distribution of pore size in the present material, as shown in Fig. 3. The data in the figure supports the discrimination between two types of pores shown in Fig. 1. The plot reveals that the residual sinter pores (type-I pores with size range: 20–75 μm) and the cave pores (type-II pores with size range: 78–340 μm) each exhibit their own unique distribution. The transition between the two distributions occurs at a pore size of about 75 μm. Both types of pores were found to initiate fatigue cracks from the surface or the interior of the specimen at a range of applied stress levels. Typical crack initiating pores are shown in Fig. 4. Fig. 4(a) and (b) is a typical example of crack initiation from type-I sinter-pores. Fig. 4(c) and (d) is a typical example of crack initiation from type-II cave-pores.

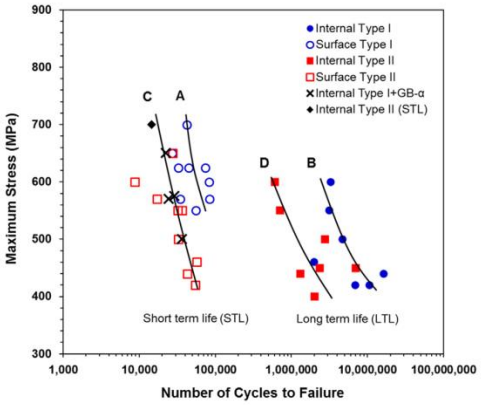

Fig. 5. S–N curve of PM Ti–6Al–4V alloy specimens distinctively grouped on the basis of initiating pore types and their location in the specimen.

3.2. S–N curves of PM Ti–6Al–4V by HSPT

Fig. 5 shows S–N fatigue data, plotted in the form of the maximum cyclic stress (σ_{max}) versus the number of cycles to failure (N_f) of all the samples tested. The data were identified and grouped according to the fatigue failure initiation modes. That is, distinct grouping of data in terms of fatigue crack initiation mechanisms, namely, surface versus interior crack initiation and/or whether the cracks initiated from a type-I or a type-II pore. It is to be noted that all pores that were located at a distance (the distance between specimen edge and the closest point on the pore surface) greater than the pore diameter were taken as interior pores. In fatigue of a defect-free material, a nucleation life is usually involved in the formation of a fatigue crack. In this work however, we find that the pores readily initiated cracks, therefore the fatigue life can be considered to be almost entirely made of crack propagation life [6,9,11]. Thus, there is no crystallographic or microstructural related crack initiation mechanism.

The data in Fig. 5 reveals that there are actually four distinct trends in the fatigue data. On the macroscopic level, the S–N curves separate naturally with two major parts: a short-term-life (STL) domain and a long-term-life (LTL) domain, reflecting the duality of the fatigue phenomenon [17,18]. However, within the STL and LTL domains, the data were found to order into two subgroups, depending on the pore type from which the crack initiated. The fatigue curves A and B in Fig. 5 are made of failures from type-I pores. On curve A, all the specimens failed from type-I pores that were located at the surface. On the other hand, failures from type-I pores that were located in the interior of the specimen formed the failure curve B.

The fatigue curves C and D in Fig. 5 are largely due to fatigue cracks initiating from type-II pores. Type-II pores that were located at the surface produced the shortest fatigue lives (curve C) and those that were located internally produced relatively longer fatigue lives (curve D). It is interesting to note that the cracking from type-I pores produced relatively longer fatigue lives, compared to those initiated from type-II pores. This is to be expected, because the size range of type-I pores was smaller than that of type-II pores.

It is therefore evident that short-term-life failures can be caused by both types of pores, located at or close to the specimen surfaces. There are two factors that are responsible for the relatively short fatigue lives. One is the geometrical effect, the geometry factor in Eq. (1) for surface pores is 30% higher than that for interior pores in Eq. (2). Secondly, the propagation of a surface crack is affected by the laboratory air environment leading to accelerated crack growth. Oguma et al. [26] have shown that the crack growth rate of Ti–6Al–4V in a room temperature air environment is significantly higher than that in vacuum. Hence, both the increased level of stress concentration and the exposure to the laboratory air environment reduces the fatigue life of these specimens relative to the internal pores.

There are however some exceptions to the classification above. In one fatigue specimen, failure started from an internal type-II pore, as indicated by a solid diamond symbol in Fig. 5. It was surprising to observe that an internal pore provided the shortest fatigue life, despite the fact that its crack initiation and growth was not influenced by the outside environment. Upon examination of the fracture surface, it was found that this initiating pore had an equivalent diameter of 274 μm and the applied stress in that fatigue test was the largest (700 MPa) of all tests performed, leading to the largest initial stress intensity factor. Though this was an internal pore, it appears that the crack initiation occurred readily because of the higher level of stress. This is thought to be the reason for this particular data point falling in curve C.

Another exception to the four distinct trends discussed above were the failures from large GB-α regions. Four samples marked with black X symbols in Fig. 5 were short-life fatigue failures, but failed from crack initiations from interior regions of the specimens. The fatigue fracture surfaces of these specimens indicated unusual fracture features, typically connected with fracturing of thick GB-α. As shown in Fig. 6, when cracks initiated from certain pores (regardless of Type-I or II), they tended to be located adjacent to a GB-α region. These cracks apparently propagated faster. The GB-α region provided a path for rapid propagation along the grain boundary, causing fracture steps and ligaments (indicated by arrows in Fig. 6) that are orientated in the projected direction of the GB-α. The combination of GB-α with the crack initiating pores, resulted in relatively shorter fatigue life. This is the primary reason for the internally-initiating cracks producing short-term fatigue lives.

The four trends in S–N data indicate a four-way competition for fatigue failure in the Ti–6Al–4V alloy manufactured by the PM route:

(i) surface-initiated failures with the shortest fatigue lives from type-II pores located at the surface. This also includes the exceptions: large type-II pore located internally (high stress level), as well as pores located in the proximity of GB-α in interior regions;
(ii) surface-initiated failures with relatively shorter (but not the shortest) fatigue lives, exclusively from type-I pores that statistically occurred at the surfaces of samples;
(iii) interior-initiated failures from type-II pores located internally in the specimen, producing relatively longer fatigue lives;
(iv) interior-initiated failures from type-I pores located in the bulk of the specimens, producing the longest fatigue lives.

3.3. Duality of S–N fatigue behavior

From the point of view of fatigue life, it is important to recognize that the principal difference between type-I and type-II pores is their size range. This can be seen in Fig. 5 where the internally located type-II pores (which are generally much larger than type-I pores) actually produced longer fatigue life than the type-I pores that happened to be located at the surface. It seems that environmental exposure (being located at the surface was more damaging than the size of the pore itself) had a dominant effect, overriding the effect of high stress concentration at a large pore. In order to evaluate this aspect, the crack initiation stress intensity factors were determined using Murakami's equations for stress intensity factors for 3-D cracks. The initial stress intensity factors, assuming that pores behave as cracks, were estimated according to the equations proposed by Murakami et al. [7]:

$$\Delta K_S = 0.65\Delta\sigma\sqrt{\pi D_e} \quad (1)$$

for a surface pore and

$$\Delta K_I = 0.5\Delta\sigma\sqrt{\pi D_e} \quad (2)$$

for an internal pore, respectively. Here, D_e is the equivalent pore diameter.

Fig. 7 shows the initial stress intensity factor values (ΔK_S, ΔK_I) versus the equivalent pore diameters for all the fatigue specimens tested in this study. The data are grouped into two categories: (i) short term fatigue life and (ii) long term fatigue life. It can be seen that all of the fatigue crack initiations that had a higher crack

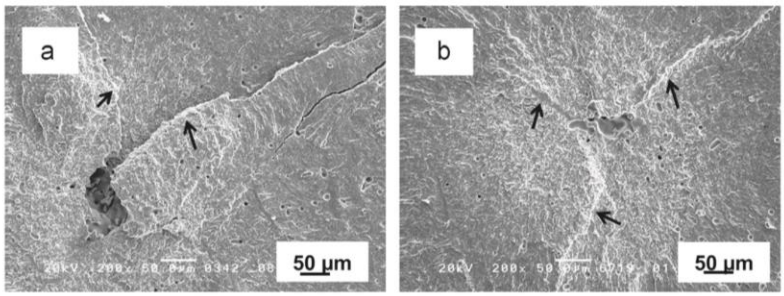

Fig. 6. Example of fatigue fracture surfaces of short term life specimens initiating from internal pores when they were associated with GB-α (a) σ_{max}=500 MPa, N_f=36,480 cycles; and (b) σ_{max}=650 MPa, N_f=22,615 cycles.

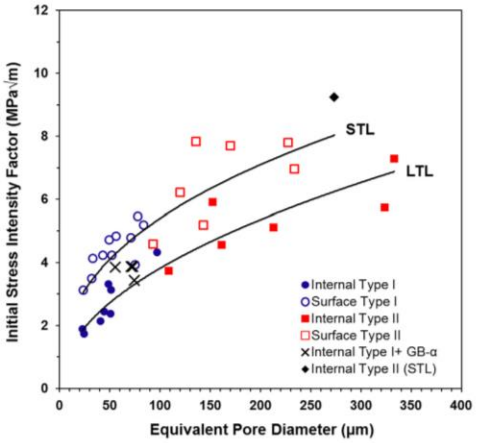

Fig. 7. Relationship between the initial stress intensity factor and equivalent initiating pore diameter.

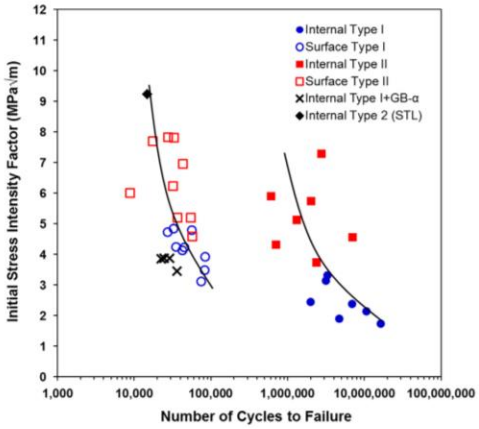

Fig. 8. Relationship between initial stress intensity factor and corresponding fatigue life.

initiation stress intensity factor had a short term life. The ones with the lower initial stress intensity factor (ΔK_S, ΔK_I) had relatively longer fatigue lives. Both types of pores, covering the entire initiation pore-size range of 20–340 μm, were involved in both life domains. Thus, it is clear from Fig. 7 that the competition between short-term life and the long-term life is also affected by the initial stress intensity factor levels, in addition to the location (surface versus interior) where they occur.

It is then possible that if the initial stress intensity factor and the location are factored into the analysis, the four distinct curves in Fig. 5 might condense into two distinct curves, one for short-term life and the other for the long-term life. This is affirmed in Fig. 8, where the S–N fatigue curve has been plotted in terms of the initial stress intensity factor for the specimens tested in this study. The two separate curves in Fig. 8 indeed confirm the duality of fatigue response. This figure indicates that when the pore size effects are accounted for, the dual fatigue behavior emerges in the data, one for environmentally affected short-life behavior and the long life behavior which is free from any environmental effect.

Fig. 8 reveals an apparent threshold initial stress intensity factor (about 3.2 MPa$\sqrt{m}$) for type-I specimens, which separates the STL and LTL domain clearly. The threshold initial stress intensity factor for failures from the type-II pores is not as clear as that of type-I. One reason might be that most of type-II pores have irregular shapes, making the estimated stress intensity factor deviate from the true stress intensity factor.

In Fig. 8 the X symbols are the specimens in which the crack initiations occurred from internal pores, but were found to be aided by GB-α. The crack propagating path (GB-α) can provide lower resistance to cleavage crack extension because of the absence of ductile beta phase in the path of the crack [27]. Fig. 8 also shows one specimen (diamond symbol) where the crack initiated from an internal pore and had the highest initial stress intensity factor. Both of these exceptions indicate that the location of failure initiation site is not the only factor that necessarily affects the fatigue life. This is supported by the observations of Lankford et al. [4]. In Lankford's study, the fatigue life was more closely related to the diameter of inclusions than to whether the nucleating particle was located at the surface or internal. Yokoyama et al. also found that the internal crack initiation site itself has nothing to do with the fatigue life [28], but the stress level and defect size are contributing factors. The influence of defect size may overtake the effect of both the crack propagation environment and the crack initiating location. This is consistent with the present study, because most of the fatigue life was essentially occupied by the crack propagation cycles to rupture. Which pore becomes the main crack initiator in a specimen is always a competitive process and depends on the size and the stress level. The results of this work confirm that the most dominant mechanism will be decided by the site with the greatest initial stress intensity factor, regardless of the location of the pore, or whether supplemented by environment effects or not.

4. Conclusions

The fatigue behavior of a powder metallurgy Ti–6Al–4V alloy made from titanium hydride powder by the HSPT process has been studied. The main results are summarized as follows:

1. Multiple crack initiations for small and large pores located either internally or at surfaces were shown to cause four distinct trends in fatigue failures. The four trends in S–N data indicate a four-way competition for fatigue failure in the present material.
2. The surface-initiated failures with the shortest fatigue lives were caused by type-II pores (larger cave-pores) located at surfaces, and large type-II pores located internally or from any pore located in the proximity of GB-α in interior regions. All these failures formed a unique S–N curve.
3. The surface-initiated failures with relatively shorter (not the shortest) fatigue lives, were caused exclusively by type-I pores (smaller sinter-pores) that statistically occurred at surfaces of samples. These specimens formed their own distinct S–N curve.
4. The interior-initiated failures from type-II pores located internally in the specimen, producing relatively longer fatigue lives, formed separate S–N curve.
5. The interior-initiated failures from type-I pores located in the bulk of the specimen, produced the longest fatigue lives. These failures formed separate S–N curve.
6. When the crack initiating pore size was accounted for in terms of initial stress intensity factor, a dual S–N fatigue response was resulted, supporting earlier observations in fatigue of structural materials.

Acknowledgment

The authors gratefully acknowledge the financial support from the U.S. Department of Energy, Innovative Manufacturing Initiative (DEEE0005761), through the Advanced Manufacturing Office and the Office of Energy Efficiency and Renewable Energy. The powders were supplied by Reading Alloys Inc. Robesonia, PA. We thank Pei Sun and James Paramore for their help in sample preparations, and Yan Wang for the X-ray microtomography scans.

References

[1] F.H. Froes, C. Suryanarayana, Rev. Part. Mater. 1 (1993) 223–275.
[2] M. Hagiwara, S. Emura, Mater. Sci. Eng. A 352 (2003) 85–92.
[3] J.Z. Yi, P.D. Lee, C. Lindley, T. Fukui, Mater. Sci. Eng. A 432 (2006) 59–68.
[4] J. Lankford, F.N. Kusenberger, Metall. Trans. 4 (1973) 553–559.
[5] Y. Yan, G. Liu, P. Nash, Int. J. Fatigue 55 (2013) 81–91.
[6] X. Zhu, J.Z. Yi, J.W. Jones, J.E. Allison, Metall. Mater. Trans. 38A (2007) 1111–1123.
[7] Y. Murakami, S. Kodama, S. Konuma, Int. J. Fatigue 11 (5) (1989) 291–298.
[8] A. De Bussac, Fatigue Fract. Eng. Mater. Struct. 17 (11) (1994) 1319–1325.
[9] Y. Jang, Y. Jeong, C. Yoon, S. Kim, Metall. Mater. Trans. 40A (2009) 1090–1099.
[10] P. Li, P.D. Lee, D.M. Maijer, T.C. Lindley, Acta Mater. 57 (2009) 3539–3548.
[11] J.Z. Yi, Y.X. Gao, P.D. Lee, H.M. Flower, T.C. Lindley, Metall. Mater. Trans. 34A (2003) 1879–1890.
[12] O.M. Ferri, T. Ebel, R. Bormann, Mater. Sci. Eng. A 527 (2010) 1800–1805.
[13] Z.Z. Fang, P. Sun, H. Wang, Adv. Eng. Mater. 14 (6) (2012) 383–387.
[14] P. Sun, Z.Z. Fang, M. Koopman, Adv. Eng. Mater. 15 (10) (2013) 1007–1013.
[15] P. Sun, Z.Z. Fang, M. Koopman, J. Paramor, K.S. Ravi Chandran, Y. Ren, J. Lu, Acta Mater. 84 (2015) 29–41.
[16] D.H. Kohn, P. Ducheyne, J. Mater. Sci. 26 (1991) 534–544.
[17] K.S. Ravi Chandran, Nat. Mater. 4 (2005) 303–308.
[18] K.S. Ravi Chandran, S.K. Jha, Acta Mater. 53 (2005) 1867–1881.
[19] S.K. Jha, K.S. Ravi Chandran, Scr. Mater. 48 (2003) 1207–1212.
[20] K.S. Ravi Chandran, P. Chang, G.T. Cashman, Int. J. Fatigue 32 (2010) 482–491.
[21] D.F. Neal, P.A. Blenkinsop, Acta Metall. 24 (1976) 59–63.
[22] A. Atrens, W. Hoffelner, T.W. Duerig, J.E. Allison, Scr. Metall. 17 (1983) 601–606.
[23] O. Umezaw, K. Nagai, ISIJ Int. 37 (12) (1997) 1170–1179.
[24] O. Umezawa, K. Nagai, K. Ishikawa, Mater. Sci. Eng. A 129 (1990) 217–221.
[25] S. Berett, Y. Murakami, Metall. Mater. Trans. 32B (2001) 517–523.
[26] H. Oguma, T. Nakamura, Int. J. Fatigue 50 (2013) 89–93.
[27] K.S. Ravichandran, E.S. Dwarakadasa, D. Banerjee, Scr. Metall. Mater. 25 (1991) 2115–2120.
[28] H. Yokoyama, O. Umezawa, K. Nagai, T. Suzuki, ISIJ Int. 37 (1997) 1237–1244.

CHAPTER 5

FATIGUE PROPERTY OF Ti-6AL-4V BY HYDROGEN SINTERING AND PHASE TRANSFORMTION

Published as:

F. Cao, K.S. Ravi Chandran, P. Kumar, P. Sun, Z.Z. Fang, and M. Koopman

New Powder Metallurgical Approach to Achieve High Fatigue Strength in Ti-6Al-4V Alloy

Metallurgical and Materials Transitions A, May 2016, volume 47, issue 5, pp 2335-2345.

New Powder Metallurgical Approach to Achieve High Fatigue Strength in Ti-6Al-4V Alloy

FEI CAO, K.S. RAVI CHANDRAN, PANKAJ KUMAR, PEI SUN, Z. ZAK FANG, and MARK KOOPMAN

Recently, manufacturing of titanium by sintering and dehydrogenation of hydride powders has generated a great deal of interest. An overarching concern regarding powder metallurgy (PM) titanium is that critical mechanical properties, especially the high-cycle fatigue strength, are lower than those of wrought titanium alloys. It is demonstrated here that PM Ti-6Al-4V alloy with mechanical properties comparable (in fatigue strength) and exceeding (in tensile properties) those of wrought Ti-6Al-4V can be produced from titanium hydride powder, through the hydrogen sintering and phase transformation process. Tensile and fatigue behavior, as well as fatigue fracture mechanisms, have been investigated under three processing conditions. It is shown that a reduction in the size of extreme-sized pores by changing the hydride particle size distribution can lead to improved fatigue strength. Further densification by pneumatic isostatic forging leads to a fatigue strength of ~550 MPa, comparable to the best of PM Ti-6Al-4V alloys prepared by other methods and approaching the fatigue strengths of wrought Ti-6Al-4V alloys. The microstructural factors that limit fatigue strength in PM titanium have been investigated, and pathways to achieve greater fatigue strengths in PM Ti-6Al-4V alloys have been identified.

DOI: 10.1007/s11661-016-3409-7

I. INTRODUCTION

TITANIUM powder metallurgy has been pursued for many years with the goal of reducing the cost of Ti manufacturing, and obtaining near-net-shape products with reduced fabrication steps.[1–4] Great emphasis was placed on PM manufacturing of titanium in the 1980 to 1990s, in order to successfully implement PM titanium components in aerospace applications. In these efforts, principally two approaches, the blended elemental (BE) powder approach and the pre-alloyed (PA) powder approach, have been undertaken to prepare PM titanium components. In the BE approach, titanium and other elemental component powders required to prepare an alloy of a specific composition are blended, compacted, and sintered at a sufficiently high temperature (usually in the β-phase field) to obtain the final alloy. In the PA approach, the powders of the required alloy composition are first prepared by atomization of the liquid alloy, followed by consolidation of powders by hot isostatic pressing (HIP). The PA products typically have superior mechanical properties to those of BE products due to higher density and uniformity of composition, resulting from the fully melted alloy. However, the costs of PA products are significantly higher, for reasons that are obvious from the steps of the method. Therefore, the BE method has been the generally preferred method to prepare PM titanium alloy parts at low cost.[5] However, the main drawback of the conventional BE PM method is the necessity to sinter in the β-phase field, which leads to a coarse colony microstructure with aligned α platelets, along with a thick layer of grain boundary α phase.[6–8] Both of these microstructural features are detrimental to HCF strength. Since titanium alloy parts are used in fatigue critical components, especially in aerospace and potentially in automotive applications, PM process innovations that target full densification without microstructure coarsening are necessary to improve the HCF strength of PM titanium alloys. Such improvements will allow PM titanium alloys to effectively compete with wrought titanium alloys.

The wrought Ti-6Al-4V alloy microstructures show fatigue strength levels (defined as the cyclic stress amplitude at which the sample survives for 10^7 cycles) ranging from about 400 MPa to about 700 MPa.[9] This range is generally due to the variations in processing and microstructures. Historically, the PM sintered Ti-6Al-4V alloys without any further processing have had fatigue strength levels below this range. In one of the earliest studies, Anderson *et al.*[2] used titanium sponge fines to fabricate a PM Ti-6Al-4V alloy. The alloy had a very low fatigue endurance limit (280 MPa). In a later work, Fujita *et al.*[1] employed sponge fines or titanium powders obtained by the hydride dehydride process as two different starting powder forms and sintered Ti-6Al-4V samples at 1533 K (1260 °C) under vacuum for 4 hours. The samples achieved densities >99

FEI CAO and PANKAJ KUMAR, Graduate Research Assistants, K.S. RAVI CHANDRAN and Z. ZAK FANG, Professors, PEI SUN, Postdoctoral Fellow, and MARK KOOPMAN, Research Professor, are with the Department of Metallurgical Engineering, University of Utah, Salt Lake City UT 84112. Contact e-mail: ravi.chandran@utah.edu

Manuscript submitted October 12, 2015.

pct. The fatigue endurance limit was approximately 370 MPa for the specimens prepared from the sponge fines. Because it is almost impossible to eliminate all the pores by sintering, HIP was used to close the residual pores in many studies. Hagiwara *et al.*[7] achieved an improved fatigue endurance limit (411 MPa) by applying HIP to the sintered BE compacts. The result supports the idea that reduction of porosity can lead to higher levels of fatigue strength.

Recently, a new PM process (HSPT) that involves sintering of TiH_2 powder in the β-phase field and obtaining the Ti-6Al-4V alloy by subsequent phase transformation and dehydrogenation has been introduced.[4,10–12] The advantage of the HSPT process is that a high density and a very fine microstructure, in the as-sintered state, can be achieved at moderate sintering temperatures. The raw TiH_2 powder is also less expensive than PA titanium powders produced by the pre-alloyed rotating electrode (PREP) process or the liquid alloy atomization process. According to the (Ti-6Al-4V)-H phase diagrams developed by different authors, β phase exists above about 1073 K (800 °C) in the Ti-6Al-4V-H system, at hydrogen concentrations >10 at. pct.[11,13–15] In the studies by Kerr and Qazi *et al.*,[13,15] provided that there is a sufficient amount of hydrogen in β solution, the β phase was hypothesized to transform into α and hydride phase upon cooling below this temperature. Since this transformation is eutectoid in nature, a very fine microstructure resulted. Sun *et al.* illustrated that the precipitation of α/α_2 phases within β grains during isothermal holding at temperatures below the β-transus under a hydrogen atmosphere, and the eutectoid transformation of remaining β into α and hydride phase at a lower temperature, is critical for the formation of the final fine $\alpha + \beta$ microstructure.[11,12] On this basis, in the HSPT process, the sintering of TiH_2 powder compacts is done in the β-phase field in hydrogen atmosphere and the subsequent phase transformation and dehydrogenation of the sintered Ti-6Al-4V-H alloy are performed below 1073 K (800 °C), to produce a very fine $\alpha + \beta$ Widmanstätten microstructure.[11,13,16]

The fatigue performance of the HSPT Ti-6Al-4V alloy with such a fine microstructure is therefore quite intriguing. The objective of this work is to demonstrate that PM Ti-6Al-4V alloys with high fatigue strength levels can be obtained using this HSPT process. In light of the previous attempts to enhance the fatigue strength levels of PM titanium materials, the principal question is how much improvement in fatigue performance occurs due to porosity reduction versus microstructure refinement. To explore this, the tensile and fatigue properties of HSPT Ti-6Al-4V fabricated from two different powder size distributions were investigated in this work. The mechanisms of fatigue crack initiation were investigated by fractography. It is demonstrated that fatigue strengths that can be achieved are higher than those obtainable *via* conventional PM methods. It is shown that the fatigue performance can be improved by reducing the porosity. Additionally, comparing the present microstructure with that from other BE PM approaches, it appears that the very fine microstructure also contributes to some extent to the improved fatigue strength. The complete closure of remaining pores by the PIF process resulted in even greater improvements in fatigue strength, to levels approaching those of wrought Ti-6Al-4V alloy.

II. EXPERIMENTAL PROCEDURES

The as-received TiH_2 powders (Reading Alloys, Ametek, Robesonia, PA) had a size range of $-20/+60$ mesh. Figure 1(a) illustrates the shapes of the as-received powders. The powders were milled for 30 minutes and then sieved to obtain -325 or -400 mesh powders. The sieved TiH_2 powders were mixed with -400 mesh 60Al/40V master alloy powder (sieved from the -325 mesh powder provided by Reading Alloys, Ametek, Robesonia, PA). The morphology of the powders after mixing with the master alloy powder is shown in Figure 1(b). The TiH_2 particles are generally angular in shape. The particle size distributions were determined by a laser diffraction-based particle size analyzer and are

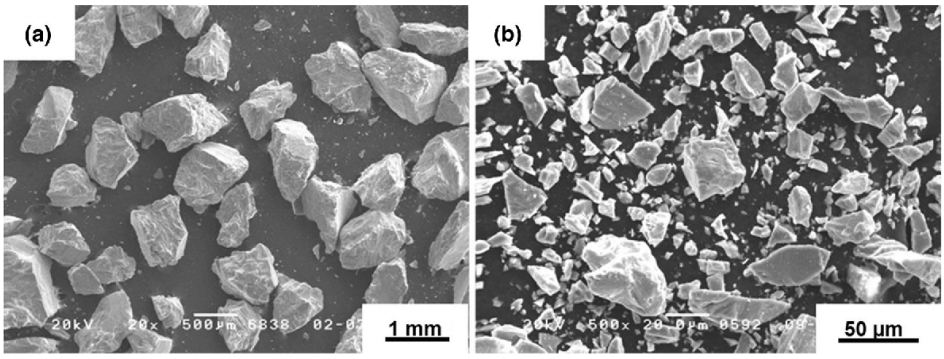

Fig. 1—Shape and size distribution of TiH_2 powder: (*a*) as-received $-20/+60$ mesh powder and (*b*) after blending the -325 mesh powder with the master alloy powder.

shown in Figure 2. The mean particle diameters for the −325 and −400 mesh powders were 25.3 and 20.6 μm, respectively.

Cylindrical Ti-6Al-4V bars were prepared by following the HSPT process. The details of the process are described elsewhere.[4,10] Briefly, the process involves first cold isostatic pressing (CIP) of the mixed TiH_2 and 60Al/40V master alloy powder at 350 MPa. After CIP, the green compacts were sintered at 1473 K (1200 °C) for 4 or 8 hours in a flowing atmosphere of Ar/H_2 (50/50) mixture. The sintered samples were then phase-transformed by furnace cooling to and holding at 923 K (650 °C) for 4 hours. This was followed by dehydrogenation at 1023 K (750 °C) for 12 hours to yield a Ti-6Al-4V alloy with fine $\alpha + \beta$ microstructure. Sintered bars were pneumatic isostatic forged (PIFed) at Ametek Inc. at 1123 K (850 °C) for a short time (5 to 10 minutes). The chemical composition of the sintered Ti-6Al-4V PM alloy was determined by ICP-MS analysis. The densities of the materials were determined using the Archimedes' principle. The size distribution of the pores was determined on metallographically polished sections, using ImageJ software, over 10 mm^2 areas. Microstructures were examined using an SEM equipped with an EBSD detector.

Tensile properties were determined using samples prepared according to the ASTM-E8 standard and tested at a strain rate of 0.002 S^{-1} at room temperature. Fatigue specimens having a total length of 76.2 mm were machined from sintered blanks. The test section was 6.35 mm in diameter and 12.7 mm in length. The test sections were polished using SiC paper until grade 1200, followed by finishing with 1 μm alumina suspension to obtain surfaces free from machining damage and residual stress. Tension tension fatigue tests were conducted under load control with a cyclic frequency of 35 Hz (sine wave), at a stress ratio ($\sigma_{min}/\sigma_{max}$) of 0.1, in a 100 kN MTS 810 testing system. The fatigue tests were conducted in laboratory air at room temperature. The wrought Ti-6Al-4V alloy specimens in mill-annealed condition were also tested in the same condition for fatigue performance comparison. Replicate tests were made until the stress-versus-fatigue-life trends were clearly revealed in the data. Fatigue fracture surfaces were examined in an SEM.

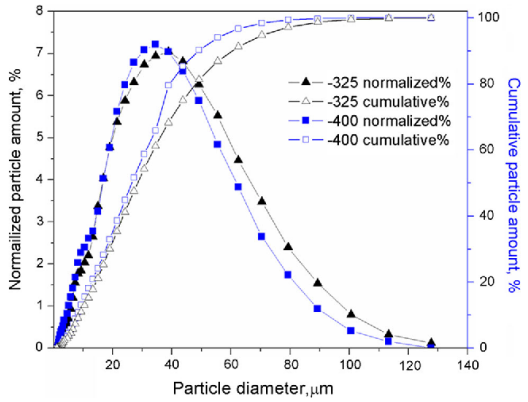

Fig. 2—Particle size distributions of mixed TiH_2 and 60Al/40V master alloy powder.

III. RESULTS AND DISCUSSION

A. *Materials and Microstructures*

Table I summarizes the alloy compositions obtained in the three processing conditions that were investigated in this work. The materials were prepared from −325 and −400 mesh TiH_2 powders. The choice of −325 and −400 mesh powders was made for two reasons. First, powder sizes coarser than 325 mesh resulted in densities <98 pct, and properties of such samples were deemed unlikely to be superior to those previously achieved. Secondly, any reduction of powder size less than 400 mesh, targeted to achieve improved densification during sintering, resulted in a large increase in oxygen level during the milling process, which severely reduced the tensile ductility of the sintered alloy. Hence, powder sizes coarser than −325 mesh and finer than −400 mesh were not pursued.

The compositions of Ti-6Al-4V alloys, shown in Table I, were generally within the composition range specified for a wrought Ti-6Al-4V alloy. The oxygen level, however, varied between 0.223 and 0.238 wt pct, which is slightly higher than that (0.2 wt pct) specified as a maximum for a wrought Ti-6Al-4V alloy. This difference is not expected to be significant in the context of the present work.

Microstructures of the Ti-6Al-4V alloys prepared in this work are shown in Figure 3. Figures 3(a) and (b) show optical and SEM micrographs of the alloy prepared from −325 mesh powders and sintered for 4 hours at 1473 K (1200 °C), hereafter referred to as −325 HSPT. Figures 3(c) and (d) show the microstructures of the alloy prepared from −400 mesh powders and sintered for 8 hours at 1473 K (1200 °C), hereafter referred to as −400 HSPT. Generally, the microstructures are very similar between the samples prepared from −325 mesh and −400 mesh powders. Figures 3(e) and (f) show the microstructure of the alloy after PIF of −400 HSPT samples. The prior-β grain size is essentially

Table I. Compositions of HSPT-Processed Ti-6Al-4V Alloys in Weight Percent

Specimen	Ti	Al	V	O	H	N
−325 HSPT/4 h	—	—	—	0.238	0.000237	0.0167
−400 HSPT/8 h	bal.	5.99	3.84	0.223	0.000276	0.0175
−400 HSPT/4 h + PIF	—	—	—	0.225	0.000448	0.0176

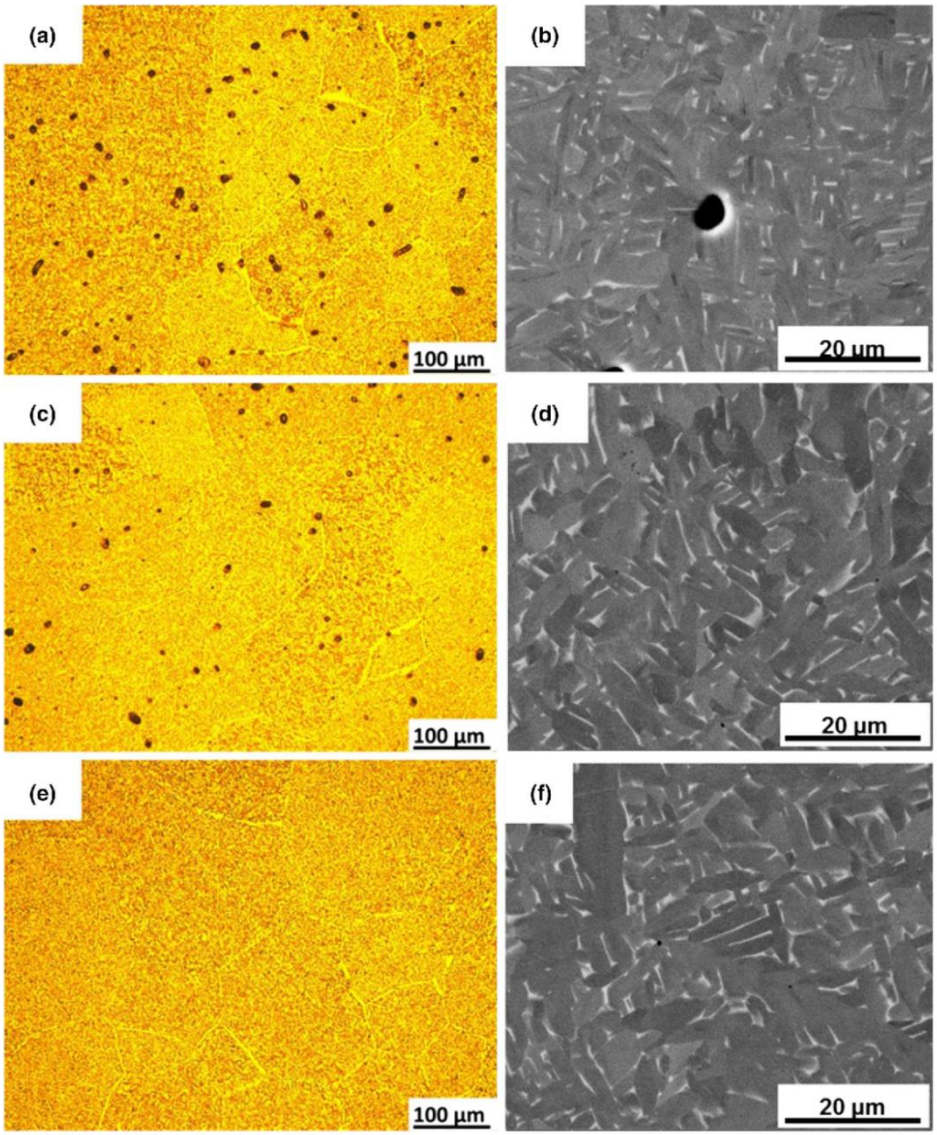

Fig. 3—Optical and SEM micrographs of Ti-6Al-4V alloys after sintering and dehydrogenation prepared with (*a*, *b*) −325 mesh powder (4 h), (*c*, *d*) −400 mesh powder (8 h), and (*e*, *f*) −400 mesh powder (4 h) followed by PIF consolidation.

equivalent to that in the as-sintered state (Figures 3(a) and (c)). However, the major change is that all the residual pores after sintering were closed by the PIF process. There were no obvious traces of the closed pores in the PIFed −400 HSPT samples.

Figure 4 shows the size distributions of the pores in the −325 HSPT and −400 HSPT samples by image analysis. Here, the pore size is characterized as the equivalent diameter of a circle that has the same area as that of an arbitrarily shaped pore in the polished section. Pores with an area smaller than 5 μm^2 were neglected by setting 5 μm^2 as the threshold during image processing in ImageJ. Such small pores were found not to affect the fatigue behavior unless they were inter-connected or present as clusters. The size distributions of pores showed that the differences in porosity between the −325 HSPT and the −400 HSPT samples came from two aspects. First is that, as seen in Figure 4, the amount of small pores is greatly reduced. Secondly, the largest pore size found over the examined area decreased

from 11.8 to 8.6 μm. This indicates that the porosity was decreased due to a decrease in the amount and size of pores. The average densities of −325 HSPT and −400 HSPT samples were determined to be 98.53 and 99.23 pct, respectively, using the Archimedes' principle. The porosity decreased by 0.7 pct using a finer starting powder (−400 mesh) and increasing the sintering time to 8 hours.

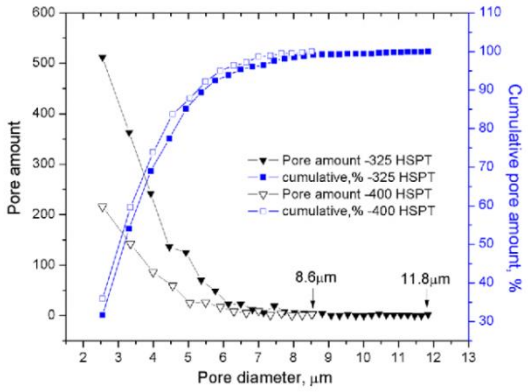

Fig. 4—Pore size distributions in −325 HSPT and −400 HSPT Ti-6Al-4V alloys.

The microstructural characteristics of HSPT-processed Ti-6Al-4V alloy include, most importantly, a fine $\alpha+\beta$ Widmanstätten microstructure , a relatively thin grain boundary α (GB-α) at prior-β grain boundaries, and some residual sintering pores. The orientation imaging microscopy (OIM) of the microstructure is shown in Figure 5. The orientation map indicates the lack of alignment of the α platelets, in contrast to the colony microstructure with parallel α plates, which typically results from vacuum sintering.[3,6] The average length and width of the α grains in the microstructure were 2 to 5 and ~10 μm, respectively. A coarse-α phase region is shown in Figure 5(c), which was observed in all the three alloys, this coarse-α phase can be a GB α plate or a large α grain adjacent to the prior-β grain boundary. The only microstructural difference between the as-HSPT-processed and HSPT+PIF-processed specimens is the porosity. Since the PIF procedure was

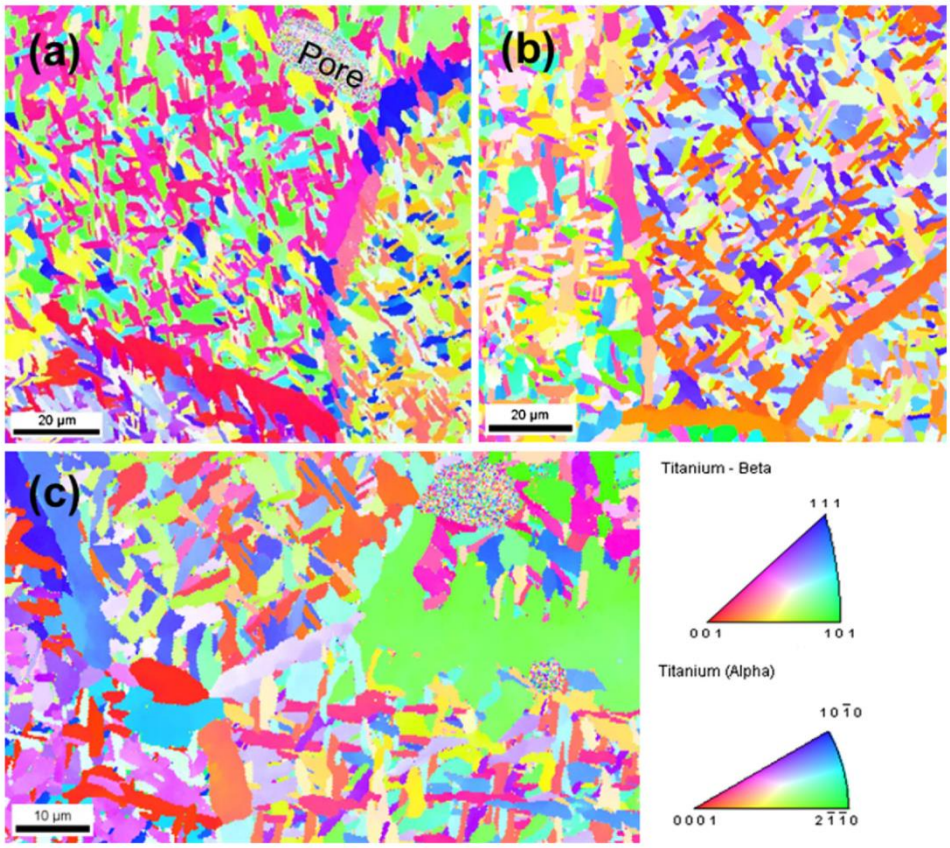

Fig. 5—Orientation imaging microscopies of Ti-6Al-4V alloys: (*a*) −400 HSPT, (*b*) −400 HSPT + PIF, (*c*) and −400 HSPT, which shows a coarse-α phase region (Color figure online).

done at 1123 K (850 °C), which is below the β transus of the Ti-6Al-4V alloy, in a short time, the microstructure did not exhibit any coarsening after the PIF treatment.

B. *Tensile Properties*

The stress strain curves for the materials investigated are shown in Figure 6. The average tensile properties are summarized in Table II. At comparable densities, the tensile and yield strengths of the present sintered samples are ~100 MPa higher than those found in the Ti-6Al-4V alloys prepared by other BE PM methods.[1,2,17] The tensile ductility is either comparable or higher than that obtained in other BE PM methods.[1,2,17] In the PIFed state, the tensile and yield strengths are also ~100 MPa higher than those of the hot-isostatic-pressed (HIPed) materials prepared by other BE approaches.[3,7,17] The elongation of the PIFed material here is about 18 pct which is higher than the elongations (12 to 16 pct) obtained in HIPed BE PM Ti-6Al-4V alloys.[3,7,18] Additionally, the yield and tensile strengths are also approximately 10 pct higher than those for annealed wrought Ti-6Al-4V alloys. The superior tensile properties, at least with respect to the wrought alloy, can be attributed to the fine $\alpha + \beta$ microstructure. Some of the increase in yield and tensile strength may come from the slightly higher oxygen content (0.23 wt pct) compared to that in wrought Ti-6Al-4V (0.2 wt pct) alloy. However, the average ductility for the −400 HSPT + PIF material is about the same as that for an annealed wrought Ti-6Al-4V alloy. This suggests that the effect of microstructure refinement on tensile properties far outweighs any degradation in ductility due to the slightly higher oxygen content.

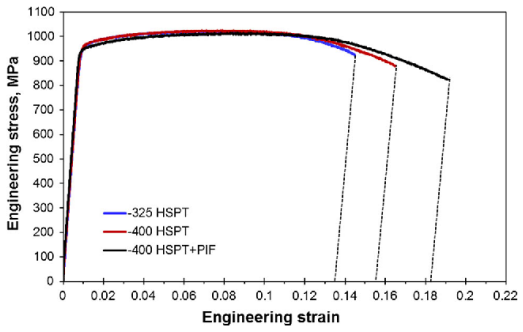

Fig. 6—Stress–strain curves of HSPT-processed Ti-6Al-4V alloys (Color figure online).

C. *Fatigue Performance*

Figure 7 shows the S-N fatigue data of the Ti-6Al-4V alloys prepared in this study. The fatigue data of wrought Ti-6Al-4V alloy are also included for the purpose of fatigue performance comparison. The HSPT-processed alloys have nearly the same microstructure (Figure 3), though their porosity levels are different. Since the data in Table II affirm that their tensile strengths are almost the same, any difference in their fatigue performance can be attributed only to the differences in porosity.

Fatigue strength here is defined as the maximum stress in the fatigue cycle for which the specimen survived for 10^7 cycles. The fatigue limit strength for the base alloy (−325 HSPT) is around 400 MPa (Figure 7) which is near the low end of the fatigue strength range found in wrought Ti-6Al-4V.[9] The −400 HSPT samples with less porosity showed a noticeable improvement in fatigue performance, with a fatigue limit of approximately 500 MPa. The improvement was more clearly evident when the data were examined at the stress levels between 500 and 550 MPa. At this stress range, the average fatigue life of −325 HSPT samples was of the order of 10^5 cycles, whereas it was between 10^6 and 10^7 for −400 HSPT samples. This improvement in fatigue performance can be attributed to the relative reduction in porosity, especially the largest pore size. The low-to-intermediate cycle fatigue performance of −400 HSPT + PIF samples was significantly higher than that of the −400 HSPT samples, which is comparable to that of wrought Ti-6Al-4V. This large improvement was mainly due to the elimination of porosity by

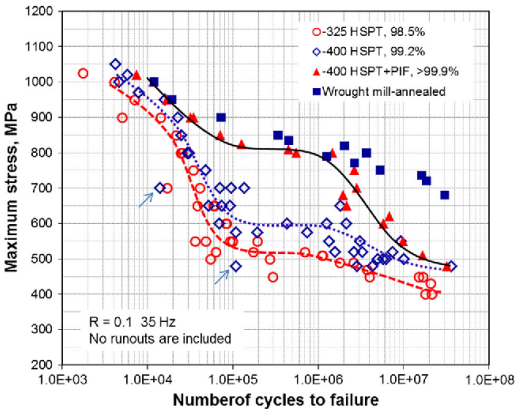

Fig. 7—S-N curves of −325 HSPT, −400 HSPT, −400 HSPT + PIF, and wrought mill-annealed Ti-6Al-4V alloys.

Table II. Tensile Properties of HSPT-Processed Ti-6Al-4V Alloys

Specimen	Sintering Time (h)	Density (pct)	YS (MPa)	UTS (MPa)	EL pct	RA pct
−325 HSPT(6)	4	98.53 (±0.04)	955 (±5)	1033 (±4)	13.7 (±0.2)	26.0 (±1.4)
−400 HSPT(6)	8	99.23 (±0.05)	946 (±6)	1032 (±3)	15.6 (±0.1)	31.6 (±1.8)
−400 HSPT + PIF(3)	4	>99.9	952 (±2)	1023 (±6)	18.2 (±0.1)	42.1 (±0.3)

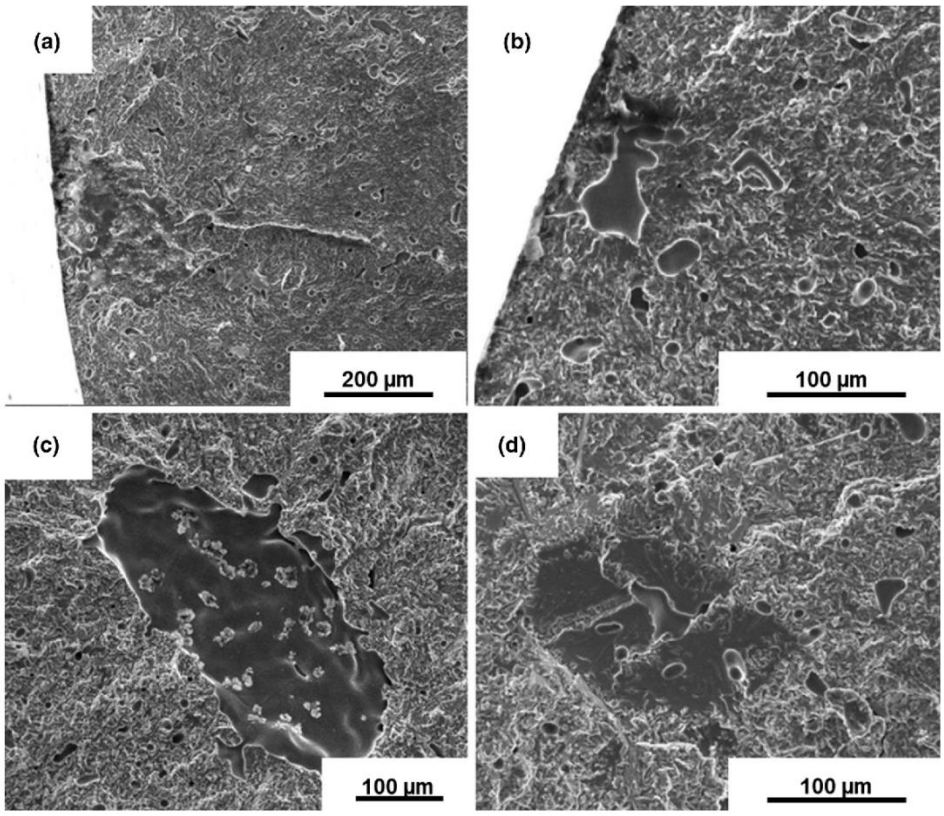

Fig. 8—Fractography of fatigue fractures of −325 HSPT samples. Fatigue cracks initiated from (*a*) extremely large pore on the surface (σ_{max} = 450 MPa, N_f = 72,666 cycles), (*b*) pore cluster near surface (σ_{max} = 520 MPa, N_f = 171,492 cycles), (*c*) extremely large pore under surface (σ_{max} = 400 MPa, N_f = 21,341,043 cycles), and (*d*) facet with pore cluster (σ_{max} = 450 MPa, N_f = 16,764,731 cycles).

PIF. However, the HCF performance is still inferior to that of wrought alloy, as shown in Figure 7, the S-N trend of the −400 HSPT + PIF samples declines with stress and approaches the fatigue lives of −400 HSPT samples. The PIF process appears to be ineffective in improving HCF life on the basis of the present S-N fatigue data. Nevertheless, an overall improvement in fatigue performance was achieved by PIF of the Ti-6Al-4V samples prepared with −400 mesh powders.

D. *Mechanisms of Fatigue Failure*

Fractography of the fatigue-fractured specimens in SEM showed that the equivalent diameter of the crack initiation sites ranged from approximately 20 to 300 μm. At high stress levels, fatigue cracks initiated from pores located at the specimen surface. At low stress levels, the fatigue crack typically initiated from a large internal microstructural discontinuity, a pore or a coarse-α phase region. It will be shown here that the relative fatigue performance of the three materials can be explained on the basis of the microstructure features that lead to fatigue crack initiation.

Typical fatigue crack initiation sites for −325 HSPT specimens at different stress levels are shown in Figure 8. Figures 8(a) and (b) show the crack initiation sites in the low-cycle fatigue region ($N_f < 5 \times 10^5$ cycles). Figure 8(a) is a statistically extreme case, where the initiation pore is quite large, about 200 μm in equivalent diameter. Specimens with such large crack initiation site consistently showed the shortest fatigue life, especially when the site was located on the surface. An example of the most common crack initiation site at high stress levels, in −325 HSPT specimens, is shown in Figure 8(b). This site is made of a cluster of small pores, each with sizes less than 100 μm. Figures 8(c) and (d) show the crack initiation sites in the high-cycle fatigue region. In this region, fatigue cracks started from either an internal pore (Figure 8(c)), or a facet originating from coarse-α phase region containing a cluster of small pores, as shown in Figure 8(d). It is thus clear that the fatigue failures transition from surface crack initiations to internal crack initiations as the cyclic stress is lowered. The flat region in the S-N curve between 10^5 and 10^6 cycles in Figure 7 corresponds to the transition from a surface-initiated to internally initiated fatigue failure mode.

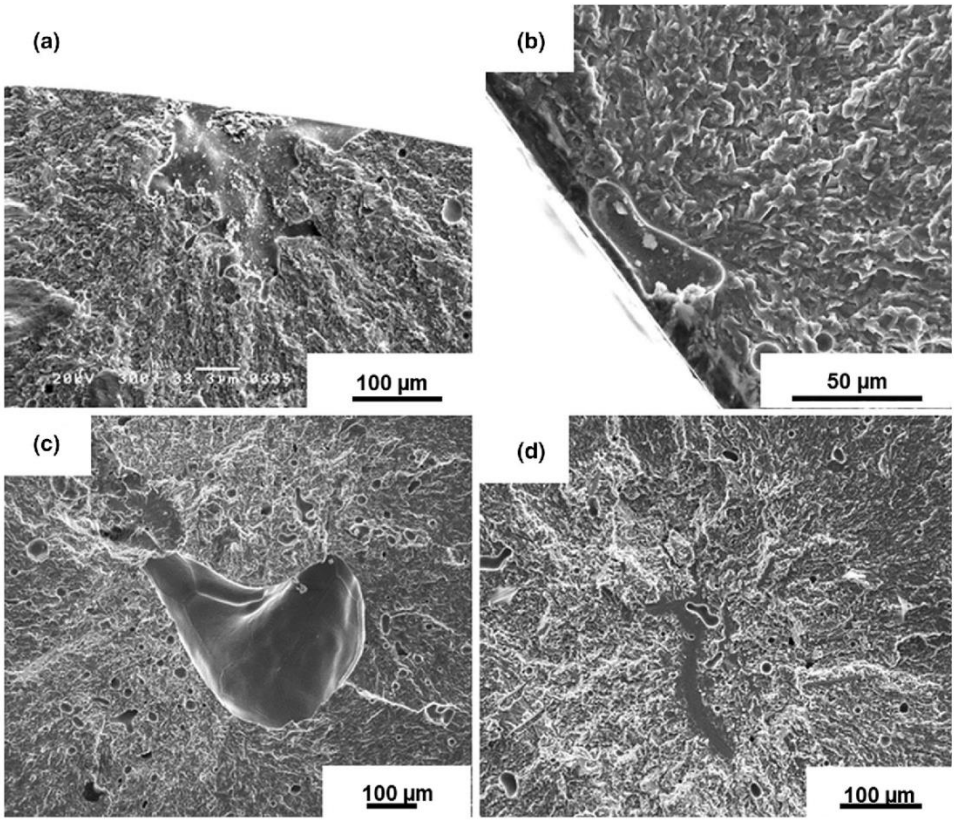

Fig. 9—Fractography of fatigue fractures of −400 HSPT samples. Fatigue cracks initiated from (*a*) extremely large pore on the surface (σ_{max} = 480 MPa, N_f = 109,423 cycles), (*b*) single small pore on the surface (σ_{max} = 600 MPa, N_f = 69,788 cycles), (*c*) large pore under surface (σ_{max} = 520 MPa, N_f = 7,469,674 cycles), and (*d*) facet under surface (σ_{max} = 550 MPa, N_f = 9,374,617 cycles).

Fractography of crack initiation sites in the −400 HSPT samples is shown in Figure 9. This sample also exhibited four different types of crack initiations depending on the fatigue stress level, that is, either from extreme-sized (>100 μm) pores on the surface (Figure 9(a)), or from small-sized pores on the surface (Figure 9(b)), or from internal pores (Figure 9(c)), or from coarse-α phase regions (Figure 9(d)). However, most initiations were from a relatively smaller single pore, which is in contrast to that observed in −325 HSPT specimens. In Figure 7, the two specimens, indicated by arrows, failed due to the extreme-sized pores on the specimen surface. With the exception of these two data points, the overall fatigue performance of −400 HSPT samples is much improved compared to that of −325 HSPT samples, due to a reduction in overall porosity and the elimination of pore clusters. The −400 HSPT samples also showed the transition from surface-initiated fatigue failures to internally initiated fatigue failures, between 10^5 and 10^6 cycles, similar to that observed in −325 HSPT samples.

Figure 10 shows the fractography of fatigue crack initiation sites for −400 HSPT + PIF specimens at different stress levels. Figure 10(a) is a typical crack initiation site at σ_{max} = 900 MPa neither pores nor inclusions were seen at the initiation site. They are similar to the crack initiation sites in high stress fatigue failures in wrought materials.[19] Figure 10(b) shows a crack initiation site near the surface, for σ_{max} = 700 MPa, which is made of a set of crystallographic facets. These crack initiation facets are thought to correspond to coarse-α phase regions (see in Figure 5(c)). In one sample, fatigue failure occurred from inclusions, as shown in Figure 10(c). The inclusion was determined to be a foreign particle containing calcium, carbon, and oxygen by EDS point analysis. Figure 10(d) shows a subsurface crack initiation site from facets. This situation is similar to the subsurface crack initiations in wrought Ti-6Al-4V alloys in the very high-cycle fatigue regime (>10^7 cycles).[19–21] Such initiation sites are usually composed of small facets, each with a size equivalent to that of α grains.[20,21] Regardless, the relatively larger fatigue crack initiation facet size, attributed to coarse-α phase regions in the HSPT specimens, reduces the fatigue life in HCF regime. Coarse-α phase region has longer slip length, which

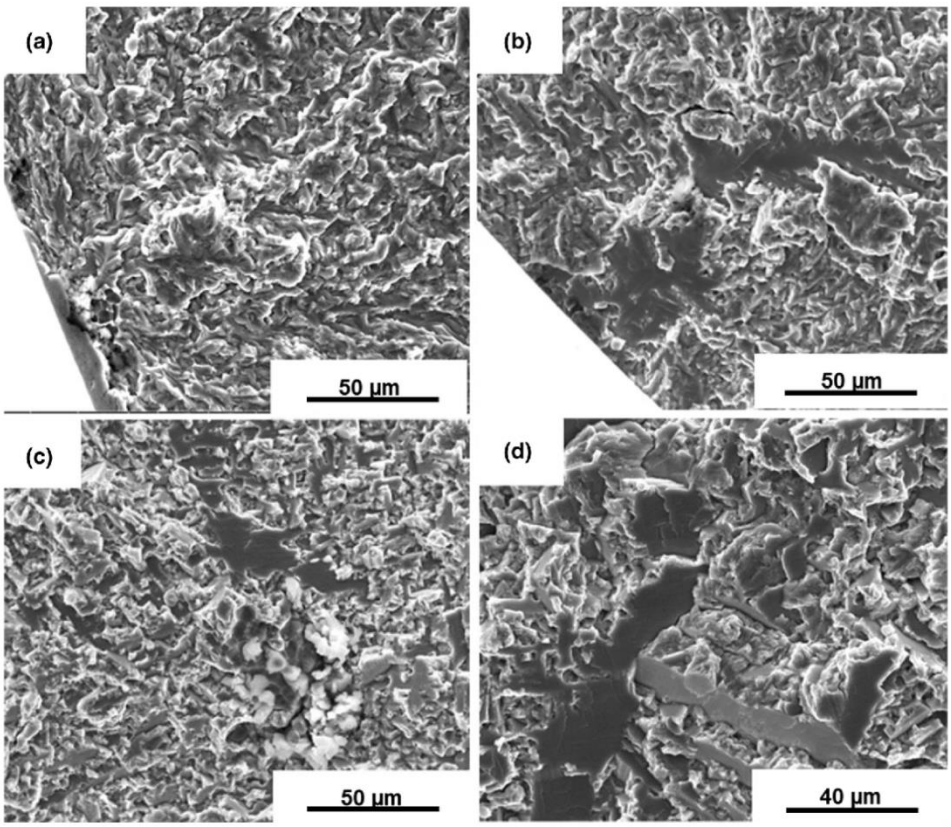

Fig. 10—Fractography of fatigue fractures of −400 HSPT + PIF samples. Fatigue cracks initiated from (*a*) featureless grain (σ_{max} = 900 MPa, N_f = 32,293 cycles), (*b*) facet just below the surface (σ_{max} = 700 MPa, N_f = 2,851,095 cycles), (*c*) inclusion together with facet (σ_{max} = 550 MPa, N_f 9,882,833 cycles), and (*d*) facet under surface (σ_{max} = 510 MPa, N_f = 16,945,546 cycles).

requires a relatively lower stress level to initiate a crack. Thus, the rapid decline of stress at HCF region in the −400 HSPT + PIF samples is due to the ease with which the crack can become critical at lower stress levels to reach the stable crack growth regime. [22]

It has been found that the role of the PIF processing is to change the crack initiator in fatigue. The only difference between the −400 HSPT specimens and the −400 HSPT + PIF specimens was the porosity, including the extreme-sized pores. The fatigue crack initiation site is determined by the competition between pores and extreme large α phase regions inside the test volume. In fatigue of PM materials, pores usually act as crack initiators and reduce the crack initiation life, and the number of cycles to failure is reduced, compared to pore-free materials.[23] The total fatigue life is substantively comprised by the crack propagation life, thus any differences in pore size from which the crack would initiate will lead to differences in fatigue life.[22,24] The −400 HSPT + PIF samples show much improved fatigue performance in the low-to-intermediate cycle fatigue region because of the elimination of pores. The HCF crack initiation sizes in −400 HSPT + PIF samples are sometimes comparable in size to the crack-initiating pores or coarse-α phase regions in the −400 HSPT samples. When the sizes of crack initiation sites (pores or coarse-α) are similar, the corresponding S-N fatigue lives are also similar, as shown by the overlapped data points in HCF region in Figure 7.

It can be summarized that in the present HSPT-processed PM Ti-6Al-4V alloys, extreme-sized pores or clusters of small pores with a large equivalent size, or coarse-α phase particles when large pores are absent, are the main fatigue crack initiators affecting fatigue life. It is also important to note that sizes of the crack-initiating pores or facets, found on the fracture surfaces, are much larger than the pores/grains typically found on the metallographically polished sections, because these are present in very small numbers. This suggests that fatigue life will be statistical, because the crack initiation and failure life are determined by the chance occurrence of any one of these features in the sample test volume. While a small area metallographic analysis area can hardly capture extreme-sized pores or coarse-α phase, a fatigue test will surely capture it by initiating a crack from it, as long as it is present in the test volume. This

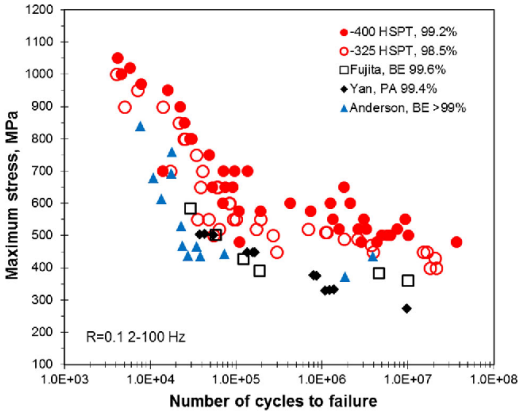

Fig. 11—Comparison of Fatigue performance of Ti-6Al-4V PM alloys prepared by HSPT with the fatigue performance of samples prepared by other PM processes with similar as-sintered density.[1, 2, 17]

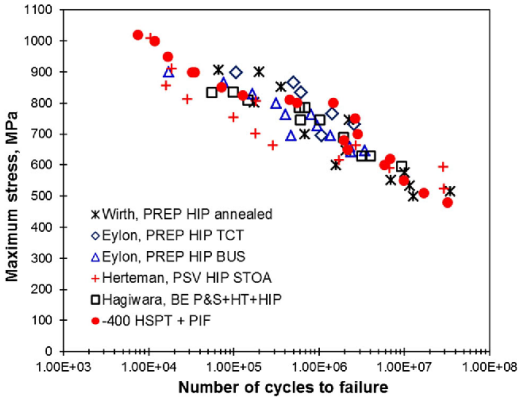

Fig. 12—Comparison of fatigue performance of Ti-6Al-4V alloy prepared by −400 HSPT + PIF process with the fatigue performance of samples prepared by HIP + heat treatment.[3,6,7,25–27] (TCT, thermochemical treated; BUS, broken-up structure; STOA, solution treated and overaged; P&S, pressed and sintered; HT, heat treated.).

perhaps points to the importance of elimination of extreme-sized pores and α phase regions, in powder metallurgy materials, to obtain a consistent improvement in fatigue performance.

E. *Comparison of Fatigue Performance of HSPT Ti-6Al-4V Alloys Against Other PM Ti-6Al-4V Alloys*

To put the present study in perspective, S-N fatigue data of PM Ti-6Al-4V alloys from other studies are compared with the present S-N data in Figure 11. The figure shows that the endurance limit stress value (defined at 10^7 cycles) of −400 HSPT samples is about 150 MPa higher than that of other PM-processed materials (the comparison is made at similar sintered density), which have coarse lamellar α colonies in the microstructure.[1,2,17] This demonstrates the significant advantage of the HSPT process in terms of providing high fatigue strength for the PM Ti-6Al-4V alloy, relative to other PM processes. This improvement can be primarily attributed to the finer $\alpha + \beta$ microstructure resulting from eutectoid phase transformation step in the HSPT process. The hydrogen that was present as hydride in the starting powder facilitated the formation of a finer eutectoid microstructure, when cooled through the β to α + hydride transition temperature, which then led to a finer $\alpha + \beta$ microstructure upon dehydrogenation. Despite the presence of extreme-sized pores in the −400 HSPT samples, they showed a fatigue limit of about 500 MPa, which is very encouraging from the point of view of the potential of the HSPT process for preparing fatigue-resistant titanium components. The fatigue endurance limit can be further improved by eliminating the extreme size pores in this material. This can very likely be achieved with further optimization of TiH_2 powder particle size distribution and HSPT sintering conditions.

Figure 12 shows a comparison of fatigue performance of −400 HSPT + PIF Ti-6Al-4V alloy samples with the results of other works[3,6,7,25–27] that used HIP and additional heat treatment processes. In general, the HIP and heat treatment steps serve to eliminate porosity and to alter the size, shape, and distribution of α and β phases in the microstructure, thus improving significantly the fatigue performance. It can be seen that the S-N fatigue performance of the present Ti-6Al-4V alloy in the −400 HSPT + PIF condition is quite comparable to the S-N data from other processes, which employed more expensive powders and/or more complicated processing steps. This suggests that the fatigue performance of the materials prepared by the present powder metallurgical approach is at least as good as the best PM Ti-6Al-4V alloys that have been processed through HIP and heat treatment steps. Because the present process uses TiH_2 powder as the raw material, the cost of the present process can be considerably lower than other processes to manufacture PM titanium alloys.

IV. CONCLUSIONS

1. The hydrogen sintering and phase transformation (HSPT) process produces a high-density Ti-6Al-4V alloy with excellent strength, ductility, and good fatigue resistance.
2. The use of −400 mesh TiH_2 powder in sintering resulted in a significant improvement in fatigue performance, relative to −325 mesh powder, due to the increased sintering density and the elimination of pore clusters.
3. When compared at similar density levels, the fine $\alpha+\beta$ microstructure, resulting from the present HSPT process, leads to a significantly improved tensile strength and fatigue performance, relative to the standard powder metallurgical approaches that use blended elements.
4. Fatigue strength in the as-sintered condition is greatly affected by the extreme-sized pores or clusters of pores present in the microstructure,

with the average-sized individual pores generally not participating in any fatigue crack initiation process.

5. Pneumatic isostatic forging (PIF) after sintering closed the residual pores without coarsening the microstructure, which leads to a large increase in fatigue performance. The fatigue performance of HSPT + PIF-processed materials is equivalent to the best fatigue results found in other PM Ti-6Al-4V alloys which were consolidated by HIP followed by additional heat treatment steps.
6. The fatigue crack initiation mechanism in the HSPT-processed Ti-6Al-4V alloy is a competition between the extreme-sized pores and α phase regions. Further improvements in processing with a view to eliminate the extreme-sized crack initiators should lead to even greater improvements in fatigue life of the PM Ti-6Al-4V alloy.

ACKNOWLEDGMENTS

The authors gratefully acknowledge the funding support from the US Department of Energy, Innovative Manufacturing Initiative (DEEE0005761), through the Advanced Manufacturing Office and the Office of Energy Efficiency and Renewable Energy.

REFERENCES

1. T. Fujita, A. Ogawa, C. Ouchi, and H. Tajima: *Mater. Sci. Eng. A*, 1996, vol. 213, pp. 148–53.
2. P.J. Anderson, V.M. Svoyatytsky, F.H. Froes, Y. Mahajan, and D. Eylon: *Modern Develop. Powder Metall.*, 1981, vol. 13, pp. 537–49.
3. D. Eylon, R.G. Vogt, and F.H. Froes: *Modern Develop. Powder Metall.*, 1985, vol. 16, pp. 563–75.
4. Z.Z. Fang, P. Sun, and H. Wang: *Adv. Eng. Mater.*, 2012, vol. 14 (6), pp. 383–87.
5. Z.Z. Fang and P. Sun: *Key Eng. Mater.*, 2012, vol. 520, pp. 15–23.
6. M. Hagiwara and S. Emura: *Mater. Sci. Eng. A*, 2003, vol. 352, pp. 85–92.
7. M. Hagiwara, Y. Kaieda, Y. Kawabe, and S. Miura: *ISIJ Int.*, 1991, vol. 31, pp. 922–90.
8. D. Eylon: *Metall. Trans. A*, 1979, vol. 10A, pp. 311–17.
9. F.H. Froes, S.J. Mashl, V.S. Moxson, J.C. Hebeisen, and V.A. Duz: *JOM*, 2004, vol. 56 (11), pp. 46–48.
10. P. Sun, Z.Z. Fang, and M. Koopman: *Adv. Eng. Mater.*, 2013, vol. 15 (10), pp. 1007–13.
11. P. Sun, Z.Z. Fang, M. Koopman, J. Paramore, K.S. Ravi Chandran, Y. Ren, and J. Lu: *Acta Mater.*, 2015, vol. 84, pp. 29–41.
12. P. Sun, Z.Z. Fang, M. Koopman, Y. Xia, J. Paramore, K.S. Ravi Chandran, Y. Ren, and J. Lu: *Metall. Mater. Trans. A*, 2015, vol. 46A, pp. 1–15.
13. W.R. Kerr, P.R. Smith, M.E. Rosenblum, F.J. Gurney, Y.R. Mahajan, and L.R. Bidwell: *Titanium'80, Science and Technology, Proceedings of the 4th International Conference on Titanium.*, Metall. Soc. of AIME, Kyoto, Japan, 1980, pp. 2477–86.
14. W.R. Kerr: *Metall. Mater. Trans. A*, 1985, vol. 16A, pp. 1077–87.
15. J. Qazi, J. Rahim, F. Froes, O. Senkov, and A. Genc: *Metall. Mater. Trans. A*, 2001, vol. 32A, pp. 2453–63.
16. D.H. Kohn and P. Ducheyne: *J. Mater. Sci.*, 1991, vol. 26, pp. 534–44.
17. Y. Yan, G.L. Nash, and P. Nash: *Int. J. Fatigue*, 2013, vol. 55, pp. 81–91.
18. V.S. Moxson, P. Sjoblom, and M.J. Trzcinski: *Adv. Powder Metall.*, 1992, vol. 6, pp. 125–40.
19. A. Atrens, W. Hoffelner, T.W. Duerig, and J.E. Allison: *Scripta Metall.*, 1983, vol. 17, pp. 601–06.
20. Y. Furuya and E. Takeuchi: *Mater. Sci. Eng. A*, 2014, vol. 598, pp. 135–40.
21. X. Liu, C. Sun, and Y. Hong: *Mater. Sci. Eng. A*, 2015, vol. 622, pp. 228–35.
22. K.J. Miller: *Mater. Sci. Tech.*, 1993, vol. 9, pp. 453–62.
23. A. De Bussac: *Fatigue Fract. Eng. Mater. Struct.*, 1994, vol. 17, pp. 1319–25.
24. F. Cao, P. Kumar, M. Koopman, C. Lin, Z.Z. Fang, and K.S. Ravi Chandran: *Mater. Sci. Eng. A*, 2015, vol. 630, pp. 139–45.
25. J.P. Herteman, D. Eylon, and F.H. Froes: *Powder Metall. Int.*, 1985, vol. 17, pp. 116–19.
26. F.H. Froes, D. Eylon, and S.W. Schwenker: *Progress Powder Metall.*, 1986, vol. 41, pp. 519–30.
27. G. Wirth, K.J. Grundhoff, and W. Smarsly: *S.A.M.P.E Q.*, 1986, vol. 17, pp. 34–39.

CHAPTER 6

CRACK GROWTH

6.1 Introduction

Titanium alloys are extensively used in aerospace applications. Fatigue crack growth properties of titanium alloys, including near threshold and Paris regions, are of great importance for the fatigue life assessment of service components, inspections, and repair schemes. Damage tolerance design including fracture toughness and fatigue crack growth has been proposed by aviation industry designers in addition to conventional fatigue/strength-based criteria in the component-safety design and material selection. The predominant influencing factors on fatigue crack growth behavior may be divided into extrinsic parameters, such as loading conditions, stress ration and loading waveform, and environment, and intrinsic parameters such as alloy composition (interstitial element) and microstructure. Microstructural feature plays an important role in the near threshold crack growth region, where a microstructurally small crack interacts with microstructure. The HSPT Ti-6Al-4V alloy with a very fine Widmanstätten/grain boundary microstructure was considered to have great damage-tolerance properties. At present, most fatigue crack growth research of titanium is focused on wrought Ti-6Al-4V alloys. Limited data about the fatigue crack growth behavior of PM titanium alloys have been reported.

Therefore, in the present investigation, a comparative study was undertaken to characterize the crack growth behavior of HSPT processed Ti-6Al-4V alloys in the as-sintered state and as-PIFed state, in comparison with that of wrought Ti-6Al-4V alloy. SEM was used to observe fractured surfaces of the crack growth features at different SIF ranges.

In order to make sure the specimen is consistent with the fatigue and tension specimens, the blanks with same dimensions were made for crack growth specimens. As limited by the size of PM Ti-6Al-4V alloy blanks, miniature single edge-notched tension specimens were used to perform crack growth tests. The experimental set-up and procedures were introduced in Chapter 3.

6.2 K Solution for the Present Miniature Specimen

Fatigue crack growth experiments with miniature specimens are of interest with respect to the characterization of small volume materials. Miniature specimens are used to evaluate biomaterials,[1] and the variability of properties in small components.[2] Because of the size limitation, it is often not possible to strictly adhere to ASTM standard specimens. An open question is whether these ΔK solutions will properly correlate the fatigue crack growth rates in miniature specimens. Indiscriminate use of ΔK solutions can lead to erroneous fatigue crack growth data.

Figure 6.1 illustrates the fatigue crack growth data of the Ti-6Al-4V alloy correlated on the basis on the uniform-stress K solution, equation (6.1), from the compilation of stress intensity factors by Tada et al.[3] This K solution has been used extensively in books and publications.[4,5] It is quite surprising that the fatigue crack

growth rates are indeed dependent on the remote stress amplitude level. The data seem to be stacked in layers, with higher applied stress levels producing higher crack growth rates, when compared at a given ΔK level of crack propagation. The crack growth rates of tests at stress amplitudes systematically increased with the applied stress amplitude. The variance in growth rates is about a factor of ten at about 40 MPa√m. The crack growth rates of tests at stress amplitudes 230-500 MPa nearly agreed with each other, indicating that the ΔK-correlation based on uniform-stressed ends works well at these stress amplitudes. Such a variance has also been seen in other investigations.[6,7]

$$K = \sigma\sqrt{\pi a}\left[1.12 - 0.23\left(\frac{a}{w}\right) + 10.55\left(\frac{a}{w}\right)^2 - 21.72\left(\frac{a}{w}\right)^3 + 30.39\left(\frac{a}{w}\right)^4\right] \qquad (6.1)$$

Table 6.1 summarizes the crack length at which tests were terminated and the corresponding ΔK values and the sizes of the plane strain plastic zones. The tests were terminated at these points and specimens were monotonically pulled apart to determine whether the fatigue crack growth conformed to plane strain conditions. The plastic zone sizes were calculated using Irwin's equation:

$$r = \frac{1}{3\pi} \cdot \left(\frac{\Delta K}{\sigma_{ys}}\right)^2 \qquad (6.2)$$

For the tests with σ_{max} values of 70-360 MPa, the plastic zones sizes at the test termination were at most one-tenth of the specimen thickness, or even less over the lengths of crack growth measured. This is consistent with the flat fracture surfaces with negligible shear lips in specimens tested at these stresses (Figure 6.2). Even at the stress

amplitude of 500 MPa, the plastic zone size was only about one-fourth of the specimen thickness and the crack seemed to grow largely under plane strain conditions. At this stage, the crack in this specimen seems to be at the end of stage-II crack growth. It seems that there is no effect of plane-stress surface regions on the fatigue crack growth at this stress amplitude.

It is shown that the finite-width correction factor for uniform stress state K solution increases rapidly with the increase of crack length (a), as shown in Figure 6.3 by empty circle symbols, which is the K solution for SENT specimens used by different authors.[4,5] A possible cause of the crack growth data scatter is the freedom of rotation of the ends of the specimen, which is mathematically present in this type of solution. To eliminate this problem, a K solution for uniformly displaced ends, for the present miniature specimen (H/W = 3), was generated by 2D boundary element method. This solution is given by:

$$K = \sigma\sqrt{\pi a}\left[1.11 + 0.664\left(\frac{a}{w}\right) - 3.52\left(\frac{a}{w}\right)^2 + 19.92\left(\frac{a}{w}\right)^3 - 33.26\left(\frac{a}{w}\right)^4 + 19.32\left(\frac{a}{w}\right)^5\right] \quad (6.2)$$

Where a is the crack length, and w is the width of the SENT specimen. Figure 6.4 illustrates the fatigue crack growth data correlated using the ΔK values (ΔK_d) calculated using equation (6.2). An excellent correlation of fatigue crack growth data at all stress levels is seen.

6.3 Crack Growth Behavior of HSPT Ti-6Al-4V Alloys

The da/dN-ΔK curve of HSPT + PIFed Ti-6Al-4V alloy is shown in Figure 6.5. The crack growth SIF range threshold (ΔK_{th}) is approximately 3.2 MPa√m, which is lower than the value of wrought Ti-6Al-4V with bimodal (~4.0 MPa√m)[8,9] and relative coarse lamella (~5.5 MPa√m)[10] microstructures. It has been shown that finer grain size will lead to lower threshold value.[11] The lower threshold value obtained for HSPT processed Ti-6Al-4V alloy is because of the finer grains. It is shown in Figure 6.6 that the crack growth curves of all three materials almost overlapped. This indicates that the micro-sized pores in the as-HSPT processed materials do not actually affect the crack growth behavior. It is also not surprising that the threshold (~3.0 MPa√m) and crack growth behavior of wrought Ti-6Al-4V alloy also overlaps with that of HSPT alloys, because the diameter of α grain in annealed wrought Ti-6Al-4V is similar to the length of Widmanstätten α grains.

The fractographs at different ΔK were observed in a SEM. Figure 6.7 shows the fractured area at the near threshold region (ΔK = 3.7 MPa√m), where facets prevails. Crack growth rate oscillating was seen up to the SIF range of 8 MPa√m. Figure 6.8 shows a much darker region with relatively flattened region at ΔK = 8.6 MPa√m; some rounded granular is seen in this region. Figures 6.9 and 6.10 show striations at stable crack growth region at ΔK = 12.8 and 14.5 MPa√m, respectively. The mechanism of crack growth and their corresponding features at different stages will be discussed in Chapter 7 together with those of fatigue failed specimens.

Table 6.1 Sizes of Plastic Zones at the End of Tests

Max. Stress (MPa)	Crack Length (mm)	ΔK, end of test (MPa√m)	Plastic Zone Size (μm)
70	7.99	43.0	217
100	7.26	45.6	245
230	5.05	49.7	291
360	2.48	36.4	156
500	3.30	67.7	539

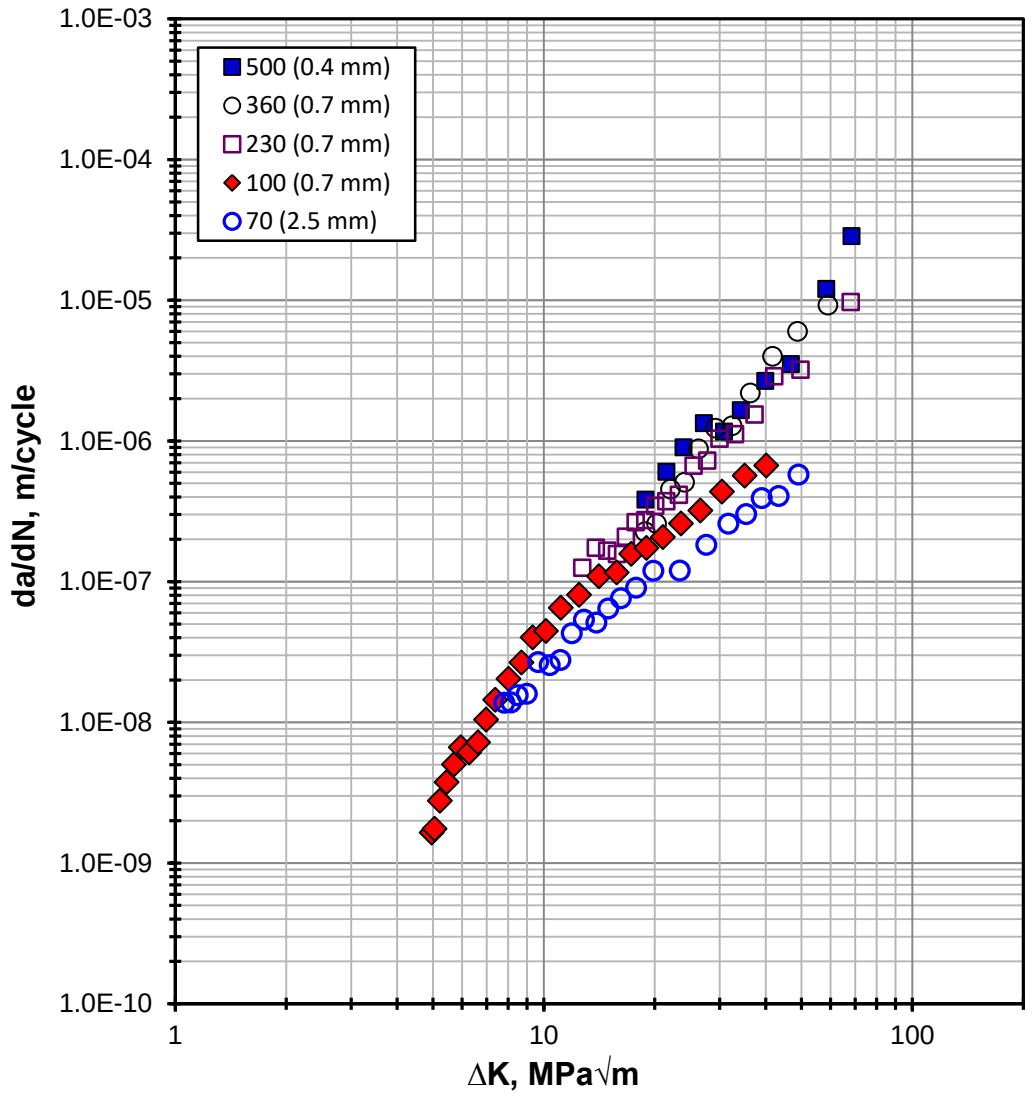

Figure 6.1 Fatigue crack growth rates of PIFed Ti-6Al-4V alloy as a function of ΔK (uniform stress) for various stress amplitudes. The numbers in parentheses indicate pre-crack depths.

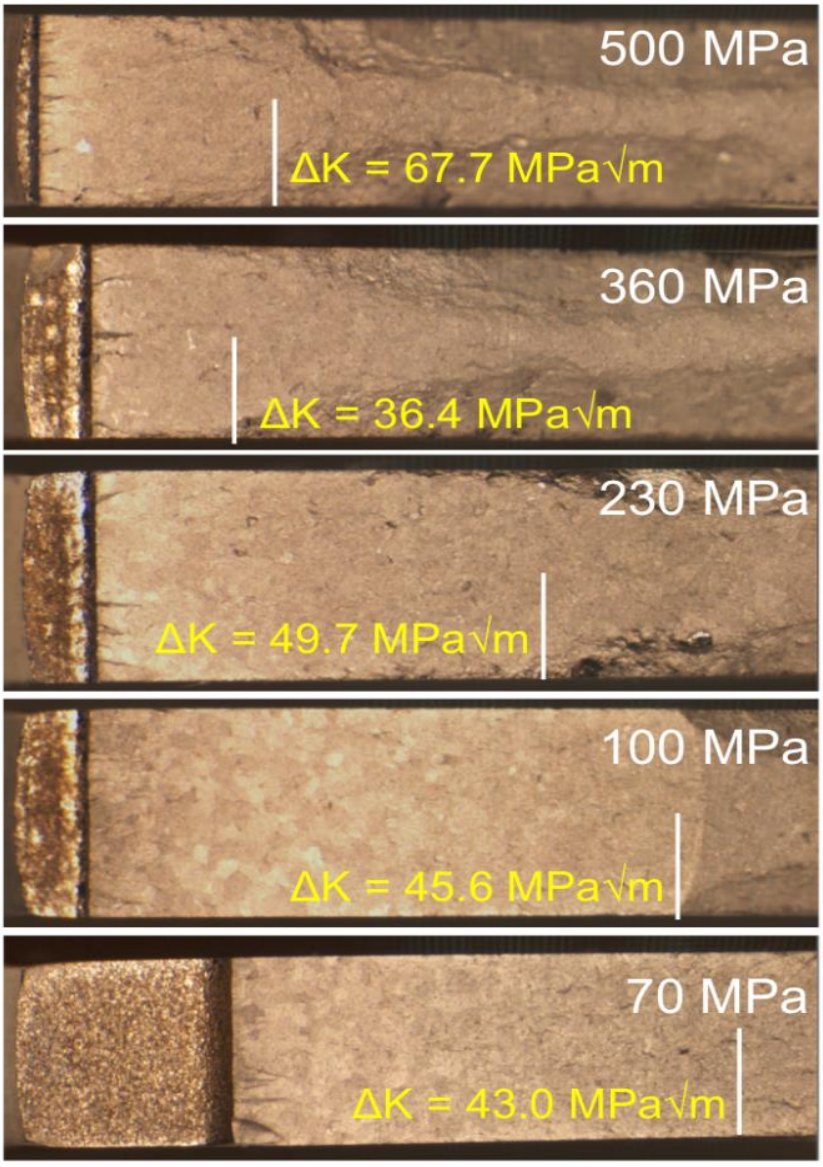

Figure 6.2 Fracture surfaces of SENT tested at different stress levels. Reprinted from K.S. Ravi Chandran, F. Cao, and J.C. Newman Jr., Scripta Mater. 122 (2016) 18-21[12] with permission from Elsevier.

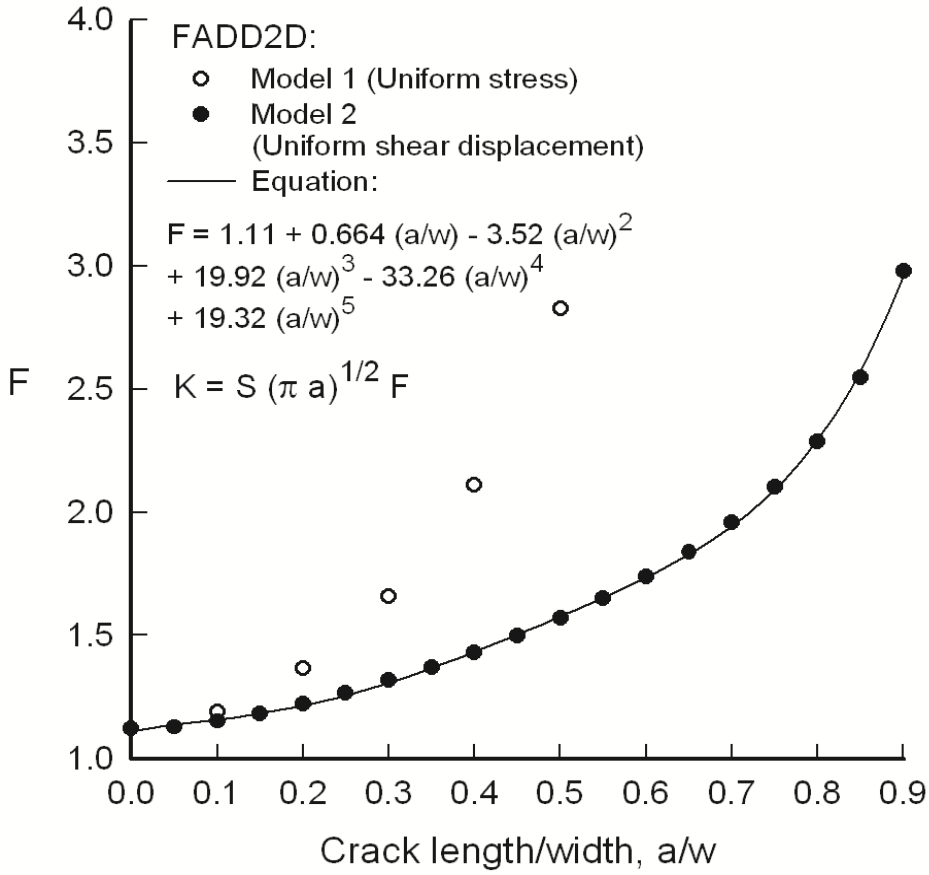

Figure 6.3 Finite-width correction factors for uniform stress and uniform shear displacement conditions.

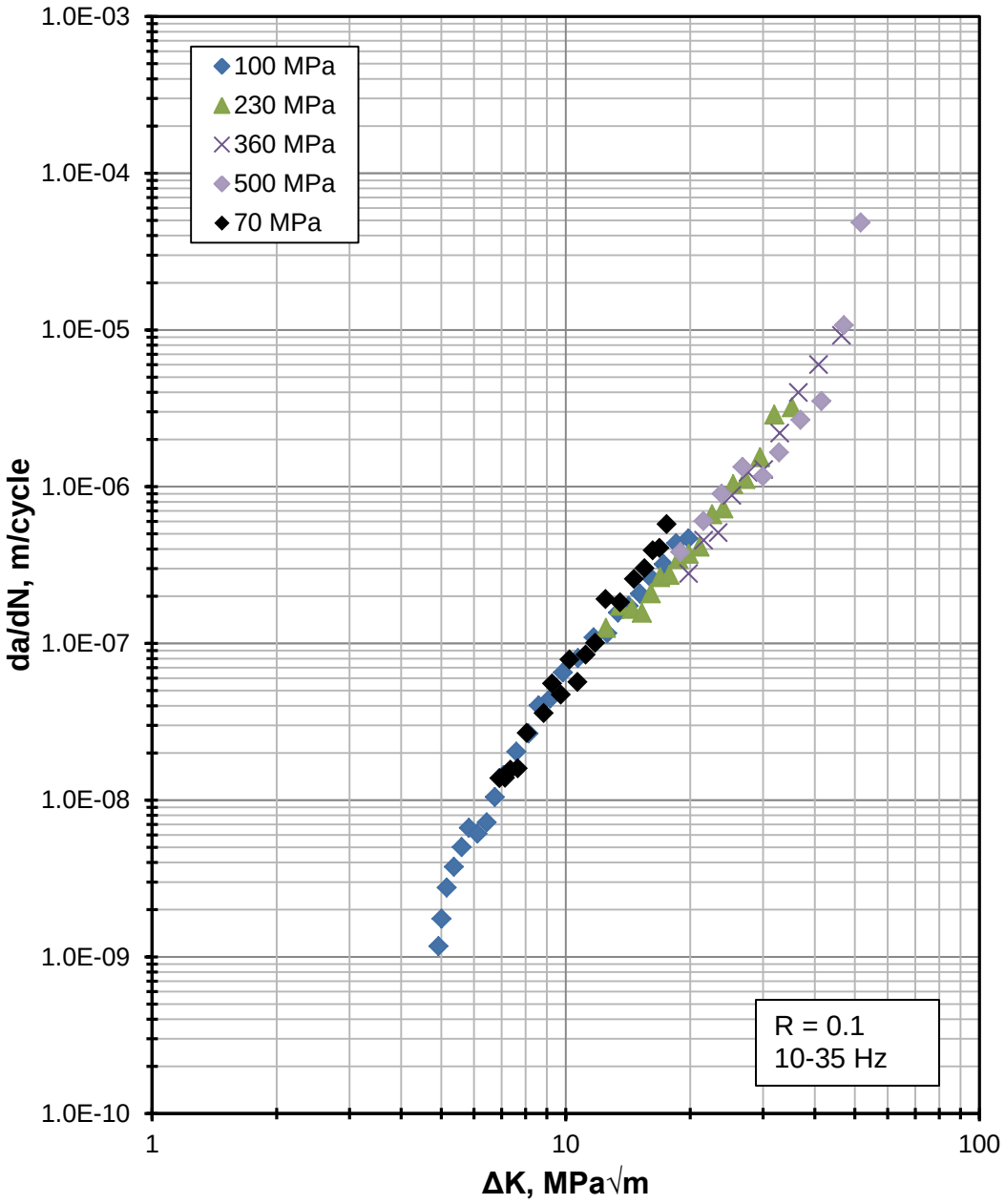

Figure 6.4 Fatigue crack growth rates of PIFed Ti-6Al-4V alloy as a function of ΔK_d (uniform shear displacement) for various stress amplitudes.

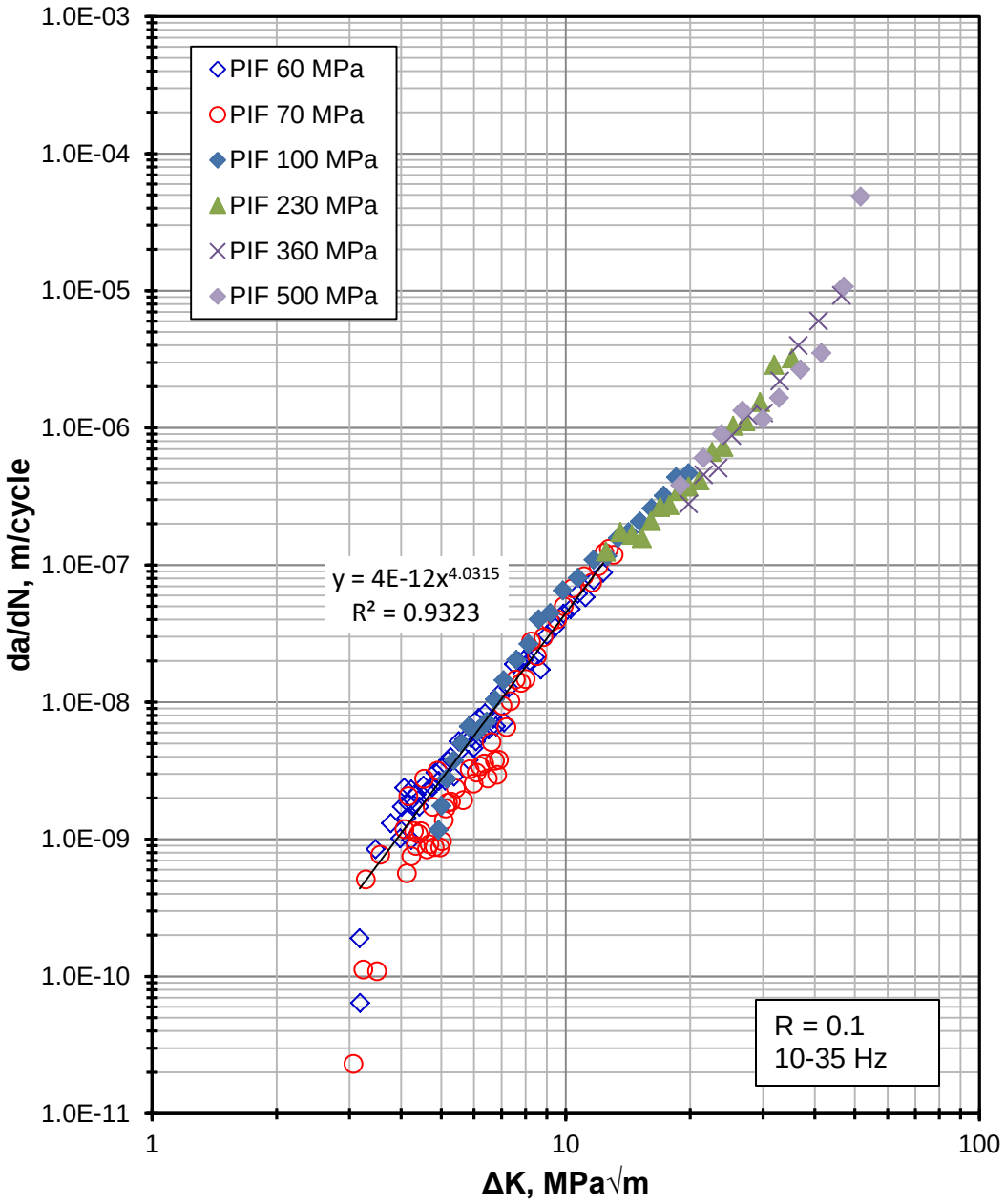

Figure 6.5 Fatigue crack growth curves of HSPT + PIFed Ti-6Al-4V alloy.

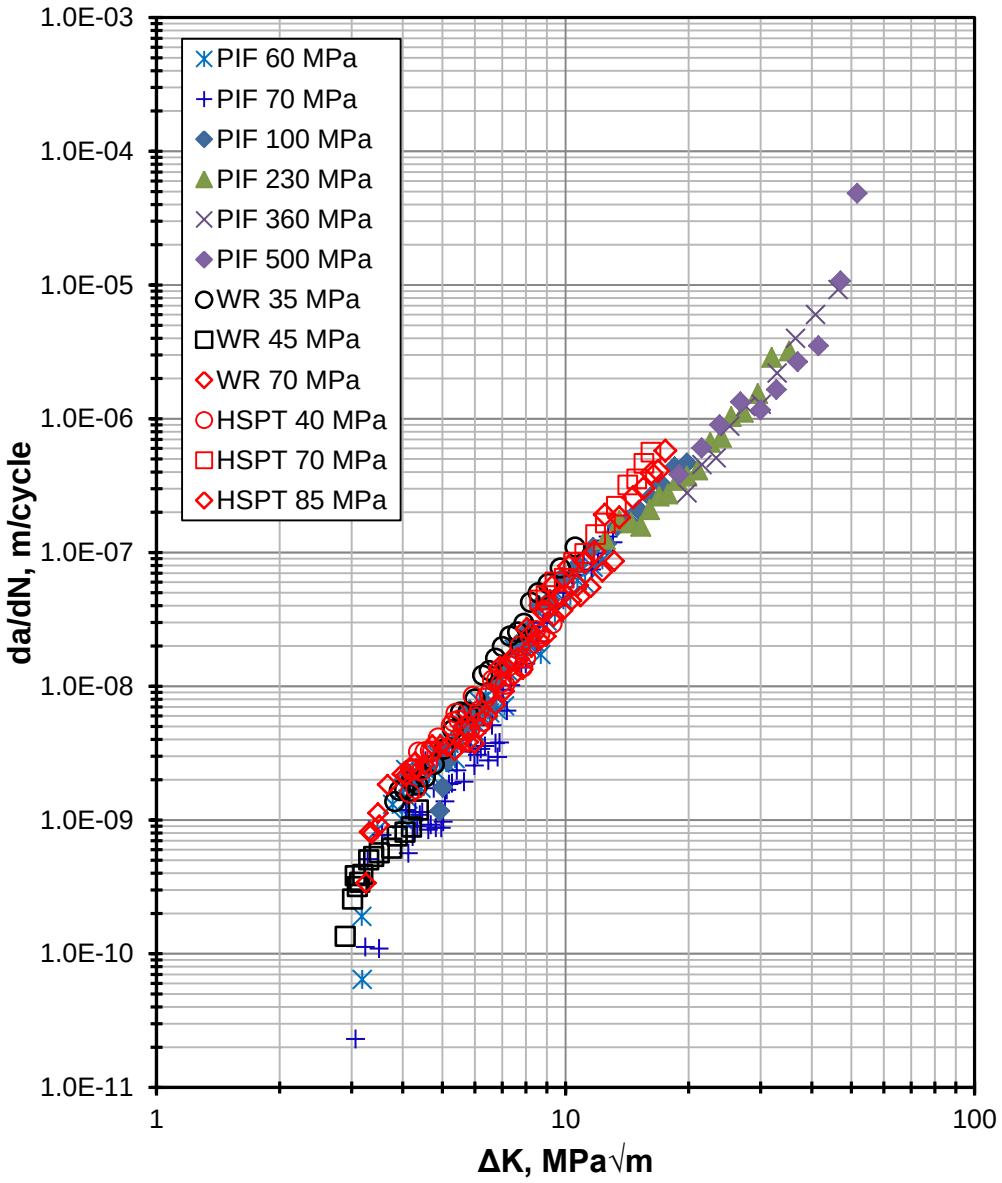

Figure 6.6 Fatigue crack growth curves of HSPT, HSPT + PIFed, and wrought Ti-6Al-4V alloys.

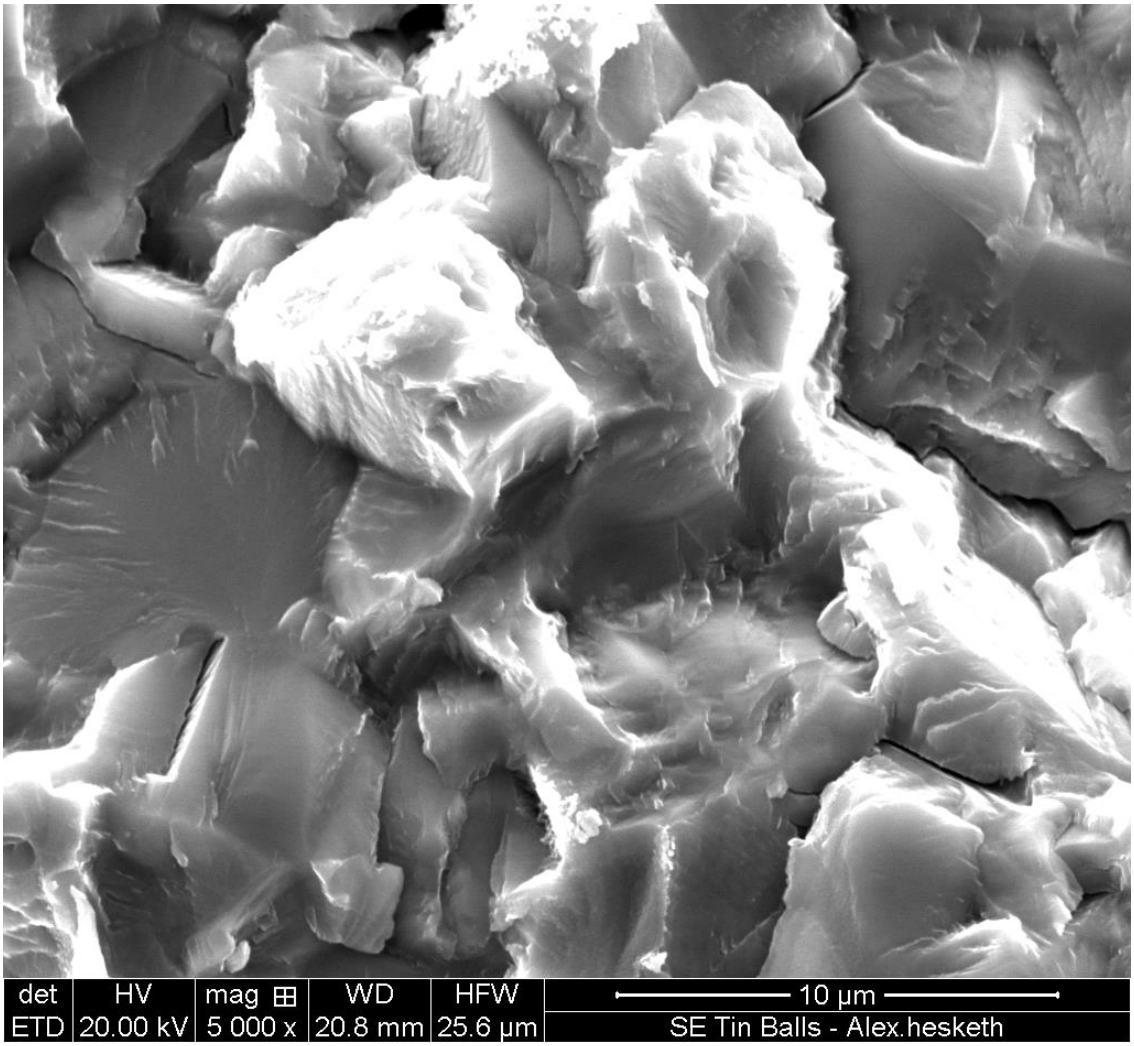

Figure 6.7 Fracture surface of wrought crack growth sample at $\Delta K = 3.7$ MPa$\sqrt{m}$.

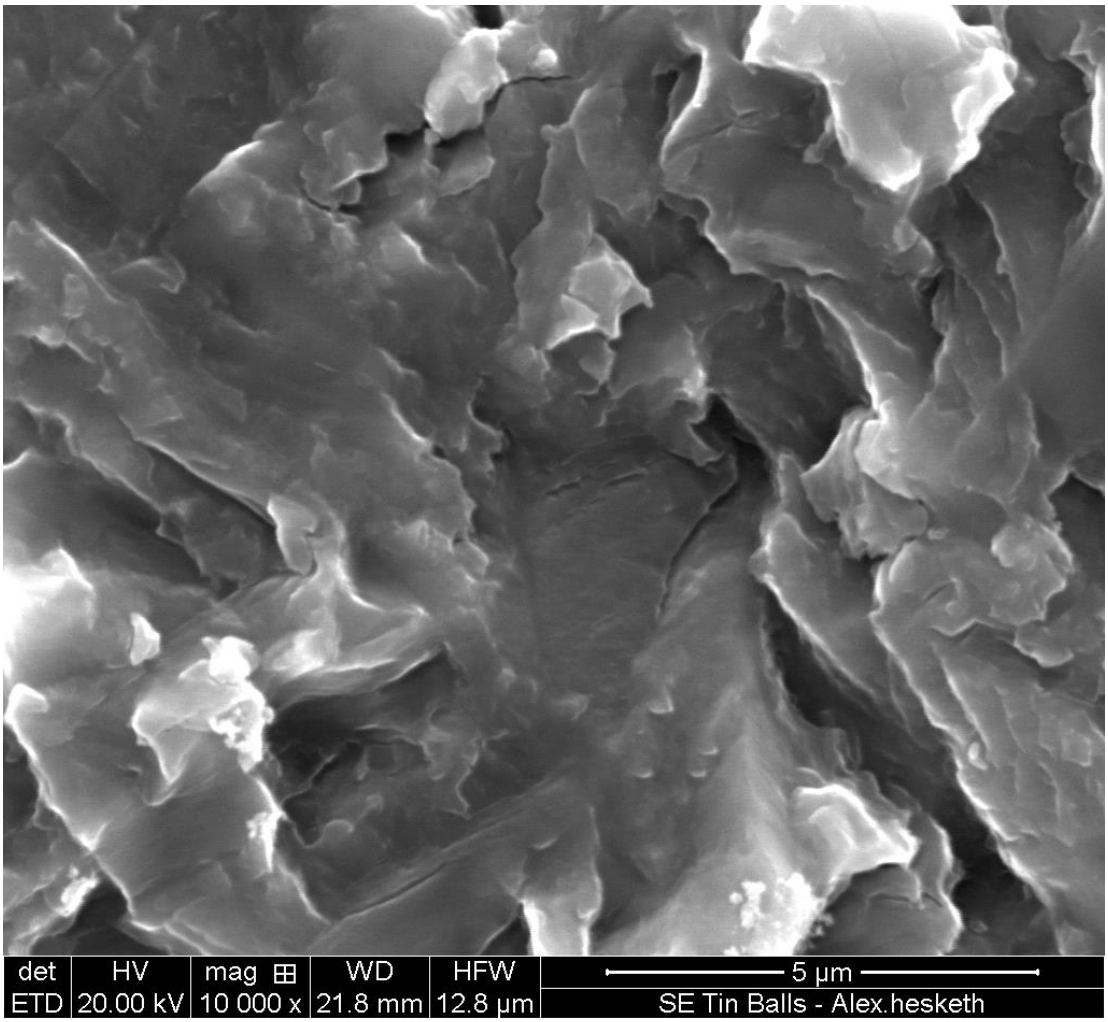

Figure 6.8 Fracture surface of HSPT alloy at $\Delta K = 8.6$ MPa$\sqrt{m}$.

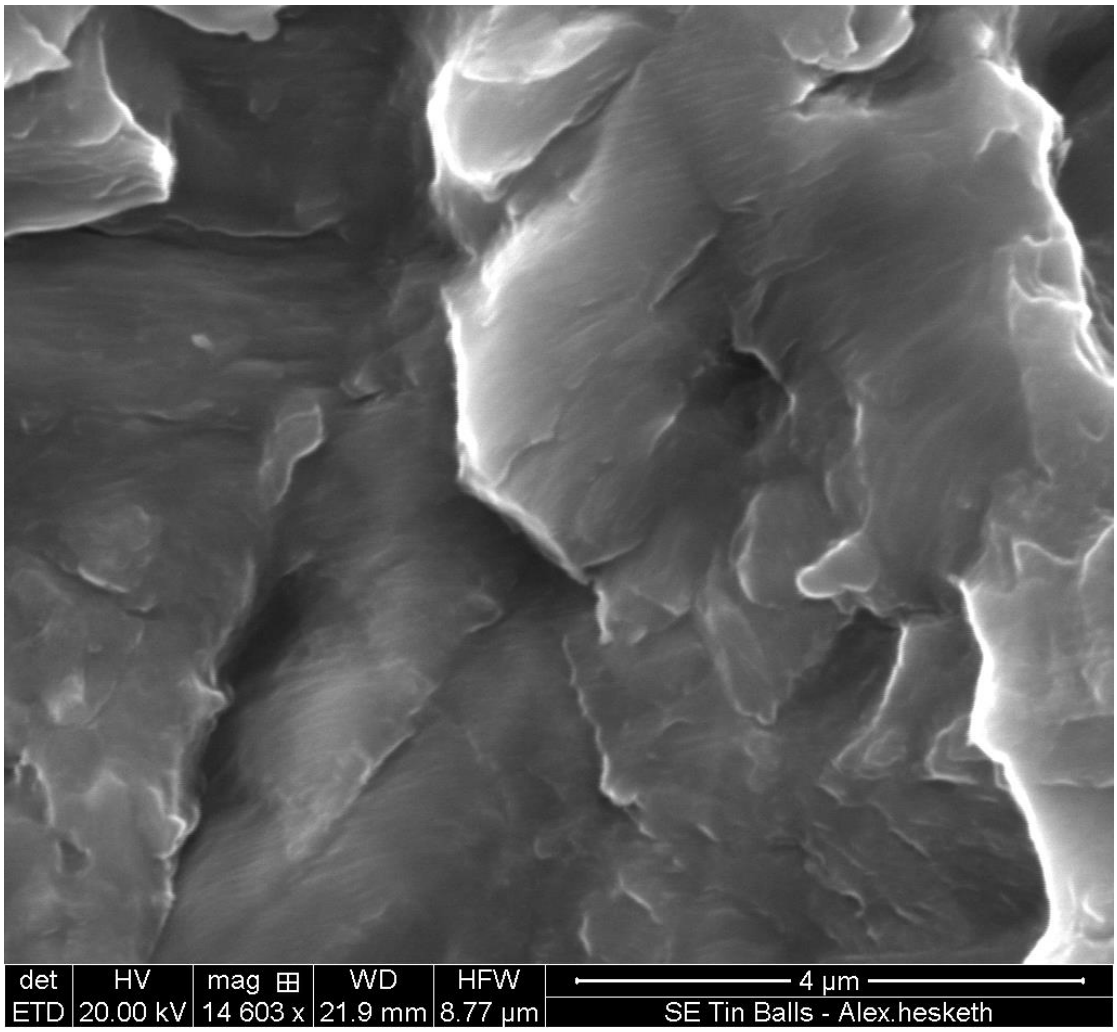

Figure 6.9 Fracture surface of HSPT alloy at $\Delta K = 12.8$ MPa$\sqrt{m}$.

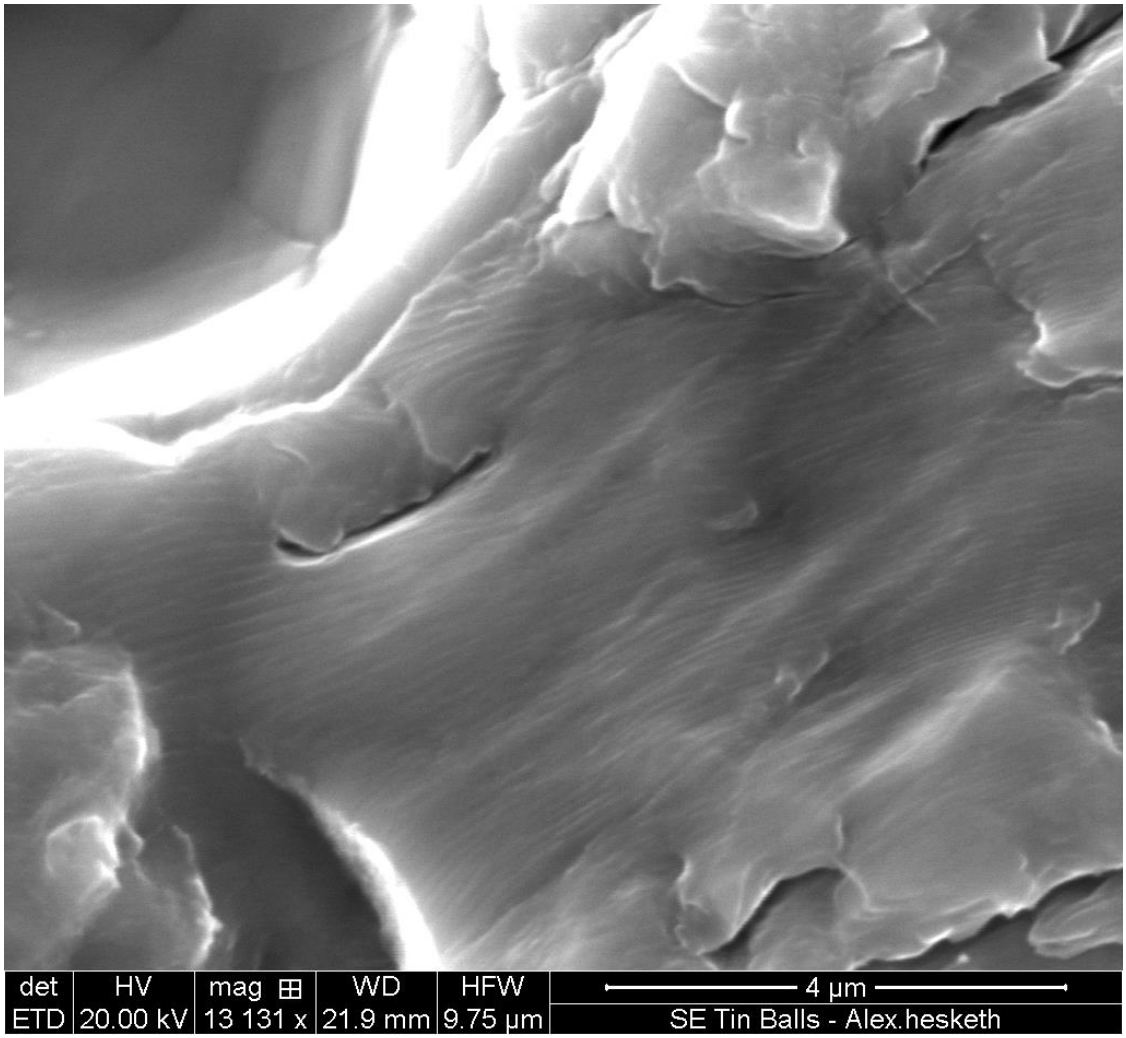

Figure 6.10 Fracture surface of HSPT alloy at $\Delta K = 14.5$ MPa$\sqrt{m}$.

6.4 References

1. D. Arola, J.A. Rouland, and D. Zhang, Expt. Mech. 42 (2002) 380-388.

2. G.E. Lucas, Metall. Trans. 21A (1990) 1105-1119.

3. H. Tada, P. C. Paris, and G. R. Irwin, The analysis of cracks handbook, New York, ASME Press 2 (2000) 52.

4. E.E. Gdoutos, Fracture Mechanics, Spinger Press, MA, 2nd edition, (2005) 53-54.

5. M.A. Astiz, Int. J. Fract. 31 (1986) 105-124.

6. D. G. Rickerby, and P. Fenici, Eng. Fract. Mech. 19(4) (1984) 585-599.

7. C.S. Shin, and S.W. Lin, Int. J. Fatigue 43 (2012) 105-110.

8. H. Oguma, and T. Nakamura, Int. J. Fatigue 50 (2013) 89-93.

9. B.L. Boyce, and R.O. Ritchie, Eng. Fract. Mech. 68 (2001) 129-147.

10. R.K. Nalla, B.L. Boyce, J.P. Campbell, J.O. Peters, and R.O. Ritchie, Metall. Mater. Trans. 33A (2002) 899-918.

11. B. Oberwinkler, Mater. Sci. Eng. A 528(18) (2011) 5983-5992.

12. K.S. Ravi Chandran, F. Cao, and J.C. Newman Jr., Scripta Mater. 122 (2016) 18-21.

CHAPTER 7

FAILURE ANALYSIS AND LIFE PREDICTION

7.1 LCF Failure and Mechanism of S-N Curve Transition

7.1.1 -400 HSPT Ti-6Al-4V Alloy

The S-N plots of -400 HSPT Ti-6Al-4V based on different types of crack initiations are shown in Figure 7.1. Three types of crack initiation were observed: i) surface pore, ii) internal pore, iii) subsurface facet, as discussed in detail in Chapter 4. An obvious S-N transition "knee" was shown near the stress level of 550-600 MPa. The fatigue life suddenly increases by nearly one order of magnitude. The average crack initiation size and corresponding SIF range on the initiators of different types are listed in the Table 7.1. The crack initiation pores were much larger than that observed from polished sections; this indicates that only extremely large pores in the specimen volume were involved in crack initiation.

At high stress LCF regime (for $N_f < 10^6$ cycles), all cracks originated from one or multiple pores at specimen surfaces, as shown in Chapter 4. Under the transition stress level, fatigue failure started from either an internal pore or a facet. Fractographs were shown in Chapter 4. The crack initiation size ranges from ~20 to 300 μm with an average size of 122 μm. When maximum stress decreases to a level, the critical crack initiation size is increased to a size larger than the size of the typical largest pore that can be found

on the surface of the gage section. The existing larger microstructural inhomogeneities inside the bulk, such as GB-α platelets and pores, increasingly govern the fatigue crack initiation process.

It is shown in Table 7.1 that the average equivalent diameter of the surface crack initiation pores is 47.6 μm. According to Murakami's SIF equation[1] for a surface crack:

$$\Delta K = 0.65\Delta\sigma\sqrt{\pi\sqrt{area}} \tag{7.1}$$

the average initial SIF range (ΔK_{ini}) on crack initiation site is 4.24 MPa√m. This indicates that the ΔK on an extremely large pore at the specimen surface is sufficiently big to act as small cracks because it is larger than the threshold value ΔK_{th} (~3.2 MPa√m) of crack growth, as indicated in Chapter 6. These small "cracks" grew immediately at the beginning of cyclic load, which led to much shorter fatigue life when compared with specimens without pores on the surface.

The ΔK value on the average extreme pore size (47.6 μm) on the surface of specimens at the stress level of 550 MPa is 3.70 MPa√m, which is comparable to the critical value, ΔK_{th} (3.20 MPa√m) determined by the current crack growth test. The estimated threshold value is higher due to a few extremely large pores, which lead to higher average extreme-pore size. At the stress levels below this critical stress level, the ΔK value on the average value of extreme surface pores is less than the value of ΔK_{th}. The geometrical factor difference in SIF calculations indicates that the internal defect size should be at least 1.6 times larger than that at the surface to have an equivalent ΔK. As shown in Table 7.1, the average internal crack initiation size is approximately 2.5 times

larger than the average value of surface crack initiations. The advantage of the competition between surface extreme pores and internal extreme crack initiators (pore or facet) inclined to the side of the latter.

As seen in Table 7.1, the average ΔK of the pores/facets under the transition is 4.8 MPa√m, which is slightly higher than that of high stress levels due to increased initiation size, even with lower stress levels. Although the ΔK values above transition (at high stress levels) are lower, the ΔK on the surface is still larger than ΔK_{th}, which is sufficient to grow a crack in air; while the SIF of internal crack initiation site is below the threshold SIF range for crack growth under high vacuum (assume the internal environment is vacuum), ΔK_{thV}, which is experimentally determined to be 7.8 MPa√m by Oguma et al.[2] Thus in the case of HCF failure, the microstructurally small crack (pore or immediately initiated facet) needs to grow to the critical crack size, at which the SIF range is ΔK_{thV}. The cycles needed to grow the original small crack to the critical size leads to the immediate shift of the S-N curve.

The plot of ΔK_{ini} values for LCF from specimen surfaces versus corresponding fatigue lives is shown in Figure 7.2. The fatigue lives of surface initiated failures significantly increase when ΔK_{ini} approaches the ΔK_{th}. It indicates that when the initial ΔK is smaller than ΔK_{th}, a microstructural small crack growth region would occur; the portion of life before the crack becomes critical is much larger than the crack propagation life from a pore that is equivalent to or larger than the critical size. This explains why the fatigue failure mode transition happened at the maximum stress around 550-600 MPa. The stress level of S-N curve transition is determined by the extreme value distribution of the pores on the specimen surface and the ΔK_{th} of the material.

7.1.2 HSPT + PIF and Mill-annealed Ti-6Al-4V Alloys

In pore-free HSPT + PIF and mill-annealed Ti-6Al-4V alloy, the transition (surface fatigue endurance limit) is approximately 800 MPa. The ΔK_{th} is 3.0 MPa$\sqrt{m}$, as shown in Chapter 6. Considering 800 MPa as maximum load, the microstructural unit size should be 13 μm to achieve a ΔK value equivalent to ΔK_{th}. This is approximately the size of α grain in both alloys. Therefore, it is clear that the surface fatigue endurance limit is determined by the ΔK_{th} and the microstructural unit that can act as crack initiator on the specimen surface.

7.2 HCF Failure and Near Threshold Crack Growth

In HSPT Ti-6Al-4V alloy specimens, HCF failures had their cracks started from either internal pores or facets, as illustrated in Chapter 4. In HSPT + PIF alloy, HCF failures always initiated from big α phase (it could be GB-α plate, or large α grains adjacent to GB). HCF cracks initiated from a cluster of facets in mill-annealed Ti-6Al-4V alloy with fine equiaxed α grains. Thus the HCF crack initiation of Ti-6Al-4V alloys in the present study can be classified into two types: extremely large residual pores and facets originate from big α phase particles. As the average value of ΔK_{ini} is much smaller than the ΔK_{thV}, the crack extension around the initiation site is actually a microstructural small crack. The crack growth near this threshold region is dependent on the microstructure[3] and consumed most portions of the total fatigue life.[4] The fractographic characteristics of the crack growth in both types of failures at different stages will be studied in this section to reveal the underline mechanisms.

7.2.1 HCF Crack Initiation from Internal Pore

Fish-eye like failure was formed from internal pore/facet in HCF specimens. Figure 7.3(a) shows an internally fractured specimen from a pore. A rough zone can be seen near the pore; beyond the rough zone a region darker than other regions tangential to the specimen surface can be seen; this is a typical feature for "vacuum" crack growth. ΔK on the border of the rough zone is 8.6 MPa√m. Inside the rough zone, facet and granular were observed. Figure 7.3(b) shows a flat region near the sharp tip of the pore; fine granular is seen at the adjacent areas near the border of facets. Multiple cross slip marks were seen on the facet, where ΔK is ~6.7 MPa√m. Stair-like steps are also seen in this region, which indicate that at this stage, crack extension was driven by the activation of single or multiple slip systems. The pore presented as a crack initiator, but the ΔK on the pore is not sufficiently big to behave like a long crack; the micro-crack (pore) preferred to grow as a stage I crack with crystalline manner. Based on extensive fractographic observations, it can be generalized that when the stress intensity is relatively small, only single slip bands (paralleled bands) can be observed on the facet, as the stress intensity increases to a larger value, multiple slip bands (crossed bands) can be observed. This is in good agreement with the microstructural small crack growth manner that was experimentally observed by Künkler et al.[3]

Figure 7.4(a) shows another specimen failed from a pore deep inside the bulk. This happened because of the presence of a larger pore deep inside the bulk, while the surface and near surface region lack a pore/phase particle that has equivalent ΔK. A mixed region of facet and fine granular (rough zone), shown in Figure 7.4(b), is present from the adjacent area of the pore with a ΔK value of 5.7 MPa√m, to the end of the rough area,

where the ΔK value is 9.2 MPa√m. Beyond that, granular was observed until the crack intersects the specimen surface, Figures 7.4(c) and (d). According to Oguma et al.,[5] granular can be observed on the fractograph for crack grown under vacuum. It turns out that failure from deep inside the pore has relatively longer life than the ones located near the surface, even though the initial ΔK is higher. The above observations show granular was found in the facet prevail areas and beyond this area but still under vacuum. Pristine facets with clear slip-marks and convex granules, Figures 7.3(b) and 7.4(b), indicate there was no significant crack closure at low ΔK regime. However, in a crack deep inside the bulk, a darker and more rounded granular and flat region were seen until the crack reaches the surface, as shown in Figures 7.4(c) and (d). This might be caused by the pseudo-vacuum environment with ΔK beyond threshold and more pronounced plasticity induced crack closure under plane strain constraint.[5, 6]

7.2.2 HCF Crack Initiation from Near Surface Facet

Facet-initiated HCF failures are generally very close to the specimen free surface, as GB-α and extreme α grains are commonly seen throughout the microstructure. Figure 7.5 shows a specimen initiated from facets just under the surface. Paralleled slip marks can be seen on the facets, as shown in Figures 7.5(b), (c) and (d). A few stair-like steps were also seen on the facet. The formation of these steps was thought to be caused by small slip band coalescence, or due to step-by-step crack extension. The magnified view of the step is shown in Figure 7.5(d). Arrow-indicated areas show clusters of granular at the step zone; this was caused by the separation of the dislocation cells resulted from cyclic strain

accumulation according to Chai et al.[7] The step-by-step extension of a small crack or coalescence of micro-cracks makes it possible to grow to a critical size.

The ΔK at the border of the facet is 4.1 MPa$\sqrt{m}$. As it is just under the surface, it immediately intersected with the surface when it reached the current size, than grew as a surface crack. So the extension procedure of this facet region was thought to be consumed most of the total fatigue life. The crack extension procedure within the facet region leads to a much longer life than the specimens that have a pore with similar size at or just under the specimen surface. But the life is still much shorter than that of a specimen failed from inside, as seen in the case of Figure 7.3. When the facet intersects with the specimen surface, even though its size is still small enough to grow as a microstructurally small crack, the speed increased immediately when expose to air, while an internal crack can still grow as a microstructurally short crack under vacuum until the crack becomes a long crack. Thus internal crack-initiated failures exhibit considerably longer life than the ones just under the surface.

The orientation of this crack initiation facet was determined by using EBSD as it was. The facet orientation was adjusted carefully by tilting and rotating the specimen holder to achieve high Kikuchi pattern index confidence (~0.6), where the total tilting angle is ~70˚. The facet was approximately 38˚ away from the loading axis. It was shown in Figure 7.6(c) that the orientation of the facets is very close to the basal plane. The orientations of crack initiation facets were not examined one by one for all the specimens.

7.2.3 HCF Crack Initiation from Internal Facet

The representative HCF crack initiation sites from internal facet are shown in Figure 7.7. Figure 7.7(a) shows a fish-eye type HCF failure of PIFed Ti-6Al-4V from a large facet. Smaller facets and granular are also seen in the brighter rough area beyond the facet (Figure 7.7(b)). Figure 7.7(c) is the HCF crack initiation site of the mill-annealed alloy; a brighter rough area similar to that shown in Figure 7.4 is also observed. The magnified image (Figure 7.7(d)) shows a cluster of facts; each of them has a size comparable to the size of α grain (~10 μm). Fine granular regions appear in between these facets.

The internal crack initiation facets were found to deviate from the loading axis to an angle, which is common for stage I crack growth. The profile (Figure 7.8) near the crack initiation site of the sample shown in Figure 7.7 (a) was determined using an optical surface profiler. The crack initiation facet is at the intersection point of line I and II. The facet tilted a lot from the loading axis, and the adjacent areas are generally normal to the loading axis though they are different in height, as shown by the topography and the profiles along line I and II. These facets were found inclined to the loading axis about 30-60 degrees, which means the small crack grew in a mixed mode (I and II). The mode II loading causes slip on planes parallel to the crack. The crack extension in this stage was driven by crack tip slide displacement.[9] The mode I loading causes slip on planes inclined to the crack plane and so blunts the crack tip by activating other slip systems. As illustrated in the previous contents, the rough area at the boarder of the primary crack initiation facet consists of smaller facets and fine granular in-between these small facets. This indicates that the microstructurally small crack grows in a crystallographic manner

and is driven by a single or double slip mechanism by absorption of dislocation dipoles during cyclic load.[811] This region is the region defined by Umezawa et al. as the border area in HCF failure of high strength steels.[12]

In situ crack growth observation showed that it took a lot of cycles to blunt a crack when the crack is microstructurally small (at near threshold region). Thus microstructurally small cracks grow in an intermittent manner. The crack growth rate increases when it passes through a grain boundary and is arrested when it approaches a grain boundary. The region ahead of the crack tip has highest stress concentration; dislocations pile up at the end of slip length. Continuous dislocation accumulation results from very small strains during each cyclic loading can cause an exhaustion of local plasticity.[13] The procedure takes a lot of cycles to accomplish, but it enables the combination of micro-cracks involved from slip bands to grow the crack to a critical size. When the grain at the crack tip is oriented properly, such as the easy slip basal plane, or planes with high Schmid factor, the crack can easily transmit to it and pass through; however, when the grain is “hard”, cyclic softening at the local plasticity exhausted zone creates dislocation cells. This leads to severe damage of the material at the crack tip. Fine granular regions near the subsurface crack initiation site of titanium alloys reported recently, were found to come along with facets at the HCF crack initiation site.[14-17] The mechanism presented above is the most possible formation mechanism of the granular regions at the rough area.

7.2.4 Summary of HCF Failure Mode

The analysis of HCF failure patterns indicates all these three materials had their HCF crack initiated from internal pores, facets just under the surface, or at the inside of a specimen. In the case of a facet just beneath the specimen surface, the fatigue life totally depends on when the microstructural small crack intersects with the specimen surface. Once the microstructural small crack is exposed to air, the crack growth rate suddenly increases by 10 to 100 times[2]; the remaining life portion is very small. The location of this type of crack initiation site determines the size of a microstructural short crack that can grow under vacuum conditions and cause life scatter. This type of failure is usually observed at intermediate-to-high cycle fatigue range. It is as a transition failure mode between surface and internal crack initiated failures. The schematic of this type of failure is shown in Figure 7.9.

With the further decrease of cyclic loading stress, the crack initiation completely shifts to internal. Internal pore/facet-induced HCF failures exhibited a fish-eye like pattern, which contains a clear rough area at the outer boundary of the crack initiator (pore/facet). The rough area was considered to be the symbol of stable crack growth retardation. The delayed crack growth stage transition results in the fatigue failure mechanism change, which has a much longer fatigue life. If the defect size is equivalent to grain size, the transition would not happen; the failure will constantly initiate from the specimen surface. However, if the size of phase particle or pore for crack initiation is larger than the critical unit size for ΔK_{RA}, lower critical stress level is required to form fine granular to obtain HCF, as the critical threshold crack size increases with the decrease of stress level.

Figure 7.10 shows the schematic presentation of HCF failure modes of mill-annealed and HSPT Ti-6Al-4V alloys. The only difference is that crack origin size of HSPT processed alloy is larger than that of mill-annealed alloy. As analyzed in Chapter 5 and illustrated by Figure 7.10, the crack origin (pore/facet) size has a major effect on fatigue life. In HSPT PM Ti-6A-4V alloys, thick GB-α plates or big α grains have high Schmid factors that are ready to initiate a crack by slip and propagate very fast to a critical size because there is no obstacles to constrain the slip. This reduces the crack initiation resistance. However, in the mill-annealed alloy with fine homogeneous equiaxed grains, the available slip length is confined in the length of the grain size. The homogeneous fine grains impeding the capability of dislocations to move and thus crack initiation or short crack propagation are retarded, resulting in longer HCF life.

7.3 Quantitative Fractograph Analysis and HCF Life Prediction

7.3.1 Introduction

It has been shown that the fatigue crack initiation site transits from surface to internal at high or very high cycle fatigue failures. The surface-to-internal crack initiation transition usually happens around 10 million cycles for mill-annealed and bio-modal Ti-6Al-4V alloys.[17, 18] This was also confirmed in this study. Subsurface crack initiation in titanium alloys from facet was discovered in the 70s in high cycle and very high cycle fatigue regime.[12,19,20,21] It was illustrated that the initiation life share at different stress levels increases with the decreasing of stress level.[22] Research on the microstructurally small crack extension mechanism is experimentally difficult, especially for internal crack

initiations, because it is small in dimension and dependent on local microstructure, which cannot be described using linear-elastic fracture mechanics.[23]

Eylon et al.[24] have shown that larger facet size generally corresponds to shorter total life in investment-cast and HIPed Ti-6Al-4V with lamella microstructure. Variation of microstructural inhomogeneity is the main reason that leads to fatigue life variation. Liu et al.[14] found that the SIF range for the rough region (facet and granular) is almost constantly located at the threshold value for crack growth threshold in high vacuum (7.8 MPa$\sqrt{m}$).[40] However, HCF crack-initiation facets are almost the same in size in wrought Ti-6Al-4V alloys. It is hard to generalize that the constant rough area ΔK is applicable for HCF initiations with different sizes and types, or for other microstructures.

PM Ti-6Al-4V has inferior HCF properties due to its microstructural discontinuities, such as massive grain boundary, large phase particles, inclusions, and porosity. Since the small crack growth from the crack origin to critical (LEFM applicable) plays a significant role in HCF, the investigation of the correlation between microstructural discontinuity (crack origin) size and HCF life of Ti-6Al-4V would shine a light on the microstructure tailoring, process optimization and cost control. A large amount of fractographic observations showed there exist some correlations between crack initiator size, rough area size, and HCF life. This section is dedicated to find the reason of fatigue life drop of the powder metallurgy Ti-6Al-4V, and estimate crack growth rate in near threshold crack growth stage. In this section, quantitative fractograph was used to reveal the relationship between HCF life and the crack origin size, as well as the correlation with crack origin ΔK in materials with different microstructures.

7.3.2 Quantitative Fractography Analysis

The HCF data of different materials in this study with fish-eye like failure are shown in Figure 7.11. As-HSPT alloy shows scattered and a worse HCF performance; HSPT + PIF alloy shows a smooth trend and higher fatigue strength. The fatigue performance of these two materials is inferior to that of the mill-annealed alloy.

The ΔK_{ini} and ΔK_{rough} were calculated from the following equation:[25]

$$\Delta K = 0.5\Delta\sigma\sqrt{\pi\sqrt{area}} \tag{7.2}$$

The area of crack initiation site (pore/first smooth facet) and rough area were used to calculate the ΔK_{ini} and ΔK_{rough}, respectively. The values of ΔK_{rough} are shown in Figure 7.12, in which most data are between 7 to 9 MPa√m. This is generally consistent with the values for wrought Ti-6Al-4V alloy, which is 6 to 8 MPa√m, as determined by Liu et al.[14] This result also approximate to the value of the threshold for crack growth (7.8 MPa√m) under ultra-high vacuum environment was determined using a compact tension specimen by Oguma et al.[2] The present investigation confirms that the size of rough area is the intrinsic characteristic size of crack initiation (microstructurally small crack growth range) for a fatigue crack originating from the interior of a specimen.

The values of ΔK on initiation site (ΔK_{ini}) are also shown in Figure 7.12, which are lower than those of the rough areas. The value of ΔK_{ini} displays a decreasing trend with respect to failure life, and then reaches a constant value, within the range of 2-3 MPa√m, to achieve a fatigue life more than 10 million cycles. As facet-induced crack origins are close to the specimen surface, the distance from the nearest point to the specimen surface

is in the range of a few hundred μm, thus a generally liner trend was obtained. However, the location of HCF failure initiated from internal pores is random; some of them are just under the specimen surface; this type of crack origin follows the trend of facet-induced failure; some are deep inside the volume, which means the crack can grow under "vacuum" for a much longer range. In this type of failures, even though ΔK_{ini} is larger, their fatigue life is similar to the failures that have lower ΔK_{ini} values but much closer to the specimen surface, as shown by the solid circle symbols in Figure 7.12. It is shown that the location of crack origin has a noticeable effect on fatigue life.

Figure 7.13 shows the measurements of both rough area and crack initiation sizes (in √area) as a function of the applied maximum stress. It is shown that both the rough area size and initiation size decrease with the increasing of maximum stress level following power function trends. At the same stress level, specimens with fatigue life $>10^7$ cycles have much smaller initiation size compared to that of samples failed within 10^7 cycles. A few exceptions deviated from the fitted line due to the variation of initiation site location. A deep inside crack initiation site with larger size would also lead to a runout life, a data far off the trend line, due to larger area crack growth with a slower rate under vacuum environment.

The size of the rough area is only related to stress level, as shown by the plot in Figure 7.13; it increases with the decreasing of stress level, and is independent from microstructure (lamellar or equiaxed), and crack origin type (facet or pore). Thus, it is demonstrated that the size of the crack origin, which could be first smooth facet or pore, is the dominant factor that determines the HCF life for internal failures. Smaller primary crack origin would leave a larger margin for growing a microstructurally small crack

before it reaches the critical rough area size. Basically, the fatigue life is dependent on the size difference between the rough area and the crack initiation area, as illustrated in Figure 7.10. The correlation between HCF life and crack origin size indicates that when the extreme size microstructural discontinuities, which act as crack origin, inside the microstructure are well examined, the HCF strength can be predicted.

In the comparison of HCF failures from a facet and a pore with similar size, no distinct life difference was found. This indicates that the HCF life is more crack origin size dependent, and seems not affected significantly by the crack initiation type. From another perspective, it also demonstrates that the initiation life of a shear crack in a single α particle can be almost neglected. This was confirmed by Bache et al.[26,27] that strain accumulation induced slip happens almost immediately in grains with proper orientation upon cyclic load.

7.3.3 Near Threshold Crack Growth Rate

The fish-eye is always tangential to the specimen surface. Thus the fatigue life beyond fish-eye can be neglected. The fatigue life consumed from fish eye to K_{1C} was calculated to be in the order of 10^4 cycles, which is less than 1% of the total life in the order of 10^6 to 10^7. However, the fatigue life consumed from rough area to fish-eye is important as the crack origin location varies from sample to sample. The crack growth at this region is actually under pseudo-vacuum environment and behaves like a long crack. In this region, the crack growth rate is much lower than the crack growth rate tested under air at the same ΔK level.[28,29] There is no rough area-to-fish-eye region for specimens had their rough area extended to the specimen surface.

It is evident that the Paris relation is acceptable to describe the crack growth process in the stable crack growth region. Paris equation (7.3) obtained from crack growth data (Figure 6.5) was used to calculate the fatigue life consumed from the rough area to fish-eye region.

$$\frac{da}{dN} = 4 \times 10^{-12} \Delta K^{4.03} \tag{7.3}$$

$$\mathrm{N} = \frac{2}{2.03 \times 4 \times 10^{-12} \times \left(0.5\sqrt{\pi}\right)^{4.03} \times \Delta\sigma^{4.03}} \left[\frac{1}{\sqrt{area}_{ro}^{1.015}} - \frac{1}{\sqrt{area}_{fe}^{1.015}} \right] \tag{7.4}$$

$$N_{RA-FE} = 10N \tag{7.5}$$

The crack growth from rough area to fish-eye is actually a vacuum environment. As shown by the fatigue crack growth data under air and high vacuum,[2] at the beginning of long crack growth region, the crack growth in high vacuum is approximately one order of magnitude slower than that in air at same value of ΔK. Thus a coefficient of 10 was used to obtain the fatigue life consumed from rough area to fish-eye, equation (7.5). The calculated life consumed from the rough area to fish-eye region and life portion are shown in Table 7.2.

The values of average crack growth rate within rough area were calculated from the rough area size and the fatigue life consumed by this region using the following equation:

$$\frac{da}{dN_R} = \frac{a_{ro} - a_{ini}}{N_f - N_{RA-FE}} \tag{7.6}$$

The results are shown in Table 7.2 and Figure 7.14 (diamond symbols). It is observed the crack growth rate within rough area, da/dN_R, is between 10^{-12} and 10^{-11} m/cycle, and the value decreases with the increasing of fatigue life, as shown in Figure 7.15. This was validated by Y. Hong et al. by using the Tanaka–Mura model.[17] This demonstrates that the microstructurally short crack can grow at higher ΔK values with lower rates at the internal of a specimen. The current available experimental fatigue crack growth data[2,28,29] of Ti-6Al-4V alloy under vacuum is also shown in Figure 7.14. The current calculated near threshold crack growth rate is lower than the experimental data detected by McClung et al.[28] and Irving et al. 29, and matches perfectly at the ΔK value of ~ 8 MPa√m with a crack growth rate of 10^{-10} m/cycle.

7.3.4 HCF Life Prediction

The calculated near threshold fatigue crack growth rates within the rough area were fitted to be:

$$\frac{da}{dN_R} = 6 \times 10^{-15} \cdot \Delta K_{IR}{}^{4.38} \tag{7.7}$$

$$N_R = \frac{2}{2.38 \times 6 \times 10^{-15} \times \left(0.5\sqrt{\pi}\right)^{4.38} \times \Delta\sigma^{4.38}} \left[\frac{1}{\sqrt{area_{ini}}^{1.19}} - \frac{1}{\sqrt{area_{ro}}^{1.19}}\right] \tag{7.8}$$

The fatigue lives consumed by the rough area for each specimen are also shown in Table 7.2. At the HCF region, the life portion consumed within rough area is mostly more than 98%, except a few specimens with their crack origin from deep inside pores. For simplicity, the rough area consumed fatigue life was taken as the total life. The calculated

HCF lives based on equation (7.8) for specimens with different crack initiator sizes are shown in Figure 7.16. The dimensions in √area (μm) in the parenthesis are average crack initiator sizes of different specimens.

The predicted curve for specimens with a size of 200 μm matches well with that of HSPT specimens, which have an average initiation size of 161 μm. However, in real S-N curve, the fatigue crack initiation size increases with the decreasing of stress level. As shown in Table 7.2, most HCF failed HSPT specimens have a crack initiation size around 200 μm with two exceptions; the two much smaller sizes lead to a much lower average value. In general, the predict lives fairly agree with the real fatigue lives of HSPT specimens.

The predicted lives for HSPT + PIF and mill-annealed specimens are much higher than the real fatigue data. The shape of HSPT + PIF specimens' initiation site usually has a high aspect ratio because they are usually originated from the grain boundary α phase plate. Thus the real slip length in these specimens should be much higher than the size of √area, which means the real ΔK should be larger than the values calculated from √area. This is just one possible reason for higher predicted life. Since the aspect ratio and sizes are random, the shape factor was not taken into account during ΔK calculations. The HSPT microstructure shows that α grain near the grain boundary plate is larger and has some common orientation relationships with their neighbor grains. These features might lead to a weaker microstructural barrier at the beginning of the microstructural small crack growth region.

Since it is almost impossible to remove all the micro-textures in wrought Ti-6Al-4V alloy even after annealing, the slip length is not necessarily confined in one grain when

slip happens. Stain concentrations that exist somewhere between two to three grains have proper orientation combinations, where slip can easily transmitted to neighbor grains, as shown in Figure 7.17. There is almost no granule in-between a few grains with similar tilt angle and the slip marks show that slip happened continuously. Thus the effective crack initiation size in mill-annealed Ti-6Al-4V is a few times larger than the α grain size due to micro-textures.

Table 7.1 Average values of crack initiation size and ΔK_{ini}.

Initiation type	Average initiation diameter, μm	Average Δk_{ini}, MPa$\sqrt{m}$
Surface pore	47.6	4.24
Internal pore	160.1	5.00
Facet	96.6	4.86

Table 7.2 Results of quantitative fractography analysis data and calculated internal crack growth rate at near threshold region.

Sample	Failure type	$\sigma_{max,}$ MPa	$N_{f,}$ cycles	$\sqrt{area}_{ini,}$ μm	$\Delta K_{ini,}$ MPa$\sqrt{m}$	$\sqrt{area}_{ro,}$ μm	$\Delta K_{rough,}$ MPa$\sqrt{m}$	$(\Delta K_{ini}+\Delta K_{rough})/2$ MPa$\sqrt{m}$	$N_{RA\text{-}FE,}$ cycles	$N_{RA\text{-}FE}/N_f$	da/dN_R, m/cycle
WR-1	Facet	720	18,547,329	11.75	1.97	185.30	7.82	4.89	77,571	0.42%	5.30E-12
WR-2	Facet	735	16,338,927	12.12	2.04	163.02	7.48	4.76	66,360	0.41%	5.23E-12
WR-3	Facet	680	30,721,500	17.46	2.27	185.64	7.39	4.83	87,959	0.29%	3.10E-12
PIF-1	Facet	480	32,272,193	64.52	3.07	535.26	8.86	5.96	113,019	0.35%	8.26E-12
PIF-2	Facet	510	16,945,546	43.17	2.67	351.82	7.63	5.15	0	0	1.03E-11
PIF-3	Facet	550	98,828,33	63.84	3.50	345.76	8.16	5.83	102,947	1.04%	1.63E-11
PIF-4	Facet	750	2,652,718	73.79	5.14	215.39	8.78	6.96	64,071	2.42%	3.09E-11
PIF-5	Facet	600	5,899,327	94.67	4.66	266.70	7.81	6.23	142,007	2.41%	1.69E-11
HSPT-1	Pore	520	7,469,674	187.20	5.67	439.66	8.69	7.18	109,746	1.47%	1.94E-11
HSPT-2	Pore	520	2,624,586	164.27	5.31	360.90	7.88	6.60	152,243	5.80%	4.49E-11
HSPT-3	Pore	600	2,128,184	186.30	6.53	373.60	9.25	7.89	104,303	4.90%	5.22E-11
HSPT-4	Pore	480	2,867,847	175.09	5.06	371.97	7.38	6.22	224,850	7.83%	4.20E-11
HSPT-5	Pore	450	3,964,901	193.56	4.99	426.18	7.41	6.20	0	0	3.31E-11
HSPT-6	Pore	400	18,076,215	213.12	4.66	644.98	8.10	6.38	243,588	1.35%	1.37E-11
HSPT-7	Pore	500	10,114,340	189.76	5.49	586.12	9.65	7.57	137,167	1.36%	2.24E-11
HSPT-8	Facet	450	16,764,731	91.36	3.43	379.96	6.99	5.21	0	0	9.71E-12
HSPT-9	Facet	480	36,600,965	52.54	2.77	536.33	8.86	5.82	0	0	7.46E-12

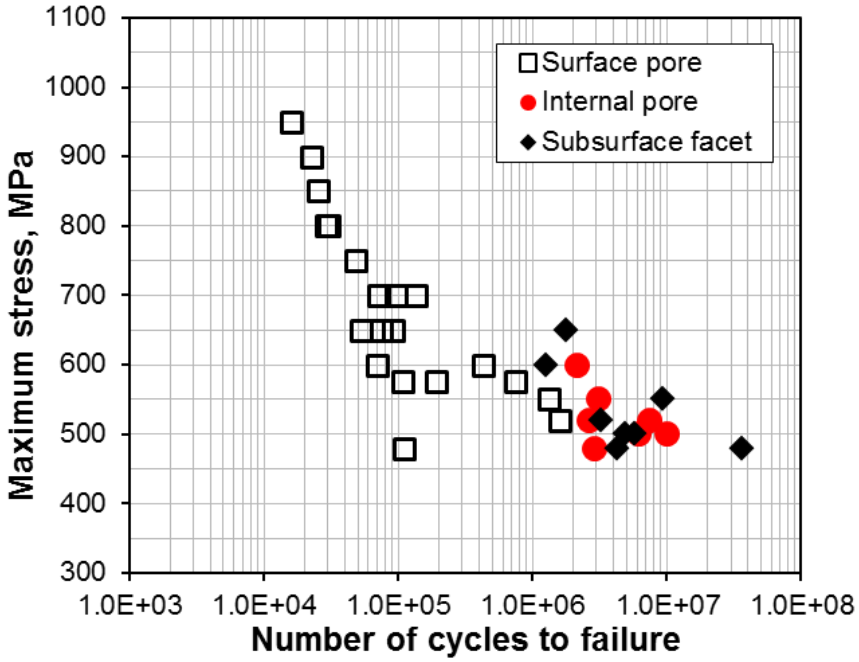

Figure 7.1 S-N plots of Ti-6Al-4V alloy by HSPT process based on failure initiation type and location.

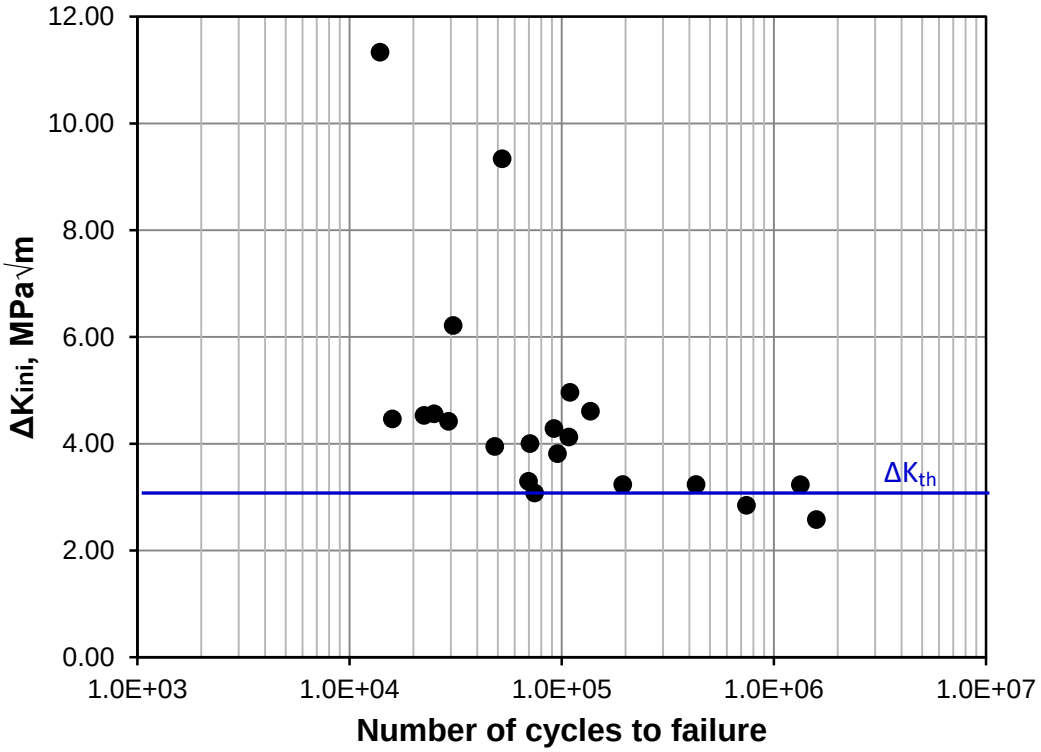

Figure 7.2 ΔK_{ini} as a function of fatigue life for surface initiated failures.

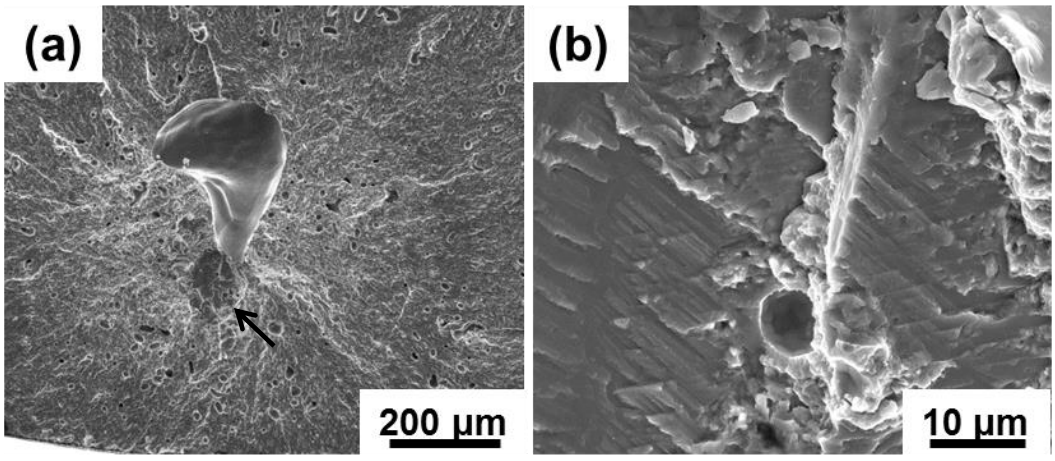

Figure 7.3 HCF failure from an internal pore, (a) σ_{max} = 520 MPa, N_f = 7,469,674 cycles, (b) magnified view of the arrow-indicated area in (a), ΔK = 6.7 MPa$\sqrt{m}$.

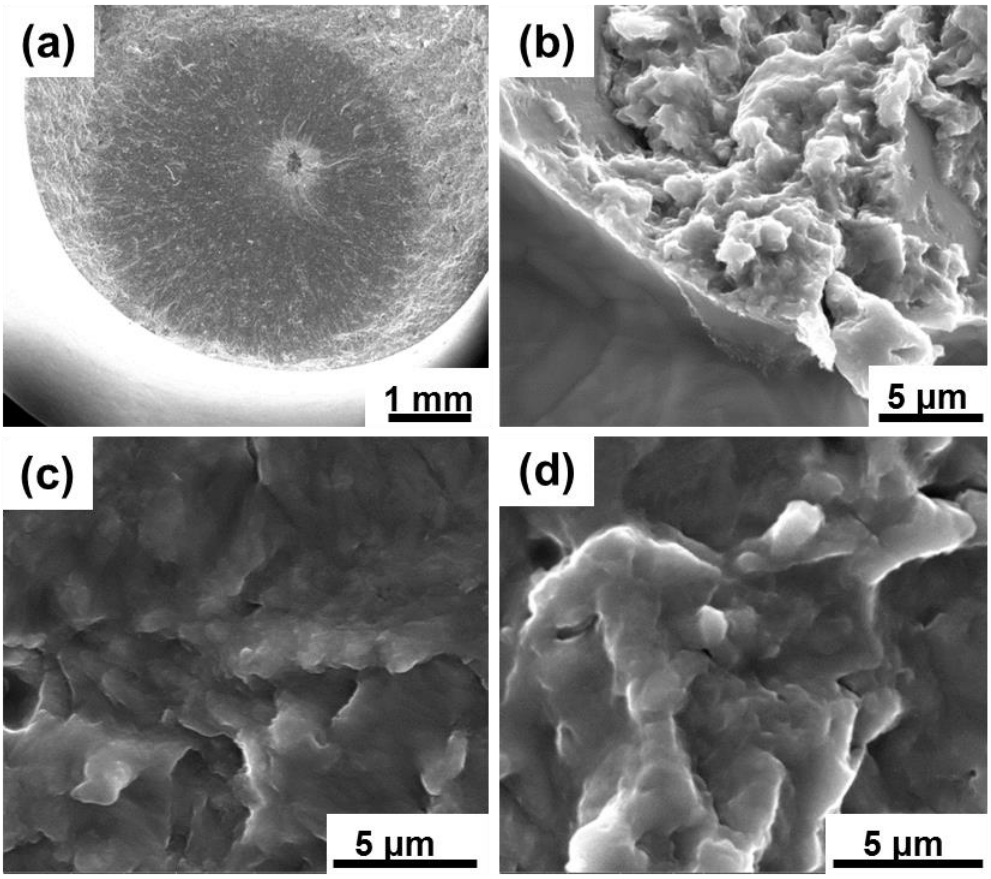

Figure 7.4 Fish-eye like failure from an internal pore, (a) σ_{max}=500 MPa, N_f=10,114,340 cycles, (b) facet and fine granular near the pore, ΔK=5.7 MPa$\sqrt{m}$, (c) and (d) rounded granular observed at ΔK = 13 MPa$\sqrt{m}$ and 23.7 MPa$\sqrt{m}$, respectively, at smooth area.

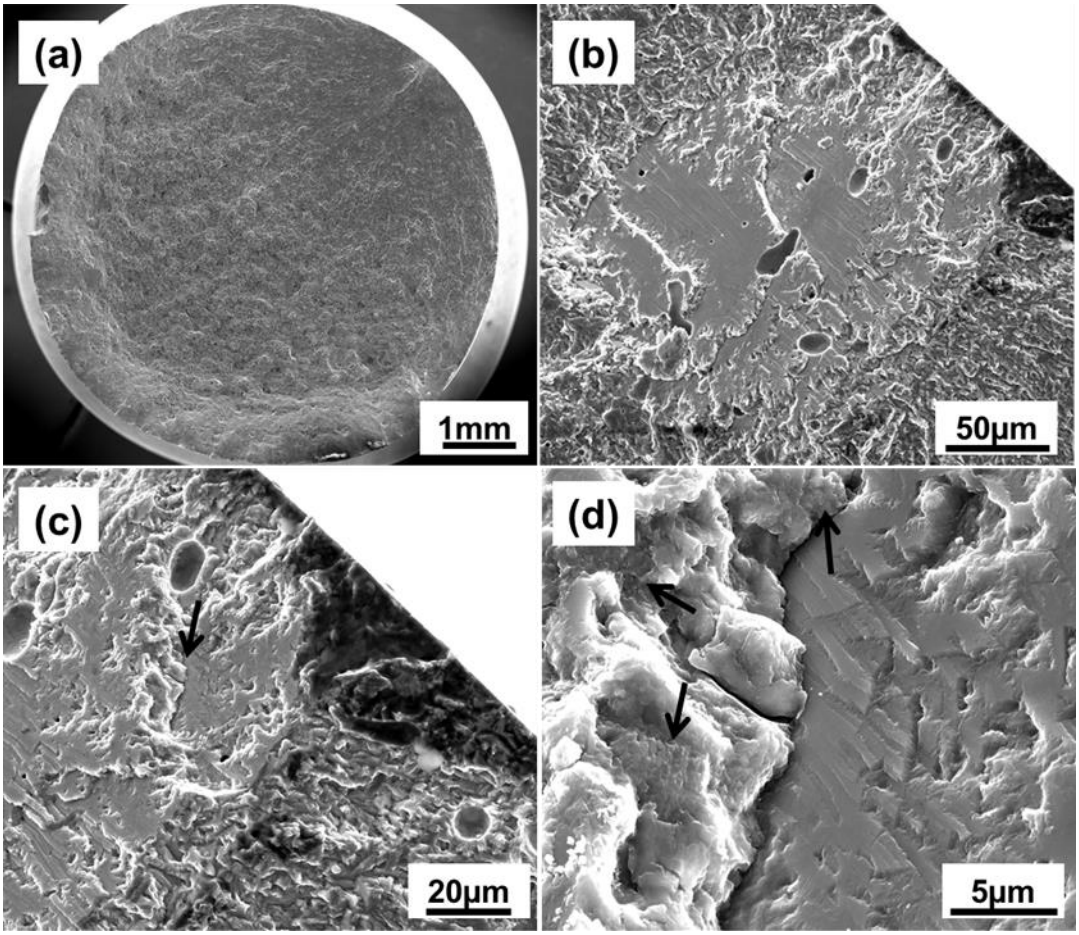

Figure 7.5 Facet formation near surface at low stress level, σ_{max}=520 MPa, N_f=3,272,656 cycles, (a) Overview of the fracture surface, (b) fatigue crack initiation site, (c) enlarged view of a step in the facet, (d) high magnification image of the arrow points area in (c).

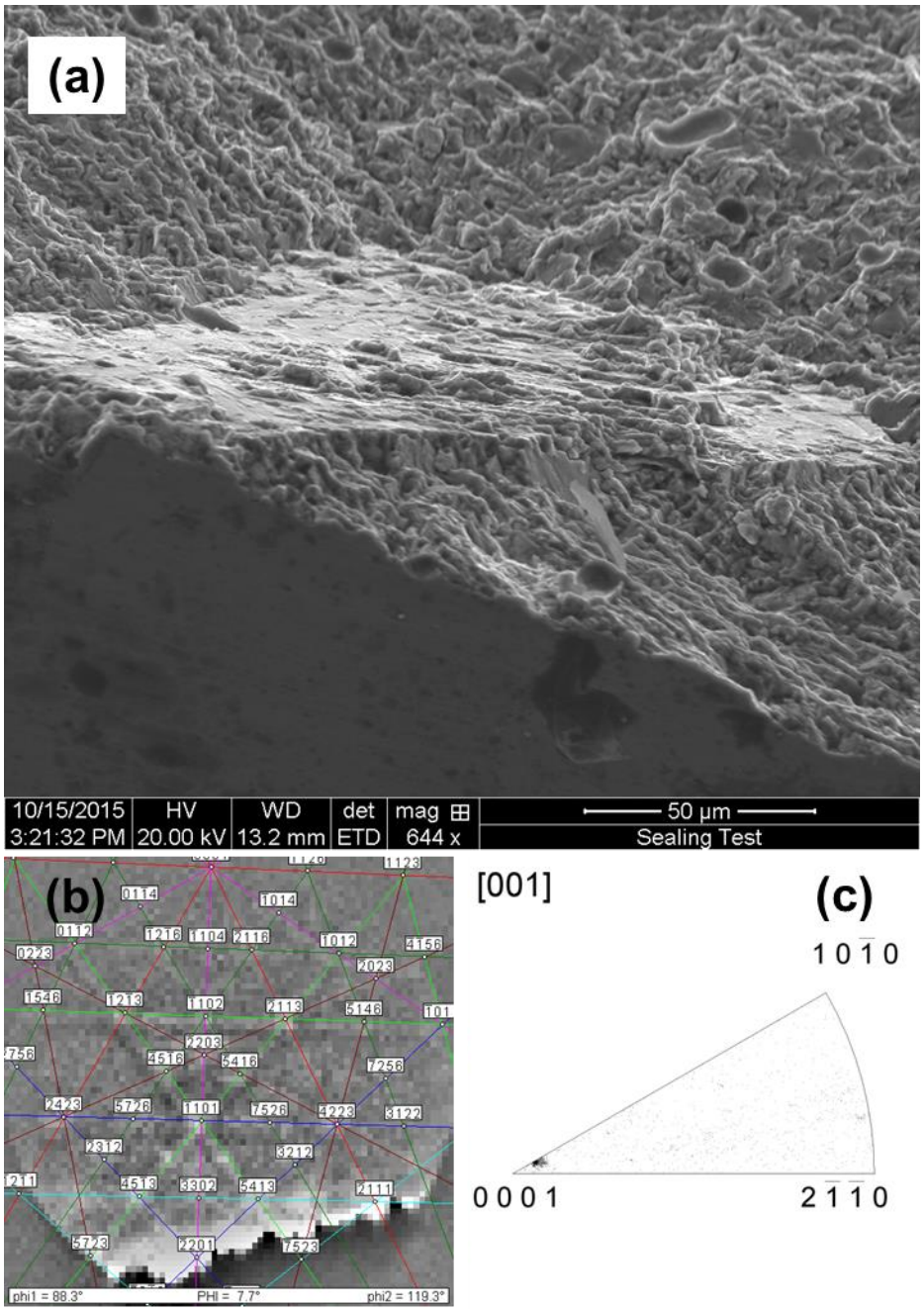

Figure 7.6 Determination of facet orientation using EBSD, (a) SEM image of a crack initiation facet (tilting corrected image) tilted to an angle of approximately 70˚ from horizontal, (b) index of a Kikuchi pattern with an index confidence of 0.59, (c) inverse polar figure shows orientation of the facet for 16 points analysis.

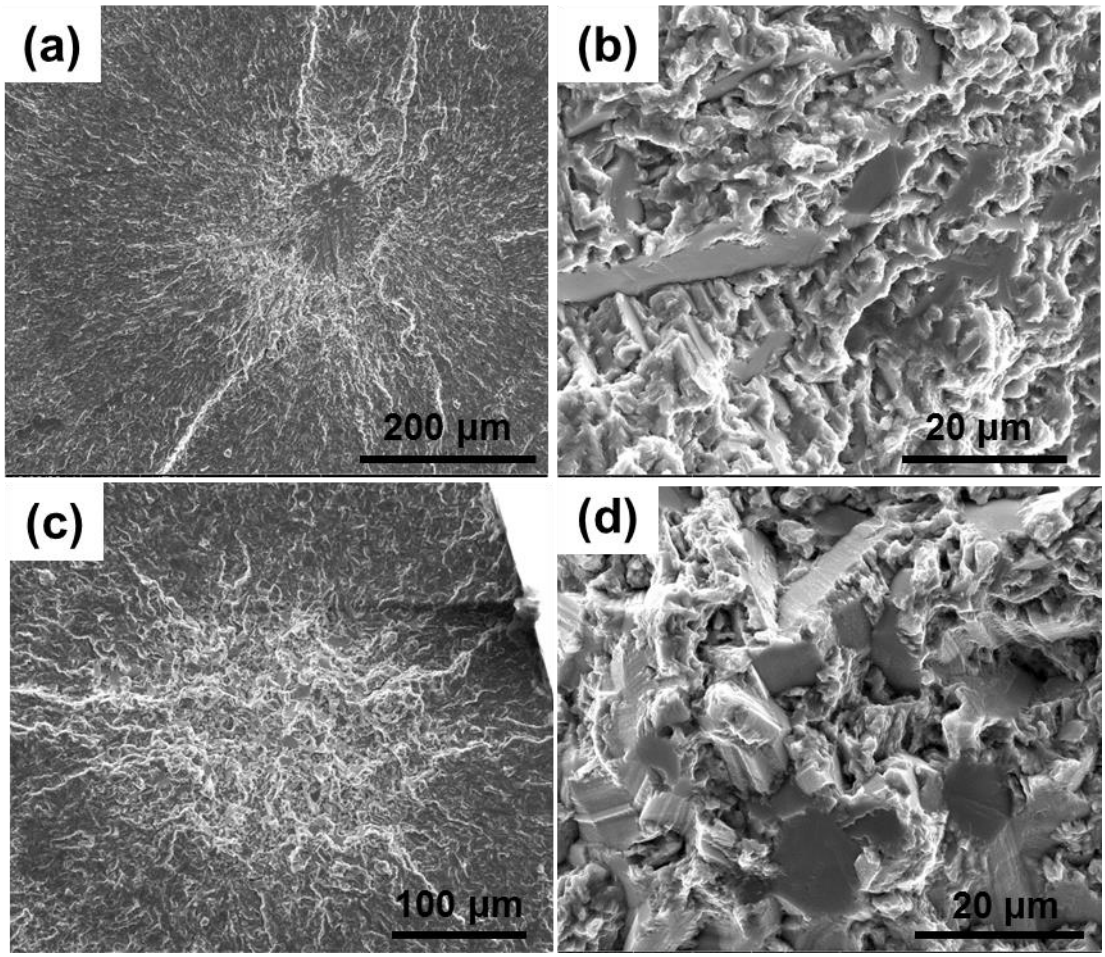

Figure 7.7 HCF failures from internal facet, (a) HSPT + PIF (σ_{max} = 750 MPa, N_f = 2,652,718 cycles), and (c) mill-annealed (σ_{max} = 720 MPa, N_f = 18,547,329 cycles) Ti-6Al-4V alloys, (b) and (d) are higher magnification images of the rough area in (a) and (c), respectively.

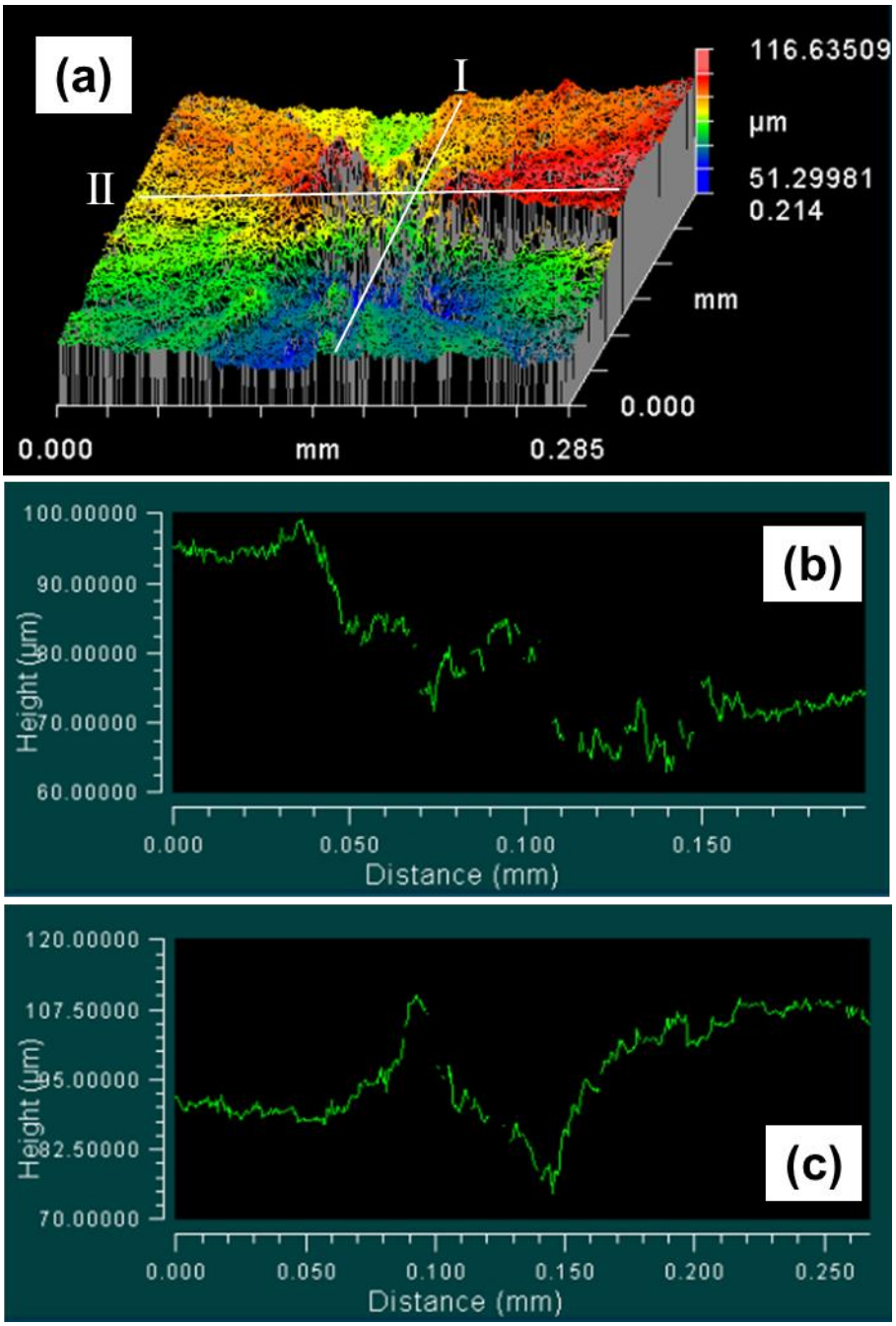

Figure 7.8 Fracture profile near crack initiation site, (a) topography of an internally failed sample (σ_{max} = 750 MPa, N_f = 2,652,718 cycles), profiles along line (I) and (II) are shown in (b) and (c), respectively.

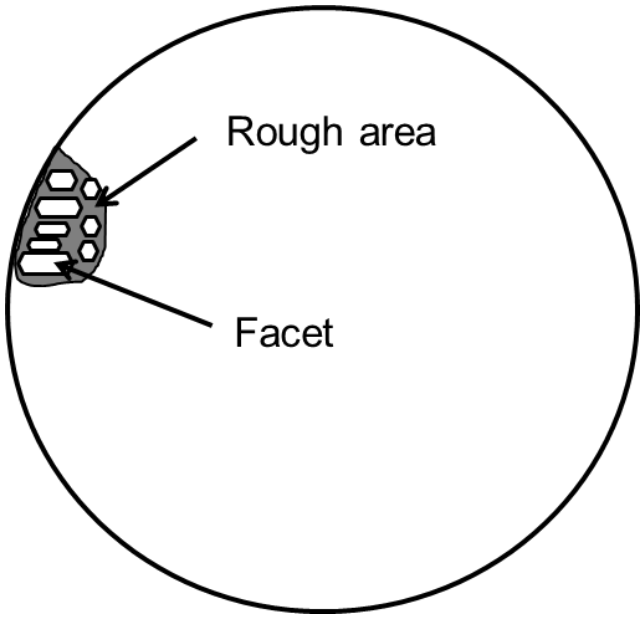

Figure 7.9 Schematic presentation of intermediate-to-high cycle fatigue failure.

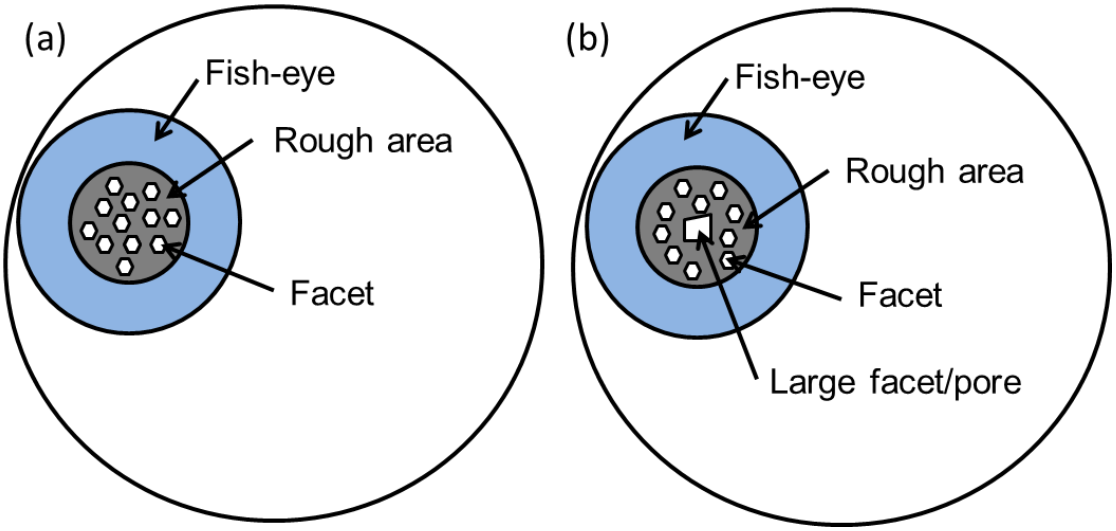

Figure 7.10 Schematic presentation of HCF failure, (a) mill-annealed Ti-6Al-4V with homogeneous microstructure, (b) HSPT Ti-6Al-4V alloy containing pores/large α grains.

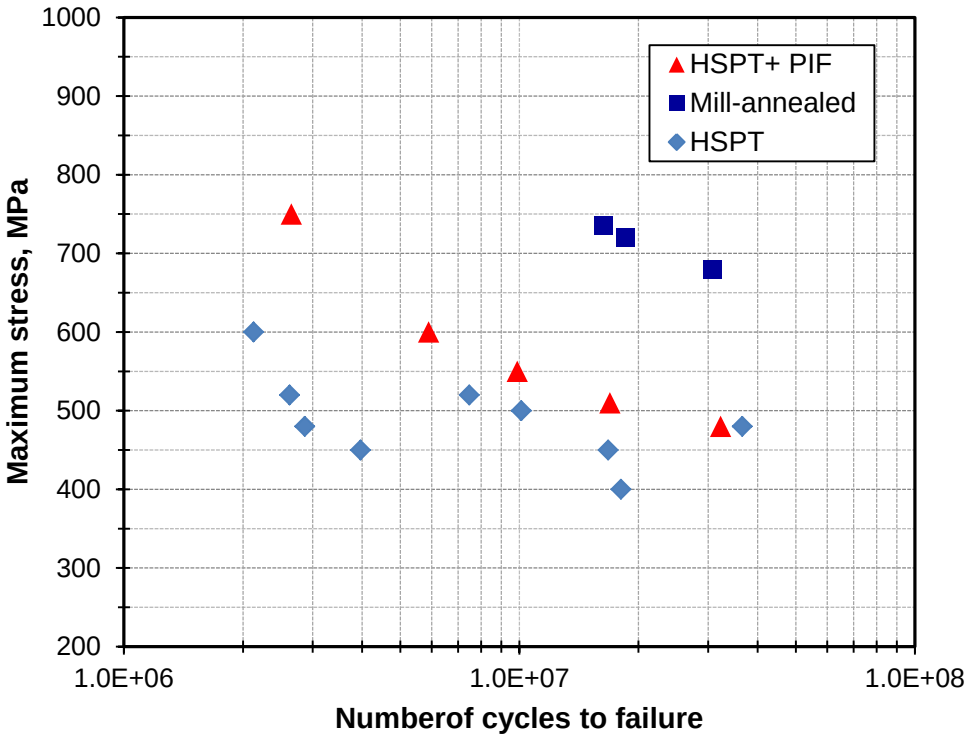

Figure 7.11 High cycle fatigue data of Ti-6Al-4V alloys with fish-eye like failure.

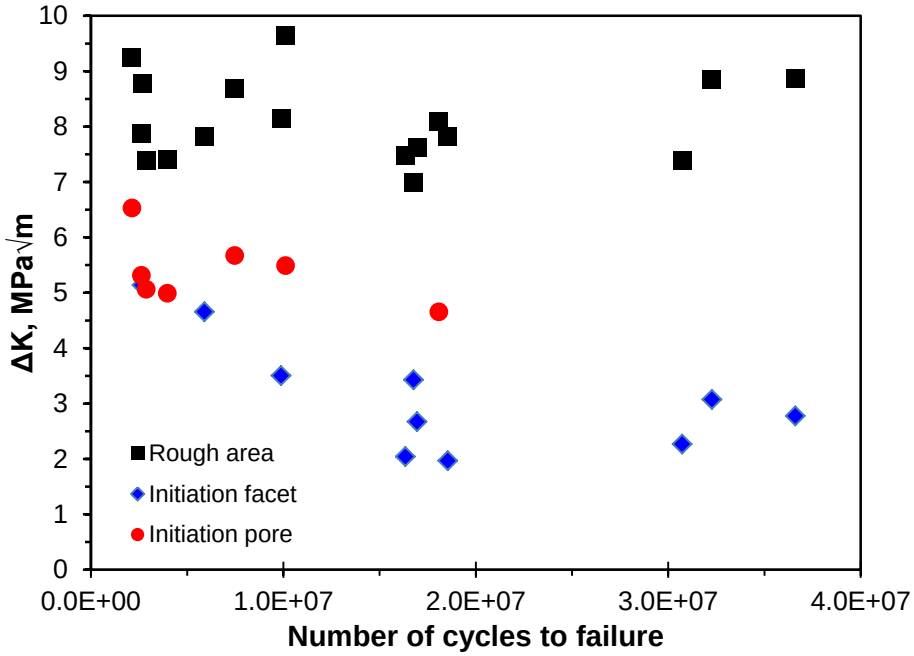

Figure 7.12 The correlation between ΔK on rough area and crack origin and HCF life.

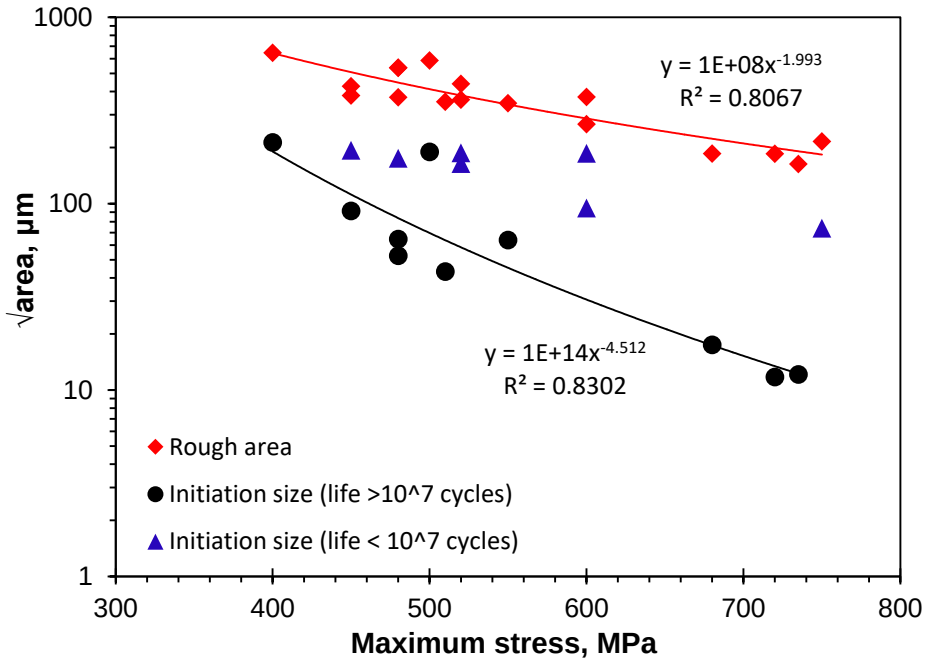

Figure 7.13 The correlation between fatigue crack initiation area and maximum stress.

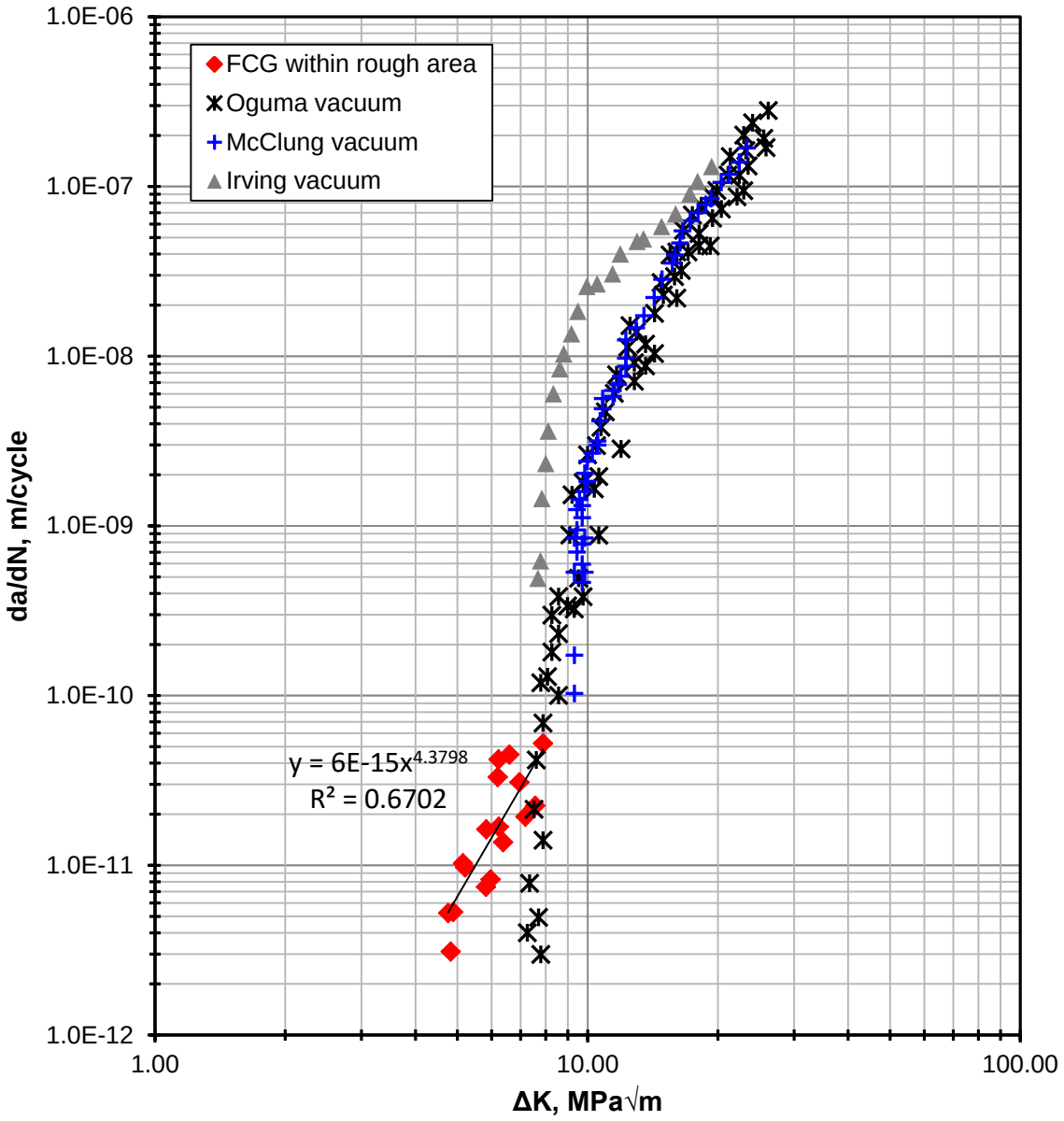

Figure 7.14 Estimated internal crack growth rate at near threshold region.

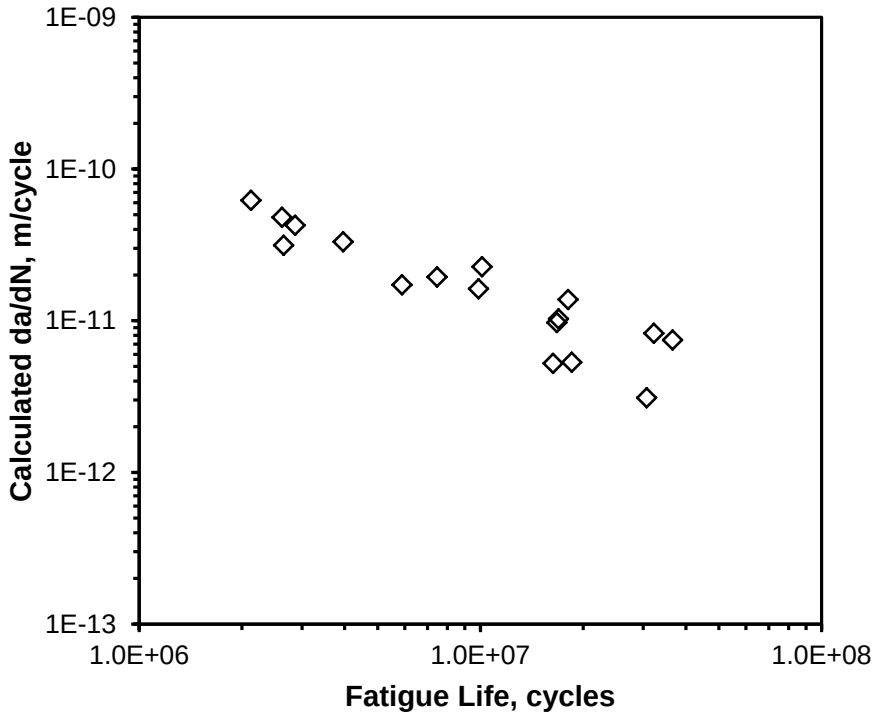

Figure 7.15 Calculated fatigue crack growth rate within rough area as a function of fatigue life.

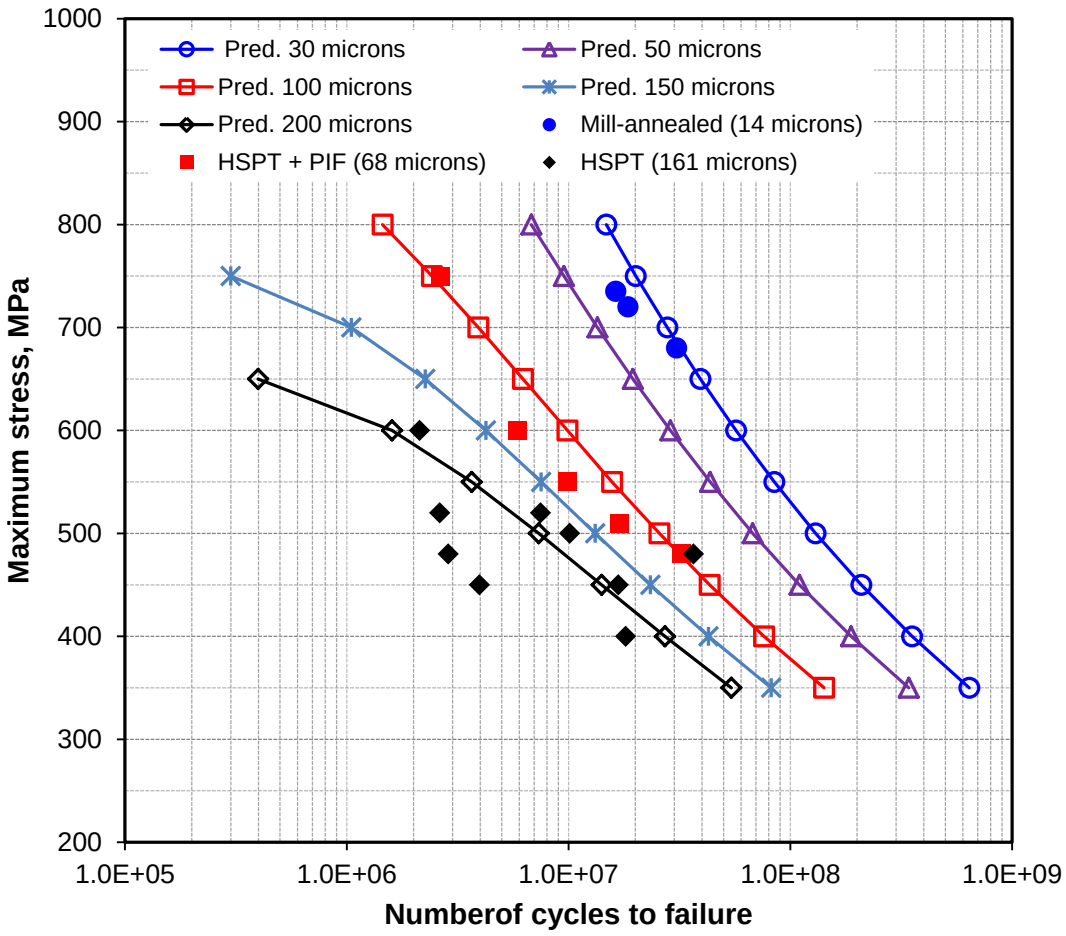

Figure 7.16 Predicted S-N curves at HCF region with different crack initiation sizes.

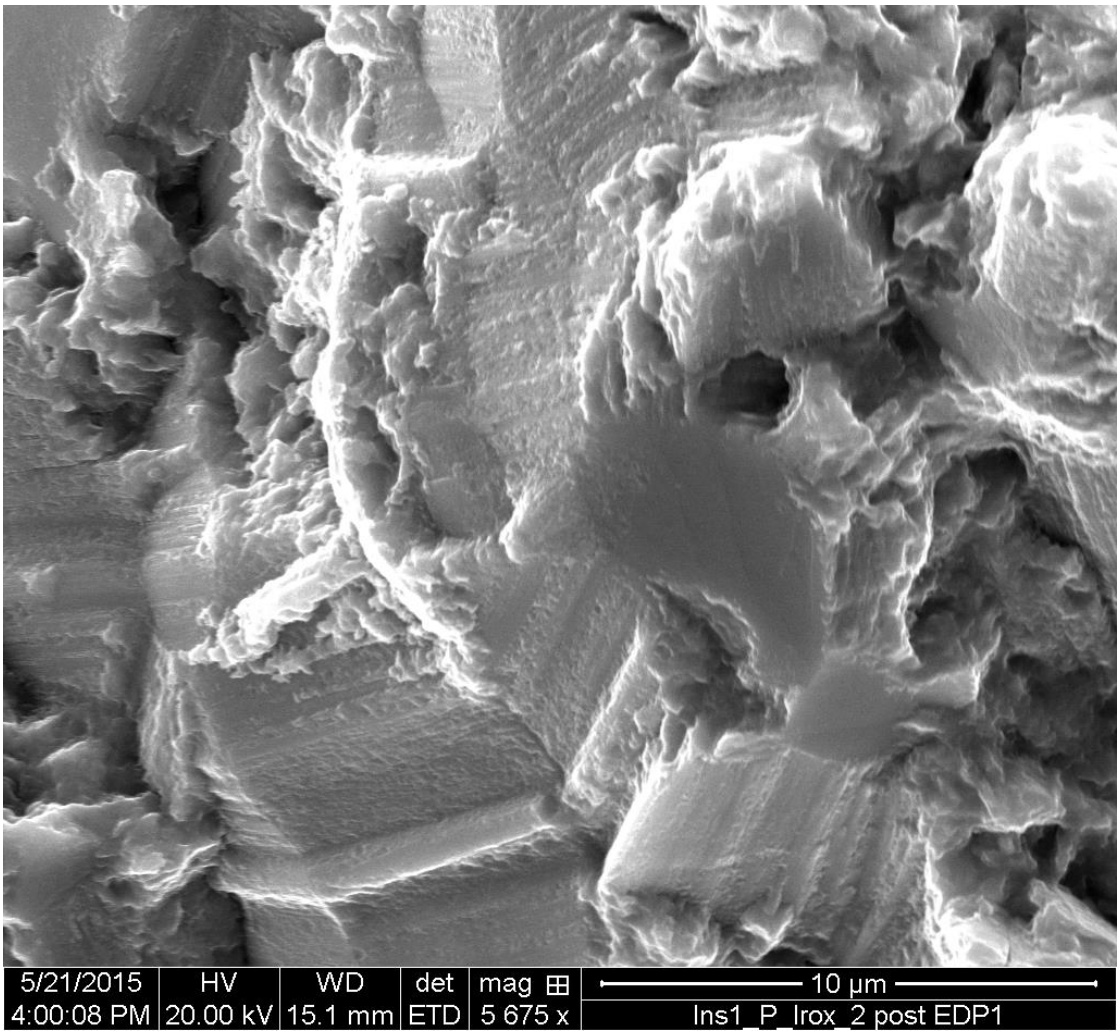

Figure 7.17 One set of facets in the crack initiation area (mill-annealed Ti-6Al-4V alloy).

7.4 References

1. Y. Murakami, T. Nomoto, T. Ueda, Fatigue Fract. Eng. Mater. Struct. 22 (1999) 581-590.

2. H. Oguma, T. Nakamura, Int. J. Fatigue 50 (2013) 89-93.

3. B. Künkler, O. Düber, P. Köster, U. Krupp, C.P. Fritzen, H.J. Christ, Eng. Fract. Mech. 75 (2008) 715-725.

4. C. Sun, J. Xie, A. Zhao, Z. Lei, Y. Hong, Fatigue Fract. Engng Mater. Struct. 35 (2012) 638-647.

5. A.J. McEvily, T. Nakamura, H. Oguma, K. Yamashita, H. Matsunaga, M. Endo, Scripta Mater. 59 (2008) 1207-1209.

6. F.O. Ruemelmoser, R. Pippan, H. P. Stuẅe, Acta Mater. 46(5) (1998) 1793-1799.

7. G. Chai, Mater. Sci. Forum 783-786 (2014) 2266-2271.

8. A. L. Pilchak, A. Bhattacharjee, A.H. Rosenberger, J. C. Williams, Int. J. Fatigue 31 (2009) 989-994.

9. B. Künkler, O. Düber, P. Köster, U. Krupp, C.P. Fritzen, H.J. Christ, Engng. Fract. Mech. 75 (2008) 715-725.

10. A.L. Wilkinson, S. G. Roberts, P.B. Hirsch, Acta Mater. 46 (1998) 379-390.

11. Y. M. Hu, W. Floer, U. Krupp, H. J. Christ, Mater. Sci. Eng. A 278 (2000) 170-180.

12. O. Umezawa, K. Nagai, ISIJ Int. 37 (1997) 1170-1179.

13. G. Chai, N. Zhou, S. Ciurea, M. Andersson, R.L. Peng, Scripta Mater. 66 (2012) 769-772.

14. X. Liu, C. Sun, Y. Hong, Mater. Sci. Eng. A 622 (2015) 228-235.

15. S. Jha, C.J. Szczepanski, R. John, J.M. Larsen, Acta Mater. 82 (2015) 378-395.

16. T. Sakai, Y. Sato, N. Oguma, Fatigue Frac. Engng Mater. Struct. 25 (2002) 765-773.

17. Y. Hong, Z. Lei, C. Sun. A. Zhao, Int. J. Fatigue 58 (2014) 144-151.

18. Y. Furuya and E. Takeuchi: Mater. Sci. Eng. A 598 (2014) 135-140.

19. D.F. Neal, P.A. Blenkinsop, Acta Metall. 24 (1976) 59-63.

20. A. Atrens, W. Hoffelner, T.W. Duerig, J.E. Allison, Scripta Metall. 17 (1983) 601-606.

21. A. Shanyavskiy, M. Banov. Eng. Fract. Mech. 77 (2010) 1896-1906.

22. K.J. Miller, Mater. Sci. Tech. 9 (1993) 453-462.

23. H. J. Christ, O. Duber, C. P. Fritzen, H. Knobbe, P. Koster, U. Krupp, B. Kunkler, Comput. Mater. Sci. 46 (2009) 561.

24. D. Eylon, J. Mater. Sci. 14 (1979) 1914.

25. Y. Murakami, Eng. Fract. Mech. 22 (1985) 101.

26. M.R. Bache, F.P.E. Dunne, C. Madrigal, J. Strain Analysis 45 (2010) 391-399.

27. R.K. Steele, A.J. MaEvily, Eng. Fract. Mech. 8 (1976) 31-37.

28. R.C. McClung, B.H. Lawless, M. Gorelik, C.Date, Y. Gill, and R.S. Piascik, Fatigue Crack Growth of Titanium Rotor Alloys in Vacuum and Air, 1999.

29. P.E. Irving, and C.J. Beevers, Metall. Trans. 5 (1974) 391-398.

CHAPTER 8

CONCLUSIONS

1. The hydrogen sintering and phase transformation (HSPT) process produces a high density Ti-6Al-4V alloy with fine α+β microstructure, which leads to a significantly improved tensile strength and fatigue performance, relative to the standard powder metallurgical approaches that use blended elements.
2. Fatigue strength in the as-sintered condition is greatly affected by the extreme-sized pores or clusters of pores present in the microstructure. The use of -400 mesh TiH_2 powder in sintering resulted in a significant improvement in fatigue performance, relative to -325 mesh powder, due to the increased sintering density and the elimination of pore clusters.
3. Pneumatic-isostatic-forging (PIF) after sintering closed the residual pores without coarsening the microstructure, which leads to a large increase in fatigue performance. The fatigue performance of HSPT + PIF processed materials is equivalent to the best fatigue results found in other PM Ti-6Al-4V alloys which were consolidated by HIP followed by additional heat treatment steps.
4. At high stress low cycle fatigue regime, residual pores on the specimen surface degrade the low cycle fatigue life significantly, though the pore is only around 20 μm. At low stress level high cycle fatigue regime, large α grains and pores in bulk

become effective crack initiators. The fatigue crack initiation mechanism in the HSPT-processed Ti-6Al-4V alloy is a competition between the extreme-sized pores and α phase regions.

5. Fatigue crack growth testing showed that the crack growth behaviors of HSPT and HSPT + PIF materials are similar, which indicates the micro-sized residual pores have no effect on crack growth behavior. The crack growth threshold of HSPT Ti-6Al-4V alloy is 3.2MPa√m.
6. Fractographic analysis of fatigue and fatigue crack growth specimens indicate that fine granules and facets near the high cycle fatigue crack initiation site are the symbols of a microstructural small crack growth region for high cycle fatigue failures. The value of ΔK_{RA} tends to be a constant; the value is between 7 and 9 MPa√m.
7. Most portions of fatigue life are consumed in the rough area (microstructural small crack growth region), and high cycle fatigue life is crack origin size-dependent. Large high cycle fatigue crack initiators lower the proportion of net rough area at given stress level, leading to shorter high cycle fatigue life.
8. The fracture pattern of rough area + fish-eye provides a way to estimate the crack growth rate in the rough area. The crack growth rate in the rough area is at the magnitude of 10^{-11} to 10^{-12} m/cycle, the rate decrease with the increase of fatigue life. The high cycle fatigue life estimated from the microstructural small crack growth rate and crack origin size matches very well with the current fatigue data.